5-2003

# Reactions of Alcohols and Organophosphonates on Tungsten Trioxide Epitaxial Films

Shuguo Ma

# REACTIONS OF ALCOHOLS AND ORGANOPHOSPHONATES ON TUNGSTEN TRIOXIDE EPITAXIAL FILMS

By

Shuguo Ma

B.S. Inner Mongolia Normal University, 1991

M.S. Institute of Chemistry of Chinese Academy of Sciences, 1995

A THESIS

Submitted in Partial Fulfillment of the

Requirements for the Degree of

Doctor of Philosophy

(in Chemistry)

The Graduate School

The University of Maine

May, 2003

Advisory Committee:

Brian G. Frederick, Associate Professor of Chemistry, Advisor

François G. Amar, Associate Professor of Chemistry

Alice E. Bruce, Associate Professor of Chemistry

Robert J. Lad, Professor of Physics

Carl P. Tripp, Professor of Chemistry

# REACTIONS OF ALCOHOLS AND ORGANOPHOSPHONATES ON TUNGSTEN TRIOXIDE EPITAXIAL FILMS

By Shuguo Ma

Thesis Advisor: Dr. Brian G. Frederick

An Abstract of the Thesis Presented
in Partial Fulfillment of the Requirements for the
Degree of Doctor of Philosophy
(in Chemistry)
May, 2003

The adsorption, diffusion, reactions, and desorption of water, alcohols, ethers, and an organophosphonate were studied using calibrated thermal desorption spectroscopy (CTDS) on thin film $WO_3(001)$ surfaces grown epitaxially on a single crystal $\alpha$-$Al_2O_3(1\bar{1}02)$ (sapphire) substrate. The studies were conducted on oxidized and reduced surfaces, which were characterized by x-ray photoelectron spectroscopy (XPS) and ultra-violet photoelectron spectroscopy (UPS). The desorption spectra for molecular desorption of all of these molecules shifted to lower temperature with increasing coverage, and had overlapping tails on the high temperature side. Monte Carlo simulations show that this typical desorption shape can be characterized by first-order or pseudo-first-order desorption kinetics in which rapid diffusion allows the molecules to find and desorb from the most strongly bound sites of a heterogeneous surface.

For methanol, UPS revealed molecular adsorption on the oxidized surface and dissociative adsorption on the reduced surface, but only molecular desorption of methanol was detected. For ethanol and isopropanol, competition between molecular

desorption and dehydroxylation at lower temperature controls the alkoxy coverage remaining and consequently, the selectivity toward alkenes. The selectivity was coverage dependent, but was not significantly different on the oxidized and reduced $WO_3(001)$ surfaces. The rate limiting step in the dehydration of the alkoxy species to ethylene or propylene was identified as C-O bond scission. Dimethoxymethane showed some decomposition to methanol on both surfaces, while only molecular desorption was found for dimethyl ether. Dimethyl methyl phosphonate (DMMP) decomposed on both the reduced and oxidized surfaces through loss of methoxy groups. Methanol and dimethyl ether were detected on the oxidized surface, while only dimethyl ether was observed on the reduced surface. Comparison of the dimethyl ether production with spectra following adsorption of dimethyl ether suggests that the rate limiting step is a surface catalyzed, intramolecular coupling reaction between methoxy groups. The C1s and P2p XPS features were consistent with a methyl phosphate-like species remaining after DMMP decomposition.

## ACKNOWLEDGMENTS

During my study in the University of Maine, my advisor spent a lot of time advising me. At the time I finished my thesis, I first thank my advisor for his help to me and to my family, and his encouragement to me. I thank Dr. Robert Jackson for offering important help to me in the period in which I learned to use CTDS system and very helpful discussions on my experiments. I thank George Bernhardt for growing the $WO_3$ films on the sapphire substrates and my committee members for their comments on my thesis. Thanks also go to Nancy R. Curtis, Science of Engineering Librarian, who gave me very nice help during literature search. This research work was sponsored by the Dept. of Navy, Naval Surface Warfare Center, Dahlgren Laboratory, Grant No. N00178-99-1-9002 and the Office of Naval Research Grant No. N00014-01-1-0921. Finally, I thank my wife, Yujing Wen, for her support.

I always feel the encouragement from my parents. This thesis is dedicated to my parents.

## TABLE OF CONTENTS

## LIST OF TABLES

## LIST OF FIGURES

# INTRODUCTION

## 1.1. Semiconducting metal oxide (SMO) chemiresistive sensors

### 1.1.1. Gas sensor application and development

Metal oxides have important applications in many fields from dielectrics to catalysts.[1-5] One specific area of interest is their potential use in sensor technology as highly sensitive materials for detection of flammable or toxic gases. In the 1960's, a $SnO_2$ based sensor was developed and commercialized by Taguchi.[6,7] These thick film devices appeared in households in Japan to monitor explosive methane gas, opening an important application for semiconducting metal oxides in sensor technology. Since then a number of research groups recognized the electrical conductivity of $ZnO_2$ changes with the surrounding gas composition.[8,9] Over the past 30 years, $SnO_2$ and $ZnO_2$ have been extensively studied as sensing materials[10-14].

The early $SnO_2$ gas sensor, even though meeting the needs at the time, was known to be sensitive to humidity and to have poor selectivity.[15] After more than four decades of study, even though sensor designs have been improved significantly, selectivity remains a challenging question. In fact, most SMO sensor technology that is commercially available is developed for use in a specific application, such as detection of combustion gases, differentiating coffee from different geographic regions, and the oxygen sensor in vehicles.

The alternative to chemical sensor technology is, of course, analytical instrumentation. Techniques such as gas chromatography/mass spectrometry (GC/MS), optical absorption and fluorescence spectroscopy have the advantages of being able to analyze a wide range of chemical compounds with equally high sensitivity and much

better selectivity. However, these instruments require trained personnel, are very expensive, and are generally large in size. In comparison, metal oxide based sensors offer the advantages of much lower cost and very small size, that would allow widespread use for continuous monitoring of chemical threats in the environment from industrial sources or terrorism.[16]

For semiconducting metal oxide sensors to be successfully commercialized, several parameters are vital: sensitivity, response time, selectivity (sometimes called specificity) and reproducibility of the sensor. Although the work in this thesis focuses on surface reactivity, we recognize that many factors may play an important role in determining a sensor response. In addition to the intrinsic electronic properties of metal oxides, morphological factors, such as the size of grains in the sensing film or powder, grain boundaries and other defect structures, the thickness of the film, and dopants can be important. [9,14,17] Studies have shown that the magnitude of an oxide thin film response can be improved by using films composed of nanosized particles or doping with transition metal elements.[9,18-21] For instance, it has been shown experimentally that the $WO_3$ based SMO sensor does not respond to NO; however, Ag or Au doped $WO_3$ films do respond significantly.[22] In practice, the oxide sensing material may be fabricated using thin or thick film techniques [13,19,23-27], having the advantages of easy fabrication and low cost of materials. Advances in fabrication of high quality thin film materials may provide opportunities to tailor the surfaces for a specific surface reaction by controlling its physical or electronic surface structure.

### 1.1.2. Sensing mechanism

Chemiresistive sensors are based upon one of several transduction mechanisms. For semiconducting metal oxides to be used as sensing materials the conductivity (resistance) must change upon exposure to target gases. These sensors are usually operated at elevated temperatures. Within the area of SMO sensors, we can distinguish two different mechanisms that are important, depending on the material. One is a space charge or band bending model; the other involves changes in the bulk conductivity and rapid vacancy diffusion.

The space-charge layer model was proposed for understanding the sensing mechanism on $SnO_2$ and $TiO_2$ based sensor materials.[10] When an adsorbate can act as an electron trap, most importantly $O^-$ and $O_2^-$, an electron depletion layer will be formed at the semiconducting oxide surface.[11] When the carrier density is low, the depletion layer can extend deep into the bulk. This results in a decrease of the surface conductivity due to the reduction of the electron density in the surface layer. The depletion layer is characterized by upward surface band bending.[10] The effect is most dramatic when the bulk conductivity is small compared to that of the surface. Upon exposure to a hydrocarbon target gas, the compound can be oxidized by surface active oxygen ion species ($O^-$ or $O_2^-$)[2] which then releases the trapped electrons back into the surface region and the surface conductivity increases.

The presence of surface oxygen species has been identified by electron spin resonance (ESR) experiments on a number of solid surfaces including $TiO_2$.[2,28,29] Due to the high activity of surface oxygen species that are stable on these materials, hydrocarbons usually undergo complete combustion into $H_2O$ and $CO_2$. Hence, this class

of oxide catalysts acts as complete combustion catalysts. Conversely, an accumulation layer, characterized by downward surface band bending, can be formed if the molecules adsorbed on a surface donate electrons to the conduction band, resulting in an increase in the conductivity.

On oxide surfaces, such as $V_2O_5$, $MoO_3$, and $WO_3$, in which the highly reactive $O^-$ and $O_2^-$ species are not stable, and the metal oxygen bond strength is not too high, a different mechanism becomes important. The adsorbed hydrocarbon molecules react, on n-type materials, with the lattice oxygen ($O^{2-}$) to leave oxygen vacancies and excess electrons behind. The resulting electrons can be thermally excited into the conduction band to give rise to an increase in conductivity. The higher energy barrier involved in the abstraction of lattice oxygen usually results in the hydrocarbons being partially oxidized. For example, methanol is converted selectively to formaldehyde on $MoO_3$ and $WO_3$. Hence, materials such as $V_2O_5$, $WO_3$ and $MoO_3$ are known as selective oxidation catalysts.

The transduction mechanism is considerably different in these materials as well. Isotope labeling studies [30] established that the oxygen vacancy diffusion rate in $WO_3$, $MoO_3$, and the related perovskite materials is very large compared to materials such as $SnO_2$ and $TiO_2$. Therefore, the oxygen vacancies diffuse through the depth of the film [31] and the electron density of the entire film depth must change. Recent work by Ren[32] suggests that the conductivity is controlled by either Schottky barriers at the electrode-oxide interface, or barriers at the grain boundaries. Unusual resistance- voltage curves suggest that the tunneling rate is strongly modulated by the carrier concentration, which controls the width of the barrier. Thus, the relationship between the rate at which oxygen

vacancies are removed from the lattice and the rate the conductivity changes probably depends on morphological factors such as grain size; however, the relationship may be approximately linear, as long as the diffusion processes are not rate limiting.

### 1.1.3. The role of surface science in sensor technology

From a device point of view, we can separate the electrical response of the sensor from the surface chemistry. The electrical response could, ideally, be described by a function that converts the rate of oxygen removal (and electron injection) at the surface into a time-dependent conductivity change. It would include the geometrical parameters of electrode spacing and film dimensions, morphological parameters such as grain size and orientation, solid state kinetics, such as shear plane formation and vacancy diffusion, and fundamental solid state material properties, including electron mobility, dependence of the Thomas-Fermi length on substoichiometry of the oxides, and the temperature dependence of electron transport mechanics in the bulk and at grain boundary or Schottky barriers. The response function, from a linear system point of view, might be expressed as a complex function that describes the amplitude as well as phase lag in the response to an impulse or step function input.

The surface chemistry, in our view, provides the input to the system response function. The rate of the chemical reactions and the stoichiometry determine the rate of oxidation or reduction of the surface. In principle, if the absolute rates of the reactions can be specified, then the ultimate sensitivity and response time can be determined and, ideally, optimized. However, the most important issue in sensor development is selectivity. The extent to which one compound can be distinguished from another on the

same sensor is ultimately dependent on the variation in the surface kinetics behavior that can be used to identify the compound or class of compounds. A fundamental understanding of the surface processes can contribute to understanding the limitations as well as suggesting alternative strategies [33] to improving sensor selectivity.

The surface kinetics include a number of steps, including adsorption (including physical and chemical adsorption), diffusion (including adsorbate surface diffusion and bulk defect diffusion), surface reaction and desorption processes. Each of these factors is temperature dependent and may vary with the crystal face and surface structure. The rate-limiting step, whether an acid-base reaction, an adsorption or diffusion process, determines how fast a sensor responds to a gas. The stoichiometry of the reaction and the redox properties determine the response magnitude, because it determines the number of electrons transferred between the reactant and the surface, which directly influences the conductivity change. Therefore, understanding of all of these processes is fundamental and crucial for the research in sensor technology.

A surface reaction is also closely related to the geometric and electronic surface structure. The role of surface defects in surface physicochemical processes, such as the adsorption, desorption, nucleation of adatoms and surface reactions, is very well known.[34-36] On the oxide surfaces, especially transition metal oxides, a large variety of defects can exist, which may exhibit different catalytic reactivities for surface reactions.

Surface science research can contribute to a fundamental knowledge of these processes. However, although there is extensive interest in understanding oxide surface chemistry and catalysis, the greater complexity of oxides, compared to metals, means that our understanding of oxide chemistry is limited. So far, studies focusing on the effect of

surface electronic structure on surface chemistry on oxide surfaces are limited to a few oxides, of which $TiO_2$ is probably the most extensively studied.

### 1.2. Research on metal oxide surfaces

Traditionally, most studies on oxides have focused on exploring their role in catalysis, as a catalyst support or modifier. For instance, deposition of metals on oxide surfaces, treated as a catalyst model system, have been used to investigate the electronic and chemisorption properties of these systems.[34,36-39] More recently, interest in oxide surfaces has expanded, with notable work driven by environmental applications. Sensor research, in some sense, encompasses both of these areas.

Relative to metals and semiconductors, the progress in understanding the surface of metal oxides lags behind, although it is currently a very active area of research. This can be attributed to the additional complexities in the surface composition and electronic structure incurred by oxide surfaces.[40,41] as well as the difficulties in working with insulators. From the surface structure point of view, maintaining the stoichiometry at the surface can be difficult. Defects, such as oxygen vacancy point defects, can easily be introduced during surface preparation. The surface oxygen composition is related to the oxygen partial pressure, which is very low in a UHV environment (typically $< 10^{-10}$ torr). Thermodynamically, the surface should be reduced, resulting in a substoichiometric oxide surface. The extent of surface reduction is determined, in practice, by reaction kinetics as well as the energetics for formation of the metal oxide. Transition metals usually have several stable oxidation states available, depending on their d electron configuration that allows the possibility of different oxidation states, which may result in

surfaces exhibiting very complicated surface structures. For instance, LEED, XPS and Auger spectroscopy have shown that single crystal (110) and (100) $RuO_2$ surfaces are highly non-stoichoimetric due to the presence of $RuO_3$.[42,43] A detail review of metal oxide structures is given by Henrich and Cox.[41]

Cleavage is probably the best method to prepare a surface having a bulk-terminated structure. However, not all metal oxides can be cleaved and even for those for which the cleaving method is applicable, the planes which can be successfully cleaved are limited as well. Due to the ionic nature of the bonding between oxygen and metal atoms, polar surfaces will relax and may reconstruct but others will facet. Tasker's rules[44] provide some basis to determine when a polar surface is not stable. The reality, as shown in STM or AFM studies, is that surfaces, even those giving rise to sharp LEED patterns, vary widely from highly perfect [45,46] to rough and defective.[47] An alternative method to cleaving is to cut a sample along a certain plane followed by mechanical polishing and etching. In-vacuum sputtering and annealing in oxygen at a high temperature are then performed to remove surface contaminants and restore the surface structure, respectively. The latter method has been successful on $WO_3(001)$ [48] and other oxide surfaces. Nevertheless, irreversible damage occurs during sputtering.

The electronic structure of transition metal oxides with $d^n$ ($n>0$) electronic configurations is also very complicated. The band theory model, which is very successful in interpreting the electronic structure of metals and semiconductors such as silicon and III-V compounds, may not be able to accurately describe the electron transport properties of $d^n$ transition metal oxides. The oxygen coordination around the d orbitals causes splitting, known as crystal field or ligand field splitting. It is well known

that d orbitals contract, depending on the atomic number and ionic charge. Therefore, the overlap between d electron orbitals is very small so that the band width is narrow. In band theory, this narrow d-band is the conduction band, but it may not be very "conductive" due to the localized nature of these d electrons. The Hubbard model[40,41] has been proposed to interpret d electron transport. A moving charge carrier will polarize the ions around it due to the electrostatic interaction. The lattice distortion will respond very slowly and produce a drag on the carrier motion. The polarization of the lattice structure in the presence of a carrier is called a small or large polaron [49], with the size depending on the electrostatic interaction. The polarization energy can be comparable to the bandwidth of the d electrons for transition metal oxides; therefore, a defect state, whether a hole or an excess electron, may be localized. The motion of the polaron will be affected by the thermal energy in the oxide lattice. Although conductivity increases with temperature like typical semiconductors, it has a different functional behavior. As we shall see, the theoretical understanding of the electron transport properties also impacts the characterization of the surface structure, since in XPS final state relaxation effects in narrow d-band oxides are thought to result in unusual behavior.[40,41,50-52]

### 1.3. $WO_3$ structure and applications

The crystal structures of $WO_3$ are based on corner sharing octahedra corresponding to distortion of the cubic $ReO_3$ type structure. The deviation of the unit cell from the cubic structure in the various phases [53] involves tilting of the octahedra which is attributed to the partly covalent nature of the bond between tungsten and oxygen.[54] The network formed by corner sharing octahedra makes the $WO_3$ structure

very open, having an interstitial site with 12-fold coordination that can accommodate foreign cations to form tungsten bronzes. For example, Na and H doped $WO_3$ are known as the sodium and hydrogen bronzes, respectively.[55,56] Doping makes $M_xWO_3$ semiconductive at low cation composition, x, and metallic at higher composition.[57,58] We should note that there is interest in the development of $WO_3$-based materials for electrochromic displays exists.[59-61] The characteristics of the open structure may be responsible for the difference in oxygen exchange reactions [30] between $WO_3$ and other metal oxides, such as $TiO_2$ and $Al_2O_3$.

The ability of selective oxidation catalysts to lose oxygen and become substoichiometric is also thought to be related to the defect structures that they can form. The bulk or surface defects are thought to be oxygen vacancies, which can be produced during treatment of the surface. Crystallographic shear (CS) planes have been identified in the bulk of $TiO_2$, $MoO_3$ and $WO_3$ oxides.[62-65] When the density of oxygen vacancy point defects in a region is high enough, an edge sharing structure forms to remove oxygen vacancies. The driving force for formation of CS planes may be the spatially delocalized $d^1$ electron interaction. When the CS planes intersect the surface, they should form line defects. Such structures have not been firmly established, but they may be related to regions with high electron density on the reduced $WO_3(001)$ single crystal surface that have been identified in STM,[50] referred to as "raft" or "trough" structures. Potential use of $WO_3$ as a sensor material has been investigated in previous studies. Studies have shown that $WO_3$ responds to $NO_2$ and $H_2S$[15,18,23-27].

## 1.4. Motivation and organization of this thesis

Research and development work at the Laboratory for Surface Science and Technology (LASST) for a number of years has focussed on growing high quality $WO_3$ thin films [53,66-68] for use in detection of $H_2S$ [69], NO [70], and more recently detection of chemical warfare agents[71]. Due to the deadly toxicity of the nerve agents (e.g. sarin and tabun), organophosphonates such as dimethyl methylphosphonate (DMMP) are used as simulants in sensor development. Studies show that $WO_3$ thin film sensors respond to DMMP; however, they also respond to methanol.[71] The structure of the chemical warfare agents and DMMP are shown in Figure 1.1. Because the sensor response (in all SMO sensors) involves combustion of the hydrocarbon side chain, the response to DMMP may differ from the chemical warfare agents that have ethoxy and isopropoxy groups instead of methoxy groups. This also suggests that the alcohols may be strong interferents and several projects [33,71] are currently aimed at distinguishing alcohols from organophosphonates. In order to improve selectivity, understanding of the surface chemistries of methanol, ethanol, isopropanol and DMMP is very important.

DMMP has been extensively studied on different metal oxide surfaces.[72-80] Inelastic electron tunneling spectroscopy[80] and infrared[74,76] studies showed that DMMP decomposes on $TiO_2$, MgO, and aluminum oxide surfaces by losing the first methoxy group at low temperature and the second at high temperature. An adsorbed methoxy group has been identified on the surface of some oxides.[76] An infrared study by Kim, *et al.*[81] of DMMP interaction with $WO_3$ powder showed a similar decomposition mechanism, leaving a methyl phosphate intermediate that is stable to high temperatures.

However, most of these studies have focussed on the decomposition intermediate and not on the fate of those intermediates or which step is rate controlling.

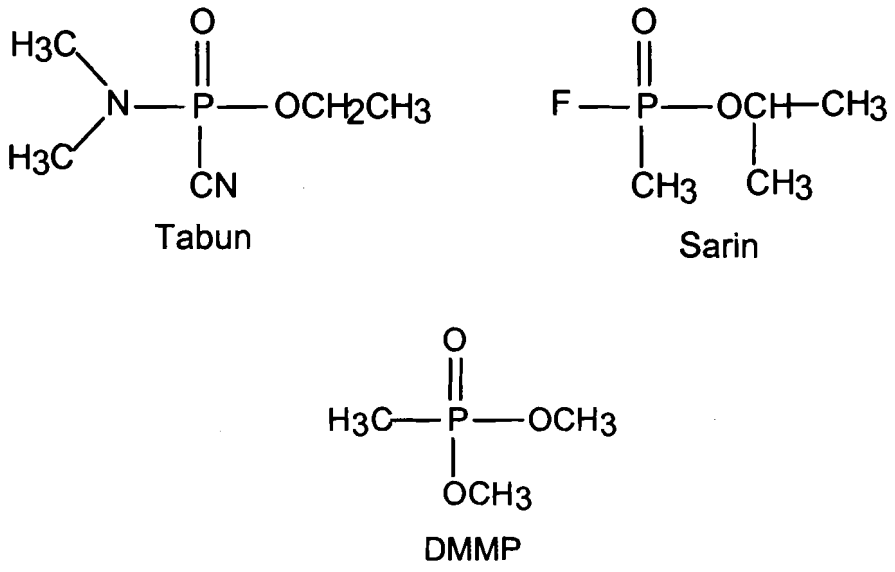


**Figure 1.1.** The structures of tabun, sarin, and DMMP

As discussed in section 1.1.2, hydrocarbons can be oxidized in two different pathways depending on the type of metal oxide catalyst: formation of $CO_2$ and $H_2O$ in the presence of surface active oxygen species on catalysts such as $TiO_2$, or selective oxidation products, such as conversion of methanol to formaldehyde or formic acid, involving lattice oxygen. As mentioned in section 1.1.2, the sensor response depends on the kinetics of the rate limiting step of the reaction as well as stoichiometry of the redox reaction. The rate limiting step in the mechanism of oxidation of methanol to formaldehyde on bismuth doped molybdenum oxides is thought to be α-H abstraction. The product distribution is similar on $WO_3$ [82] but the surface activity of $WO_3$ is not

necessarily the same, due to the differences in the materials. The reactivity of primary, secondary, and tertiary alcohols has been discussed by Tanner [47] on $WO_3(001)$ and Kim [83,84] for $TiO_2$, which suggests that differences in the rate limiting step may be important for distinguishing alcohols and organophosphates in sensing applications. Our goal is to relate the mechanism of the surface reaction to the surface geometric and electronic structure of the $WO_3$ films used in sensors. This motivated the research in this thesis.

In this research work, alcohol molecules, including methanol, ethanol and isopropanol, and reaction products of the alcohols and DMMP, including dimethyl ether (DME) and dimethoxymethane (DMM), were chosen in order to study the catalytic properties of the $WO_3$ thin film surfaces. Alcohol molecules, widely used as probe molecules in catalysis and surface science, were used to probe the fundamental surface properties, such as chemisorption, diffusion, and reactivity toward dehydration and dehydrogenation. Formation of DME and DMM have been reported in previous studies as reaction pathways for methanol or methoxy on metal oxide surfaces.[35,85-87] The studies of the interactions of these molecules with $WO_3$ surfaces are then used to gain an understanding of the surface chemistry and decomposition of DMMP.

## EXPERIMENTAL

### 2.1. System configuration and characteristics

All of the spectroscopic experiments were performed in a stainless steel vacuum chamber, which was pumped by a turbo-molecular pump and an ion pump to a base pressure of $5\times10^{-10}$ mbar. The system is equipped with a differentially pumped mass spectrometer, sputtering gun, concentric hemispherical electron energy analyzer, dual-anode x-ray source, and differentially pumped UV lamp, as shown in Figure 2.1.

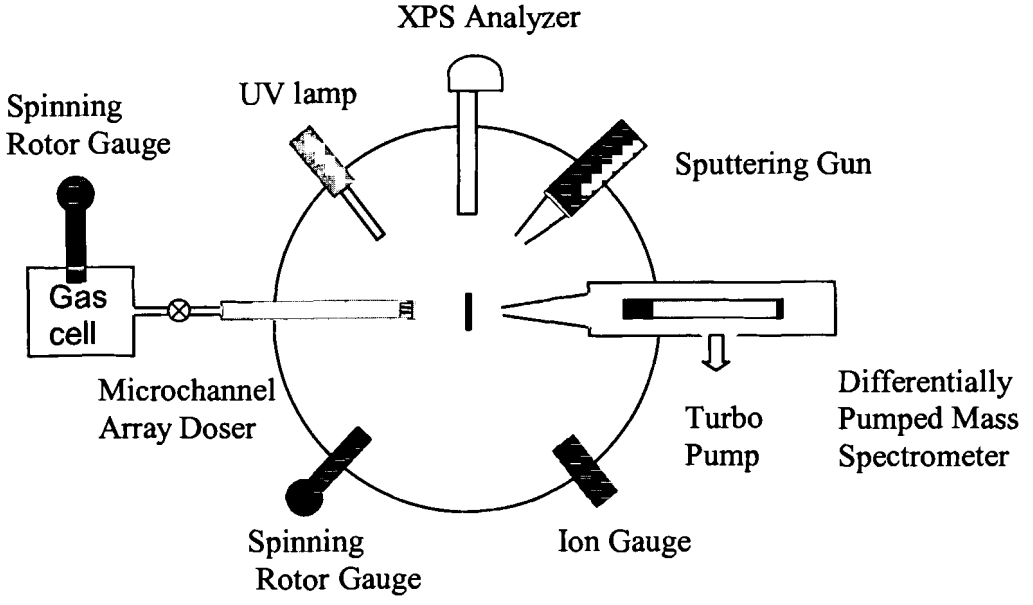


**Figure 2.1** Schematic display of the CTDS system

The mass spectrometer (Balzers QMG 112 A) is mounted in a cylindrical shroud, which is coaxial to the ionizer and quadrupole. The shroud extends to a translatable conical shroud in front of the ionizer with a 3.63 mm diameter aperture at the end. A second turbo molecular pump (360 liters/s) was used to separately pump the mass

spectrometer housing. The shroud geometry was designed [88] so that the following properties were achieved: (1) a linear relationship between the pressure in the ionizer and the mass spectrometer signal over four orders of magnitude; (2) sensitivity to $10^{10}$ molecules/($cm^2$ s) flow rates ($\approx 10^{-5}$ monolayer); and (3) a time constant of approximately 6 ms for inert gases; and (4) a large "pumping speed immunity", *i.e.* weak dependence of the ionizer region pressure to changes in the pumping speed at the turbo pump inlet. For gases that have large sticking coefficients on the wall, such as alcohol molecules, a flag was designed to allow the mass spectrometer cone to quickly open and close so that the response of the system could be measured. The response of the system to methanol is shown in Figure 2.2. The response time, which can not be more accurately extracted due to the limitation of the electronics, is less than 550 ms.

During adsorption, the surface was cooled to 140 K and positioned 1-2 mm away from the doser where the flux is uniform.[88] After dosing, the sample was rotated toward the mass spectrometer cone and positioned within 1 mm before starting the desorption experiment. Therefore, interference due to desorption from the wall, the edge of the tantalum block and the manipulator can be ruled out. Experimental data were acquired under computer control, recording up to eight masses.

Ultraviolet photoelectron spectroscopy (UPS) and x-ray photoelectron spectroscopy (XPS) measurements were made at normal emission with a hemispherical analyzer (Leybold EA-10). For XPS, the Mg Kα source (Perkin-Elmer, Φ 32-095) was operated at 15 keV and 100 W, incident at 45° with respect to the surface normal. The pass energy was fixed at 20 eV for detailed scans and at 100 eV for survey scans. For UPS measurements, a UV lamp (Leybold UVS 10/35) produced He (II) radiation (40.8

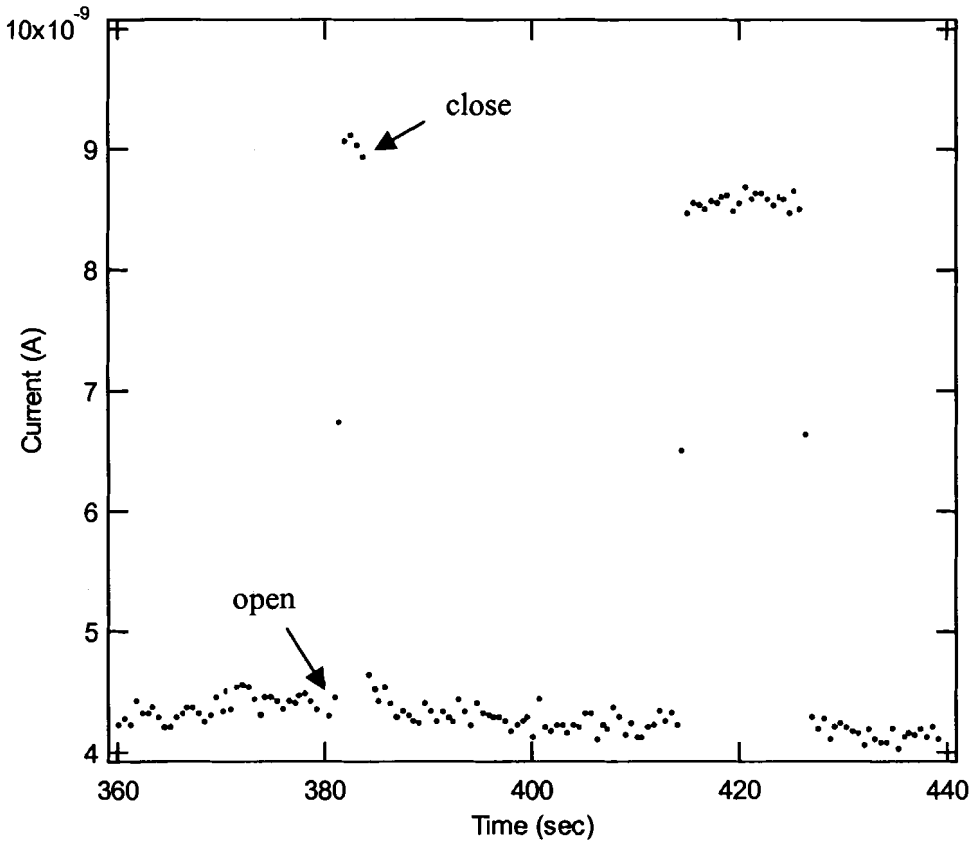


**Figure 2.2**. The response of the differentially pumped mass spectrometer system to methanol. The chamber was filled with methanol with the mass spectrometer cone closed by the flag to a pressure of $9.8 \times 10^{-8}$ torr in the main chamber and $9.8 \times 10^{-9}$ torr in the mass spectrometer region. The response was measured by immediately rotating the flag to open and close.

eV) incident at 45° and measurements were made at a pass energy of 10 eV, corresponding to a resolution of 0.2 eV.

Curve fitting of XPS spectra were performed in the freeware XPSPEAK 4.0 by Kwok using the sum of Gaussian and Lorentzian functions as the model function. During fitting, the peak area ratio of $W4f_{5/2}$ to $W4f_{7/2}$ was constrained to 0.78, based on the calculated cross sections by Scofield, [89] and the spin-orbit splitting was fixed at 2.1 eV.

## 2.2. Calibration of mass spectrometer

A microchannel array doser is aligned with the mass spectrometer. The doser is connected through a positive-shutoff (PSO) valve to a known-volume gas cell, whose pressure is monitored by a spinning rotor gauge. The effusion rate of the PSO valve ($10^{13}$ molecules $N_2$/s at $10^{-3}$ mbar) provides a flow rate comparable to the desorption rate in a typical desorption experiment. This dosing system can be used to calibrate the mass spectrometer, for compounds that don't stick to the doser, by monitoring the pressure in the gas cell vs. time.[88]

For sticky gases, the calibration of the mass spectrometer required a more complicated procedure. The flux impinging on the entrance aperture of the mass spectrometer shroud, $\Gamma = P/\sqrt{2\pi mkT}$, given by the kinetic theory of gases, is valid at the pressures utilized here. We assumed that the detector current, $I^{SEM} = I^F \cdot G$, is proportional to the flux, $I^{SEM} = c\Gamma$, where $I^F$ is the current measured with the Faraday plate and $G$ is the secondary electron multiplier (SEM) gain. Thus, the calibration factor, $c = (\frac{I^F}{P}) G\sqrt{2\pi mkT_{cal}}$, for a given mass fragment (at the chamber calibration temperature $T_{cal}$), includes the pumping speed through the ionizer (at the calibration temperature), the

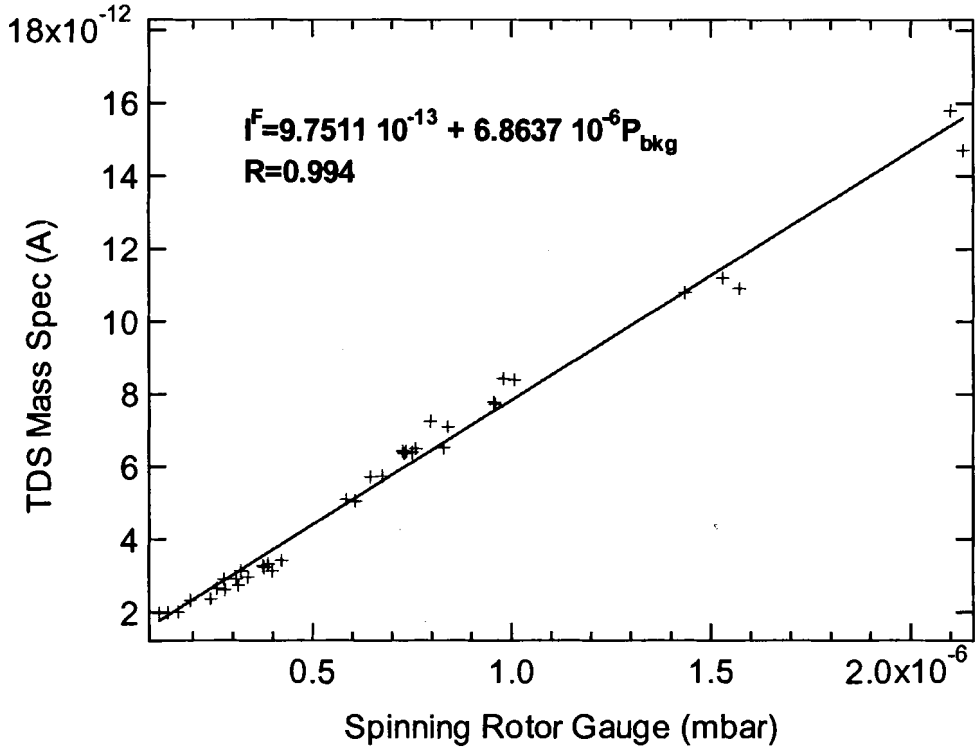


**Figure 2.3.** Calibration for DME comparing the Faraday plate current of the mass spectrometer with the spinning rotor gauge pressure. A similar calibration procedure was required for each compound.

ionization cross section, and the mass spectrometer's transmission efficiency. The detection efficiency is included in the SEM gain, measured on a day-to-day basis. Figure 2.3 shows the calibration of the mass spectrometer for DME using the spinning rotor gauge. The pressure is therefore converted to the flux in calculation of the calibration factor c.

### 2.3. $WO_3$ thin film and reagent treatments

The $WO_3$ thin films were grown epitaxially on the single crystal $\alpha$-$Al_2O_3(1\bar{1}02)$ substrate by RF magnetron sputtering of a pure tungsten target in a 50/50 oxygen/argon atmosphere at a total pressure of $4x10^{-3}$ mbar in a thin film deposition system.[67] The 500 Å films were grown at 1Å/sec with the substrate held at 773 K. The structure of the film and surface morphology have been studied [53,67] using reflection high energy electron diffraction (RHEED), X-ray diffraction (XRD), transmission electron microscopy (TEM) and scanning electron microscopy (SEM).

The $WO_3/Al_2O_3(1\bar{1}02)$ sample was mounted on a $1cm^2$ square tantalum block by spot welding thin tantalum foil strips over the edges of the sample. The tantalum block was then spot welded to 0.5 mm diameter Ta wires, which were welded to Ta rods. The rods were electrically isolated from a liquid nitrogen cooled copper block by a sapphire wafer (0.7 mm thick).

The sample could be resistively heated to 800 K and cooled to 140 K with this design. A K-type (Nickel-Chromium vs. Nickel-Aluminum) thermocouple was spot welded on the back of the tantalum block to monitor the sample temperature.

The major contaminant on the surface, after introducing the sample to the analysis chamber, was carbon. XPS showed a rather strong C1s peak before cleaning. The $WO_3(001)$ surface was cleaned by $Ar^+$ sputtering (100 μA beam current, 500 eV) until the C1s signal was reduced below the XPS detection limit. Meanwhile, sputtering preferentially removed lattice oxygen, resulting in the "reduced surface". The sputtered surface was treated in oxygen at approximately 0.2 mbar and 300 °C for 2 hours to produce the "oxidized surface". Oxygen (99.997%) and argon (99.9996%), both from Airco Specialty Gases, were used for oxidizing and sputtering the surface, respectively.

Methanol (EM Science, > 99.8%) was purified using freeze-pump-thaw cycles. The mass spectrum of the further purified methanol sample showed that the rise in the intensity at mass 18 due to water was less than 12% of the intensity at mass 31 of the most intense methanol fragment and that significant peaks due to other compounds were not observed. Ethanol (>99.5%) and isopropanol (99.5%) (Aldrich) were further treated by freeze-pump-thaw cycles and their purity was checked using the mass spectrometer before dosing onto the WO(001) thin film surfaces. Mass spectra for ethanol and isopropanol showed negligible water in both samples. Dimethyl ether (DME) (99.3%) from Specialty Gas Supply Inc. was used during experiments without further treatment. Dimethoxymethane (DMM) (Aldrich 99%) was further purified by freeze-pump-thaw cycles before dosing onto the $WO_3(001)$ thin film surfaces. The purity of DMM was checked with the mass spectrometer, which showed some intensity at masses 28, 29 and 30, assigned to formaldehyde contaminants that could not be entirely eliminated.

# SURFACE HETEROGENEITY AND DIFFUSION IN THE DESORPTION OF METHANOL FROM $WO_3$ (001) SURFACES

## 3.1. Introduction

Desorption from surfaces is a well-known and fundamental phenomenon in catalysis, widely used to study the energetics and kinetics of adsorption, desorption, and surface chemistry.[90] Although desorption spectra on metals typically focus on the decomposition reactions and desorption kinetics, the desorption process can be controlled by additional factors. These include surface diffusion, the surface heterogeneity, and the interaction between adsorbates, depending on the chemical properties of the adsorbates and the surface structures of the adsorbent.

The adsorption and desorption of methanol on different metal oxide surfaces have been extensively studied,[35,91-96] as the simplest alcohol, as a probe molecule for surface acidity, and as an important reagent for production of formaldehyde. Desorption of methanol is usually characterized by a large temperature span and a long tail on the high temperature side.[35,94,95] Surface diffusion, interactions between adsorbed methanol molecules, and the surface adsorption site heterogeneity may all play a role in producing this desorption profile. The surface heterogeneity results from metal oxides' sensitivity to the surface treatment and subsequent defect formation, such as oxygen vacancies and stepped structures.

Similar desorption features are widely observed for water adsorption on metal oxide surfaces.[97-103] However, there are only a few detailed studies of the role of the microscopic factors involved in the desorption process.[101-103] Most previous theoretical

simulations of desorption were limited to simple diatomic molecules on homogeneous metal surfaces assuming fast surface diffusion.[104,105]

In this chapter, we study the adsorption and desorption of methanol on the sapphire single crystal supported $WO_3(001)$ surfaces, using calibrated thermal desorption spectroscopy (CTDS) [88] combined with Monte Carlo simulations to explore the role of the surface heterogeneity, the interaction between the adsorbates, and the surface diffusion of adsorbates during desorption.

Pure $WO_3$ is a good insulator; however, it has been thoroughly studied as a semiconducting material,[106-109] since defects, particularly oxygen vacancies and crystallographic shear planes, can easily create variable tungsten oxidation states. In our laboratory, $WO_3$-based sensors have been studied for potential use in nerve agent (sarin and taban) detection,[71,110] using dimethyl methylphosphonate (DMMP) and other organophosphonates as simulants of these warfare agents.[81] The decomposition and loss of methoxy groups on $WO_3$ is similar to the surface chemistry of DMMP on other metal oxide surfaces.[74,76,78-80] However, knowledge of the decomposition products of the methoxy groups and details of the reaction mechanism on most surfaces is limited. In order to interpret the decomposition and reaction mechanism of DMMP on the $WO_3$ surface,[111] it was necessary to study the surface chemistry of methanol on $WO_3$. This also motivates the present study.

The experiments were performed on two different kinds of surfaces: the gently sputtered surface and the surface oxidized in oxygen after sputtering. X-ray photoelectron spectroscopy (XPS) was used to characterize the surface by monitoring the W4f and the valence band regions. Ultra-violet photoelectron spectroscopy (UPS) was used to

monitor the adsorption state of methanol on the $WO_3(001)$ surface. Calibrated thermal desorption spectroscopy (CTDS) was used to monitor the reaction products and quantify the absolute coverage during the desorption processes. This study shows that surface heterogeneity and diffusion play important roles in desorption of methanol. As far as the surface reaction was concerned, no other reaction products, for instance dimethyl ether, were detected.

### 3.2. Theoretical methods

We now describe the Monte Carlo model developed for the simulation. The catalytic surface was represented by a square L×L lattice of adsorption sites with periodic boundary conditions. The desorption rate for a molecule in the type $i$ local adsorption configuration is given by

$$rate_{\,i} = \nu_{d,i} \exp\left(-\frac{E_{d,i}}{k_B T}\right), \qquad (1)$$

where $\nu_{d,i}$ is the pre-exponential factor and $E_{d,i}$ is the activation energy of desorption, which is defined by

$$E_{d,i} = E_{d,i}^{\,0} + N_{nn,i}\, E_{nn}. \qquad (2)$$

Here, $E_{d,i}^{\,0}$ is the activation energy for desorption of an isolated molecule from site $i$, $N_{nn,i}$ is the number of nearest neighbor adsorbates of the $i^{th}$ molecule, and $E_{nn}$ is the interaction energy between nearest neighbors. Only the nearest neighbor interaction was considered in these simulations. The sign convention made for $E_{nn}$ is that $E_{nn}$ is positive for attractive interactions and negative for repulsive interactions. In the simulation, the pre-exponential factor, $\nu_{d,i}$ was assumed to be identical for all of the adsorbates with different local configurations. For a homogeneous surface model, all $E_{d,i}^{\,0}$ are identical, whereas

for a heterogeneous surface model, the $E_{d,i}^{0}$ values were randomly chosen from a distribution. For example, for a normal distribution, the mean $\overline{E}_d$ and standard deviation $\Delta E$ parameterized the distribution.

Diffusion and desorption were treated as two competitive surface processes. We controlled the relative diffusion and desorption rates by introducing a parameter $r = R/(R+1)$, where $R$ is the ratio of diffusion attempts to desorption attempts and $0<r<1$. This definition of r means that the probability of diffusion is higher for large $r$. $R$ is in principle determined by the difference of the activation energy between diffusion and desorption processes.

The Monte Carlo algorithm is formulated as follows:

(1) Randomly populate the L×L lattice sites with $N_0$ adsorbates at the initial surface coverage of $\theta_0$ ($\theta_0 = N_0/L^2$) and initial temperature $T_0$.

(2) Randomly choose a molecule on the lattice. Select a random number between 0 and 1 and attempt diffusion if it is less than $r$, or attempt desorption otherwise. For the diffusion test, step (3) will be performed, while for the desorption test, step (4) will be conducted.

(3) For the diffusion test of a chosen molecule, randomly choose a nearest neighbor site. If it is occupied, return to step (2). If it is empty, the molecule jumps into the new site if a random number between 0 and 1 is less than $exp(-\Delta E/kT)$, where an energy difference, $\Delta E < 0$, corresponds to a favorable jump between the chosen nearest neighbor site and the initial site. Then return to step (2).

(4) For the desorption test, the desorption probability was calculated by

$$p_{d,i} = \nu_{d,i} \exp(-\frac{E_{d,i}}{kT})\Delta t \qquad (3)$$

where the time step $\Delta t$ was decreased until the shape of the spectrum converged. A linear program was used for the temperature, $T=T_0 + \beta\Delta t$, where $\beta$ is the ramp rate. Desorption occurs if a random number between 0 and 1 is less than $p_{d,i}$. The desorption tests were counted by a parameter, $m_{trial}$, which was set equal to the number of adsorbates on the lattice at the beginning of each temperature step, and $m_{trial}$ was decreased by 1 for each desorption attempt (whether a desorption event occurs or not). Once $m_{trial}$ desorption attempts were tested, the temperature was increased by $\Delta T = \beta\Delta t$. Since the diffusion test does not affect the rate that the surface temperature increases, the ratio $R$ controls the extent to which surface equilibrium can be established. The desorption rate was calculated by $R=\Delta N/\Delta t$, where $\Delta N$ is the number of molecules that desorb. The simulation was conducted in MathCad version 2000. Initial simulations utilized lattices with 100×100 sites, but larger, 200×200 lattice sizes were then used for production runs. The time step was varied between 0.1 and 0.5 s to test convergence of the algorithm. For $\Delta t \geq 0.5$ s, significant peak shifts were observed; therefore, a time step of $\Delta t = 0.2$ s was utilized for the spectra shown. Comparisons were also made to direct numerical solution of the corresponding Polanyi-Wigner equation for appropriate cases (*i.e.* in the rapid diffusion limit).

## 3.3. Results

### 3.3.1. Experimental results

#### 3.3.1.1 Characterization of the $WO_3$ films after initial growth

Previous studies in our laboratory show that the structure, the stoichiometry, and the electrical properties of $WO_3$ films grown on r-cut sapphire substrates are very sensitive to the growth conditions. Reflection high energy electron diffraction (RHEED) in transmission and glancing incidence X-ray diffraction (XRD) show that the $WO_3$ films made at the conditions described above are grown in the highly oriented monoclinic phase with the (001) planes (of the nearly cubic structure) parallel to the sapphire substrate surface.[53,66,67] Scanning electron microscope (SEM) images of the cleaved edge of the film show that the film, as deposited, is very dense, while TEM measurements indicate that pores, if present, are less than 1 nm in width.[53] However, heavily stepped structures and domains were observed in scanning tunneling microscope (STM) images.[67] Annealing in oxygen at high temperatures can smooth the surface significantly.[67] Before CTDS experiments, the surface was heated at 4 K/s to 800 K in vacuum several times until no desorption was observed.

#### 3.3.1.2. XPS characterization of the $WO_3$(001) surfaces

Two types of surface were produced for this study: the sputtered surface and the oxidized surface, which was produced by treatment of the sputtered surface in oxygen at high temperature. XPS was employed to characterize these surfaces by analyzing the W4f and valence band regions.

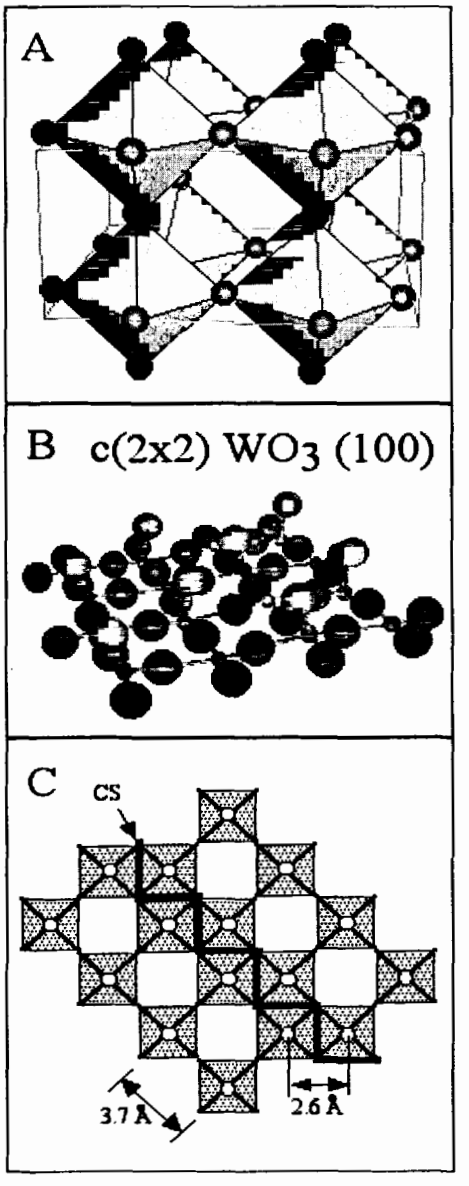


**Figure 3.1.** $WO_3$ structure, the ideal (100)/(001) plane structure and crystallographic shear (CS) boundaries. A) Structure of monoclinic $WO_3$ shown as corner sharing octahedra. Small tilting and distortions of the octahedra result in the $W_4O_{12}$ unit cell shown. B) A model of the c(2×2) non-polar structure $WO_3$(001) surface (periodicity referenced to the idealized, cubic $ReO_3$ structure). C) Illustration of the approximately 3.7 Å W-O-W distances in the $WO_3$(001) face, and the shorter (~2.6 Å) W-W distances at CS boundaries (indicated by heavy line).

Two types of oxygen exist on the bulk terminated (001) surface, terminal oxygen and bridging oxygen. Figure 3.1A shows the structure of monoclinic $WO_3$. Because the deviations from the cubic $ReO_3$ structure are very small ($\beta = 90.9°$; a = 0.730 nm, b = 0.754 nm, c = 0.769 nm),[112,113] the (001), (010) and (100) orientations are present in the epitaxial film; however, the (001) face is prevalent. [67] As in previous single crystal studies, [47,50] we refer all surface structures to the idealized cubic structure and make no distinction between the (100), (010) and (001) surfaces. In the non-polar c(2×2) surface, shown in Figure 3.1B, half of the terminal oxygens are removed, to produce a stable, charge neutral surface.[109,114] Sputtering may preferentially remove oxygen, either in the terminal or bridging positions, to result in a reduced, disordered surface. Formally, the five-coordinate tungsten cations, with missing terminal oxygens, are in the 5+ oxidation state. However, annealing the surface would also be expected to produce shear plane structures, which also result in reduced formal cation oxidation states. At shear plane boundaries (see Figure 3.1C), in which an octahedron has two corner sharing and two edge sharing octahedra neighbors, the cations would also be in a 5+ formal oxidation state. Removal of the terminal oxygen from the cation at the shear plane would formally produce a 4+ oxidation state.

Figure 3.2A shows a W4f XPS spectrum for the epitaxially grown film following introduction to the analysis chamber. Only the $W^{6+}$ spin orbit doublet contributes to the spectrum. The W4f XPS spectra for the ion sputtered or thermally treated surfaces (Figure 3.2 B, C, D) are complicated by the emergence of new bands in the lower binding energy region, whose intensity depends upon the extent of surface treatments. At present, two mechanisms have been proposed to interpret the W4f spectrum.

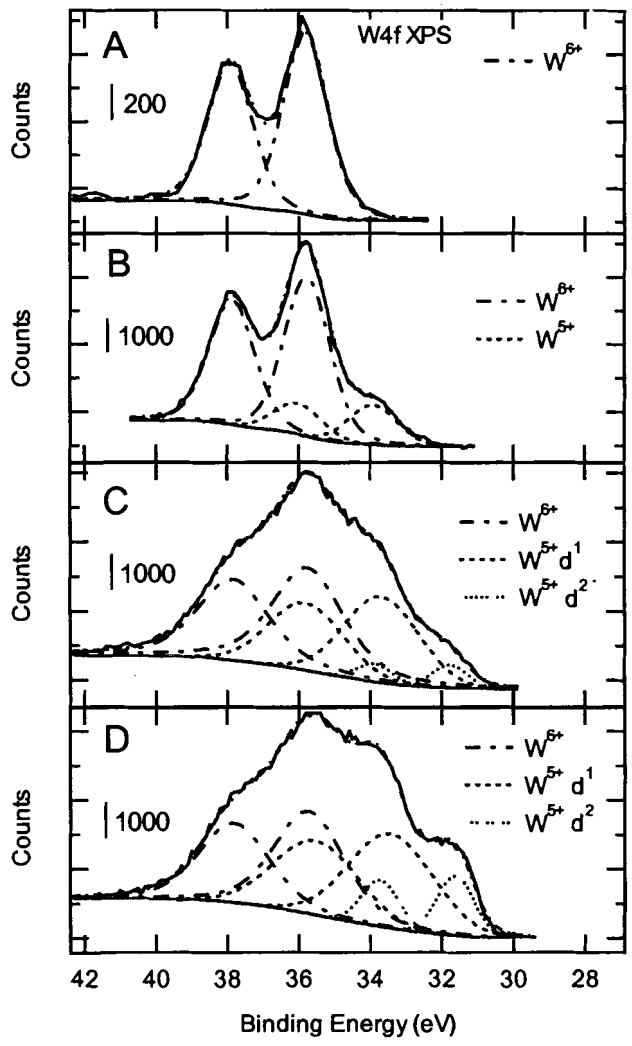


**Figure 3.2** W4f XPS spectra for $WO_3$(001) surfaces treated under different conditions and their fitts by the final state model. A) The W4f XPS spectrum of a fully oxidized $WO_3$ film (solid line) after growth and introduction to the analysis chamber. B) The spectrum for a $WO_3$ film after sputtering and oxidation in 0.24 mbar $O_2$ at 300 °C for 2 hours fit with $W^{6+}$ and $W^{5+}$ $d^1$ final state spin-orbit split doublets (dashed curves). C) The spectrum of an $Ar^+$ sputtered (500 eV, 100 μA beam current, 110 secs) $WO_3$ surface fit with $W^{6+}$, $W^{5+}$ $d^1$, and $W^{5+}$ $d^2$ final state spin-orbit split doublets (dashed curves). D) The spectrum of a heavily sputtered surface fit with $W^{6+}$, $W^{5+}$ $d^1$, and $W^{5+}$ $d^2$ final state spin-orbit split doublets (dashed curves). The peak parameters for fits to the final and initial state models are given in Tables 3.1 and 3.2, respectively.

**Table 3.1.** Parameters obtained from fitting the final state model.

| Surface studied | Oxidation state | Binding energy ($W4f_{7/2}$) (eV) | FWHM (eV) | Surface composition (%) |
|---|---|---|---|---|
| As-grown | $W^{6+}$ | 35.7 | 1.46 | |
| Oxidized after Sputtering | $W^{5+}$ | 33.9 | 1.61 | 19 |
| | $W^{6+}$ | 35.8 | 1.50 | 81 |
| Reduced | $W^{5+}$ $d^2$ | 31.8 | 1.15 | |
| | $W^{5+}$ $d^1$ | 33.7 | 2.46 | 44 |
| | $W^{6+}$ | 35.7 | 2.36 | 56 |
| Heavily reduced | $W^{5+}$ $d^2$ | 31.6 | 1.21 | |
| | $W^{5+}$ $d^1$ | 33.4 | 2.76 | 55 |
| | $W^{6+}$ | 35.7 | 2.33 | 45 |

**Table 3.2.** Parameters obtained from fitting the initial state model.

| Surface studied | Oxidation state | Binding energy ($W4f_{7/2}$) (eV) | FWHM (eV) | Surface composition (%) |
|---|---|---|---|---|
| As-grown | $W^{6+}$ | 35.7 | 1.46 | |
| Oxidized after sputtering | $W^{4+}$ | 33.8 | 1.52 | 18 |
| | $W^{5+}$ | 35.5 | 1.52 | 20 |
| | $W^{6+}$ | 35.8 | 1.46 | 62 |
| Reduced | $W^{0}$ | 31.7 | 1.02 | 10 |
| | $W^{4+}$ | 33.7 | 2.34 | 34 |
| | $W^{5+}$ | 35.5 | 2.10 | 11 |
| | $W^{6+}$ | 35.8 | 2.40 | 45 |
| Heavily reduced | $W^{0}$ | 31.6 | 1.12 | 29 |
| | $W^{4+}$ | 33.7 | 2.59 | 29 |
| | $W^{5+}$ | 35.6 | 2.25 | 17 |
| | $W^{6+}$ | 35.8 | 2.44 | 25 |

The first mechanism, which originates from many body effects, supposes that, when the electrostatic interaction between the core hole, after photoionization, and an electron in the conduction band,[115] is strong enough to exceed the width of the conduction band, the conduction band state can be pulled down into the gap to form a localized state, trapping the conduction electron. Two final states can be evolved, depending on the occupancy of the localized state; if the trap is occupied, final state screening results in a lower apparent binding energy (*i.e.* the "screened" final state) compared to the "unscreened" final state in the case when the trap is empty. For this mechanism, two final states are possible from the same initial oxidation state, and the relative intensity and shift are dependent upon the electron density near the Fermi level.[116]

The second mechanism assigns the features to different initial states. Lower oxidation state tungsten species are assigned to $W^{5+}$ and $W^{4+}$, following mild ion sputtering or thermal treatment, and additionally, metallic $W^0$ from extensive sputtering.[107,117-120] Hence, in this mechanism the W4f spectrum is fit with up to four different spin-orbit doublets representing different *initial* states (formally $W^{6+}$, $W^{5+}$, $W^{4+}$, and $W^0$).

The final state screening mechanism has been favored for interpretation of core level XPS spectra for sputtered and annealed $WO_3(001)$ single crystal surfaces which were also characterized by LEED and STM.[50] Dixon, *et al.* [50] found that significant differences above the valence band (*i.e.* in the gap of stoichiometric $WO_3$), as measured with UPS, could be correlated with formation of "troughs" running across the c(2×2) terraces and regions of high tunneling probability ("bright rafts") on more reduced surfaces.[50]

Figures 3.2 B, C and D show W4f XPS spectra for the oxidized, reduced, and heavily sputtered surfaces, respectively. We note first that the spectra can be fit in a manner consistent with both the final state screening mechanism and the initial state model. The spectrum of the oxidized surface, shown in Figure 3.2B, was fit with two spin-orbit doublets, assigned to the $d^0$ final state of $W^{6+}$ ($W4f_{7/2}$ BE=35.8 eV) and the unscreened $d^1$ final state of $W^{5+}$ ($W4f_{7/2}$ BE = 33.9 eV). The spectra in Figure 3.2C and 2D were fit with three spin-orbit doublets, assigned to the $d^0$ final state of $W^{6+}$ ($W4f_{7/2}$ BE=35.7 eV), the unscreened $d^1$ final state of $W^{5+}$ ($W4f_{7/2}$ BE = 33.7 eV) and the screened $d^2$ final state of $W^{5+}$ ($W4f_{7/2}$ BE = 31.8 eV). The results of the final state model are given in Table 3.1. Small contributions from the W 5p level were neglected.[116]

The W4f XPS spectrum shown in Figure 3.2B can be fit equally well with three doublets (*cf.* two in the final state model) assigned to $W^{6+}$, $W^{5+}$ and $W^{4+}$ based on the initial state mechanism. Likewise, the spectra in Figure 3.2C and 2D can be fit with four doublets (*cf.* three in the final state model) assigned to $W^{6+}$, $W^{5+}$, $W^{4+}$ and metallic $W^0$. These fits are not shown, but the results are given in Table 3.2.

Valence band spectra, measured with He II radiation, compare very well in shape and relative intensity to data shown by Dixon, *et al.*[50] The UPS valence band spectrum corresponding to our Figure 3.2B is essentially identical to the spectrum in Figure 9a of Ref 49 for the c(2x2) surface with troughs (the STM image in Figure 2a of Ref 49), while that corresponding to our Figure 3.2C is very similar to the UPS spectrum in Figure 12 a of Ref 49 for their sputtered and annealed surface (and the STM image shown in Figure 2b of Ref 49). The similarity of our XPS and UPS data to that of Dixon, *et al.*, and estimates of the substoichiometry, $x$, in $WO_{3-x}$, based upon considerations given by

Chazalviel, *et al.* [116] lead us to favor the final state model, for reasons discussed further below. Regardless of interpretation, the spectra of Figure 3.2B and 3.2C and corresponding UPS valence band regions uniquely characterize the surfaces that were used for the methanol adsorption and desorption experiments.

### 3.3.1.3. Adsorption state of methanol on $WO_3$(001) surfaces

UPS is a convenient technique to study the adsorption state of methanol. Five bands can be identified for the molecular adsorption of methanol in UPS using a He II source, which are assigned to the 2a″, 7a′, 6a′, 1a″, and 5a′ molecular orbitals within the $C_s$ point group.[121] If a methoxy group, with higher, $C_{3v}$ symmetry, is formed via dissociation of methanol, then the 2a″and 7a′, and the 1a″ and 5a′ orbital pairs become degenerate, which are assigned to the 2e and 1e orbitals, respectively, and 6a' is designated as the totally symmetric $5a_1$ orbital.[122,123] Therefore, only three bands are observed for the methoxy group.[93,124]

UPS difference spectra of methanol adsorption on the $WO_3$(001) surfaces are shown in Figure 3.3. Figure 3.3A shows the spectra for methanol adsorption on the sputtered $WO_3$(001) surface as a function of coverage and temperature. For multilayer adsorption, at a coverage of 1.5 ML and 140 K, five peaks are detected at 5.8 eV (2a″), 7.5 eV (7a′), 10.2 eV (6a′), 11.9 eV (1a″), and 17.4 eV (5a′) associated with the molecular orbitals of methanol. This observation is consistent with the results for methanol adsorption on the aluminum oxide surface,[93] on Cu(110),[125] and on the aluminum surface,[126] suggesting molecularly adsorbed methanol. However, the five bands evolve into three bands at 5.8 eV (2e), 10.2 eV ($5a_1$), and 17.4 eV (1e) assigned to

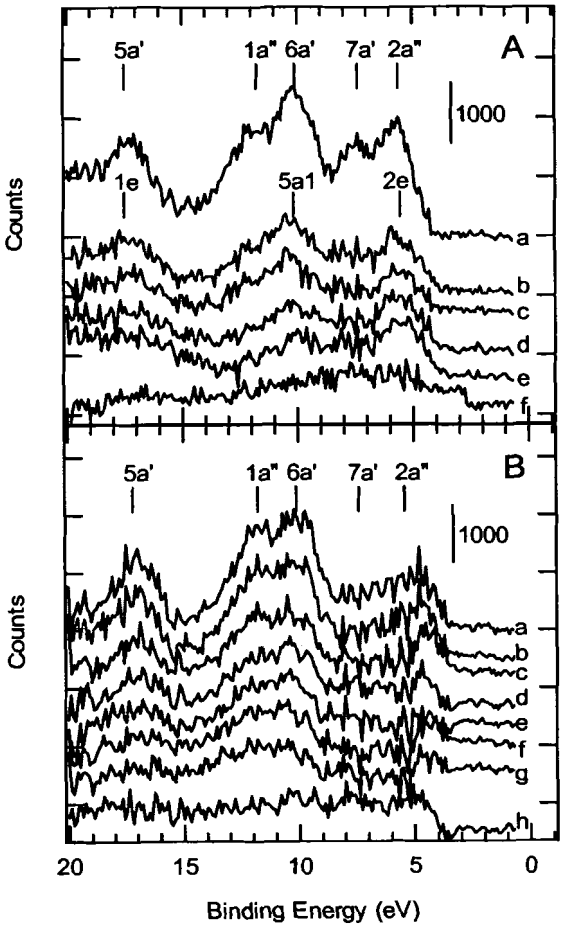


**Figure 3.3** UPS difference spectra for methanol adsorption on $WO_3(001)$ surfaces. A) UPS difference spectra following adsorption of methanol on the reduced $WO_3(001)$ surface at temperatures and absolute coverage of: a) 140 K; 1.5 ML; b) 186 K; 0.60 ML; c) 205 K; 0.55 ML; d) 250 K; 0.27 ML; e) 310 K; and f) 500 K; and B) UPS difference spectra following adsorption of methanol on the oxidized $WO_3(001)$ surface after sputtering at temperatures and coverage of : a) 140 K; 1.1 ML; b) 160 K; 0.83 ML; c) 187 K; 0.50 ML; d) 195 K; 0.42 ML; e) 205 K; 0.40 ML; f) 220 K; 0.26 ML; g) 250 K; 0.12 ML; and h) 310 K; 0.03 ML. The UPS and corresponding coverage measurements were conducted separately.

methoxy, for sub-monolayer adsorption at surface temperatures above 186 K. The decrease in the intensity of the 1a" peak at 186 K, and further reduction in intensity by 250 K, suggests that a majority of the methanol dissociates into methoxy on the reduced surface (Figure 3.3 A, spectra b-e). All of the bands disappeared by 500 K.

UPS spectra for methanol adsorption on the oxidized $WO_3$ surface are shown in Figure 3.3B. Four bands can be identified at 5.5 eV, 10.2 eV, 11.8 eV, and 17.1 eV for the multilayer adsorption at 140 K. Compared with the UPS spectra for adsorption on the sputtered surface, the intensity of the peak at 5.5 eV is greatly suppressed, and the band at 7.5 eV due to the lone pair electrons on the methanol oxygen atom, observed for the reduced surface, cannot be resolved. This phenomenon was also observed for adsorption of methanol on the zinc terminated ZnO(0001) surface in a study by Hirschwald and Hofmann,[127] who suggest that the lone pair electrons on the oxygen atom are strongly perturbed in the adsorption state, due to interaction of the methanol oxygen atom with cation sites. With increasing surface temperature, the UPS spectrum does not change in character. Thus, the UPS spectra for the oxidized surface suggest that methanol adsorbs molecularly both in the multilayer and sub-monolayer adsorption regimes.

### 3.3.1.4. Thermal desorption of methanol on $WO_3$(001) surfaces

Figure 3.4 shows coverage dependent desorption spectra of methanol on the $WO_3$(001) surfaces. In all of the experiments, the fragmentation pattern agreed with methanol. Although a range of mass fragments were monitored, including 28, 29, and 30 (formaldehyde), 29, 45, and 46 (dimethyl ether), 28 (CO) and 44 ($CO_2$), no other products were observed. With the sputtered surface, the peak desorption temperature is

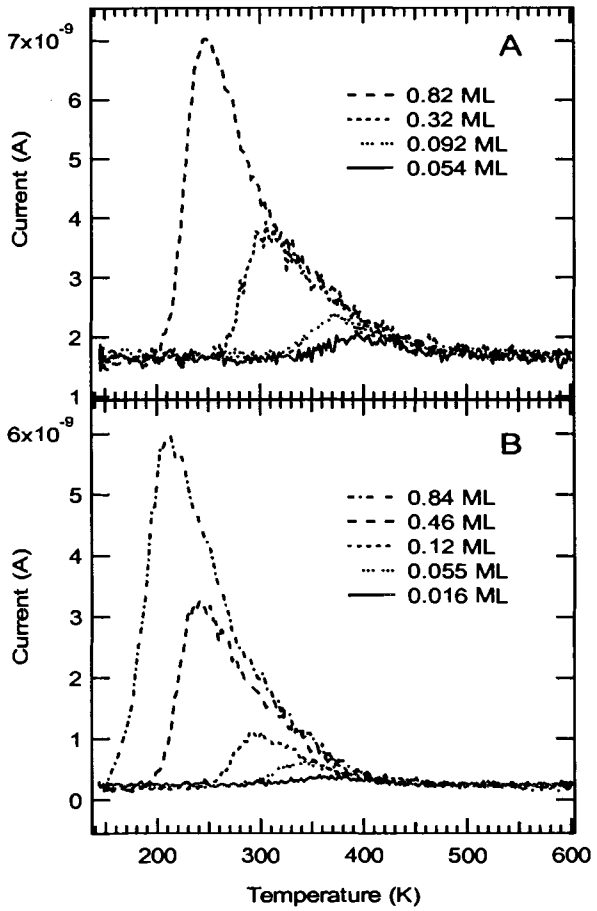


**Figure 3.4**. Thermal desorption spectra of methanol (31 amu signal) on A) reduced $WO_3(001)$ surface; and B) oxidized $WO_3(001)$ surface. Dosing of methanol was performed at 140 K through a microarray doser, and the temperature ramp rate was 4 K/sec.

at 390 K for a coverage of 0.054 ML, where 1 monolayer (ML) is defined to be $10^{15}$ molecules/cm$^2$, and decreases with increasing surface coverage, as shown in Figure 3.4A. For the oxidized surface, the desorption temperature is at 360 K for a coverage of 0.016 ML and decreases with increasing surface coverage, as shown in Figure 3.4B. The desorption features of methanol on sputtered and oxidized $WO_3$ surfaces show similar behavior in that, with increasing coverage, the peak temperature decreases but the high temperature side of all of the spectra overlap. Similar spectra have been observed for both single crystal and polycrystalline oxide surfaces for water [101-103] and methanol.[94,95] This common behavior could be attributed to the desorption process, or possibly limitations of the conductance of thermal desorption spectrometers used by a number of groups in studying $H_2O$ and alcohol desorption, since these compounds adsorb on the UHV system walls.

Although the mass spectrometer is housed in a separately differentially pumped section of the UHV system and the pumping time constant for inert gases is designed to be 6 ms,[88] the pumping speed for sticky gases is not easy to predict. Therefore, we constructed a viton shutter that could be rotated rapidly into position to close the aperture of the mass spectrometer shroud. Methanol was admitted to the UHV chamber, creating a pressure difference of an order of magnitude between the sample and mass spectrometer housing regions. The shutter was opened and closed, and the mass spectrometer current responded too quickly to measure with the present electronics, placing an upper limit for the methanol pumping time constant at 550 ms. Compared to the 10 to 25 s width of the desorption curves, the shape is not significantly broadened by the mass spectrometer electronics or differentially pumped housing conductance.

### 3.3.2. Theoretical results

Monte Carlo simulations on homogeneous surfaces have been studied by other groups.[104,105] Because the barrier to diffusion for simple adsorbates is typically 10% of the desorption barrier, most simulations have included a diffusion step to equilibrate the surface between desorption steps. However, experimental evidence for desorption of $H_2O$ from $Al_2O_3(0001)$ [103] suggests that diffusion can be much slower than desorption on at least some oxide surfaces. Therefore, we investigated the affect of the relative rates of diffusion vs. desorption on the coverage-dependent shape of the desorption curves. We focussed on desorption from the oxidized surface since UPS shows that the methanol is molecularly adsorbed at all coverages and temperatures. Therefore, a first order, molecular desorption process is justified.

The decrease in desorption temperature with increasing coverage, also observed for $H_2O$ on the $TiO_2(110)$ surface,[101] has been interpreted as due to repulsive interactions. However, to achieve a sufficiently large temperature shift at desorption temperatures of 200-400 K, the repulsive interaction causes a splitting at high coverage. The simulation for rapid diffusion and repulsive interactions in the homogeneous surface model, illustrated in Figure 3.5A, is similar to previous studies [104] but is not consistent with the experimental behavior. When diffusion is negligible, the desorption curves show a markedly different character, as shown in Figure 3.5B. For lower coverage, the peaks tail to lower temperature, but at higher coverage, the additional repulsive interaction between neighbors leads to a second peak. Thus, evaluation of the repulsive interaction model on

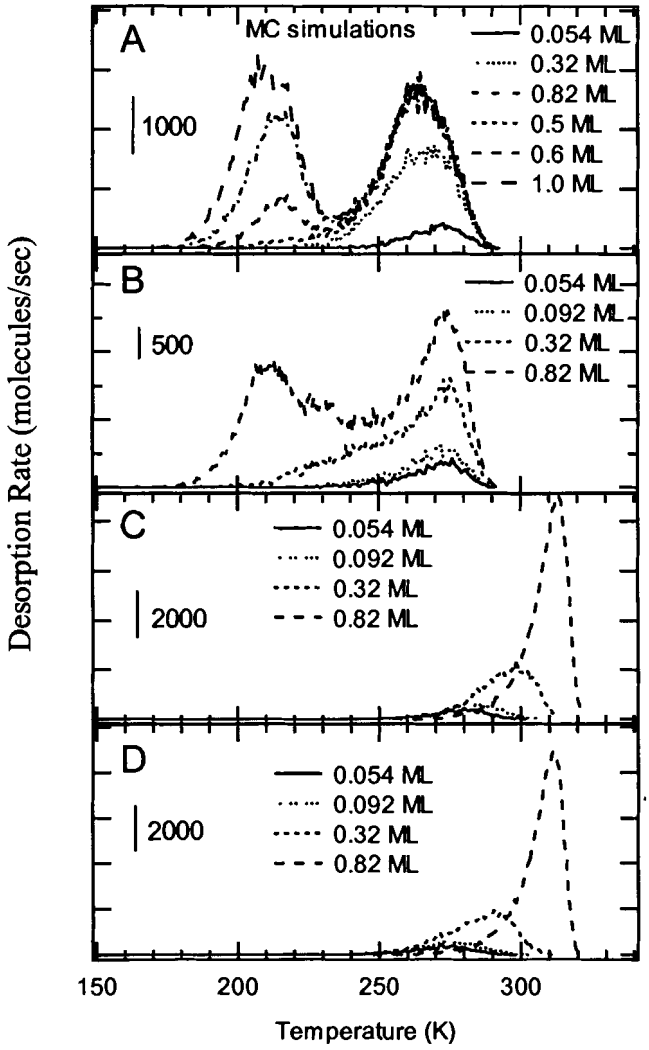


**Figure 3.5.** Monte Carlo simulations of molecular desorption on a homogeneous surface at various coverages, as indicated in the panels. A binding energy of 70 kJ/mol, ramp rate of 4 K/sec, and a preexponential factor $\nu = 10^{13}$ $sec^{-1}$ were assumed with A) rapid surface diffusion and a repulsive interaction of 4 kJ/mol between adsorbates; B) negligible surface diffusion and a repulsive interaction of 4 kJ/mol between adsorbates; C) rapid surface diffusion and an attractive interaction of 4 kJ/mol between adsorbates; and D) negligible surface diffusion and an attractive interaction of 4 kJ/mol between adsorbates.

a homogeneous surface cannot explain our methanol results and similar data,[35,94,95,101-103] with either rapid or negligible diffusion.

Because we expect hydrogen bonding interactions between methanol molecules (or water) to be attractive, and the case of negligible diffusion has not been previously reported, we compare in Figures 3.5C and D the cases of rapid and negligible diffusion, respectively. As expected, the desorption peaks shift to higher temperature with increasing coverage, which is qualitatively different from the methanol desorption behavior. Note that when diffusion is rapid compared to desorption (Figure 3.5C), the behavior can also be described by half order desorption, but for the slow diffusion case, the curves are qualitatively different.

Nelson, *et al.* [103] analyzed their data for $H_2O/Al_2O_3(0001)$ using a distribution of adsorption sites for the case in which the sample was exposed to saturation coverage and then annealed to remove the weaker bound species. We have simulated a distribution of adsorption sites and varied the ratio of the diffusion vs. desorption rates. The results show that even relatively low rates of diffusion are sufficient to keep the surface near equilibrium.

Figure 3.6 shows the results of Monte Carlo simulations of first order desorption on a heterogeneous surface. The surface site binding energies were described by a normal distribution with an average energy of 70 kJ/mol and a standard deviation of 6 kJ/mol. A temperature ramp rate of 4 K/sec and a desorption pre-exponential factor, $\nu = 10^{13}$ $sec^{-1}$ were used. Figure 3.6A shows the simulation results for increasing surface coverage with both the interactions between adsorbates and surface diffusion negligible. As can be seen, the desorption temperatures do not change with surface coverage and random population leads to a similar shape for all coverages. By contrast, Figure 3.6B shows a simulation in which the adsorbate interaction is neglected, but diffusion is

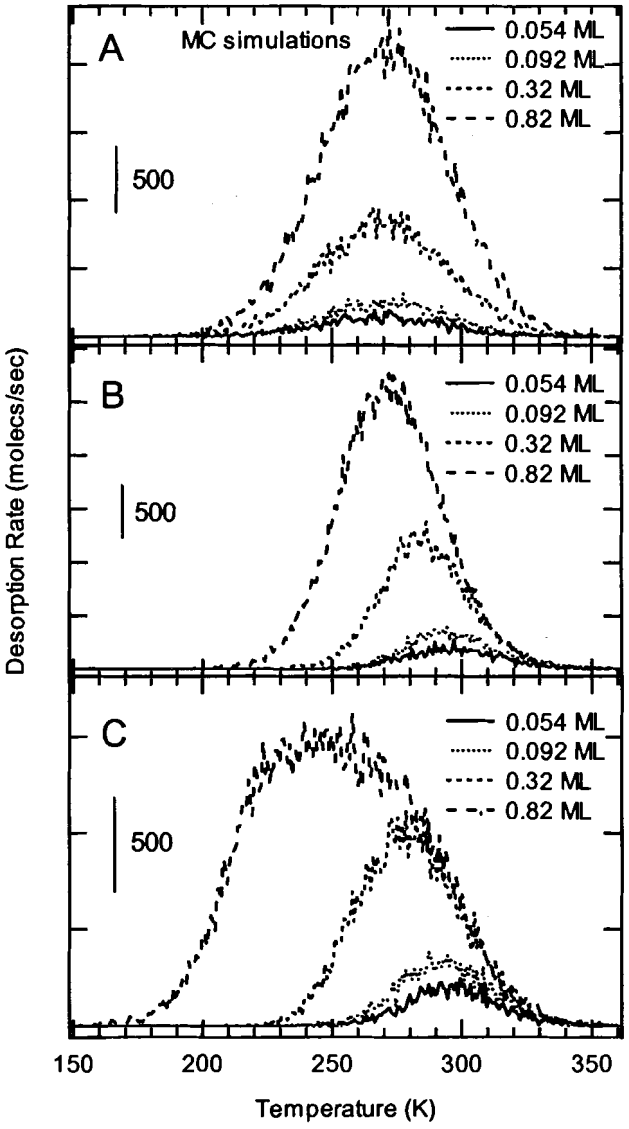


**Figure 3.6** Monte Carlo simulations of the first order desorption on a heterogeneous surface. A normal distribution of the surface sites with the mean of 70 kJ/mol and standard deviation of 6 kJ/mol, with the ramp rate equal to 4 K/sec, and a preexponential factor $\nu = 10^{13}$ $sec^{-1}$ were assumed for the indicated coverages with A) negligible surface diffusion and no interactions between adsorbates; B) negligible interactions between adsorbates but with rapid surface diffusion; C) rapid surface diffusion and repulsive interactions of 3 kJ/mol between adsorbates.

sufficiently fast that an equilibrium adsorption state can be established before every desorption event. The simulations with rapid diffusion produce desorption spectra with overlapping high temperature tails, which are qualitatively similar to the experimental observations shown in Figure 3.4. A simulation similar to that in Figure 3.6B, but with a repulsive interaction of 3 kJ/mol is shown in Figure 3.6C. The repulsive interaction causes the desorption temperature to shift to lower temperature, compared with the results in Figure 3.6B, but results in a flat topped or split peak at higher coverage. If attractive interactions, *e.g.* hydrogen bonding between adsorbed methanol molecules, are introduced on the heterogeneous surface, the desorption temperature increases with the coverage as expected (spectra are not shown here). Therefore, a model with an attractive interaction is not compatible with desorption of methanol on these $WO_3$ surfaces.

While the simulations of desorption with a normal distribution of surface site energies shown in Figure 3.6B produce similar desorption spectra to the experimental results shown in Figure 3.4 in terms of the coverage dependence of desorption temperature and overlapped trailing edge, the extent of coverage dependence of the desorption temperature is far from the experiment observations. A surface site energy distribution, with which the theoretical desorption spectra under the same condition as shown in Figure 3.6B is close to the experimental results on the oxidized surface, is shown in Figure 3.7. Figure 3.8 presents the corresponding simulations of desorption spectra and the experimental desorption spectra on the oxidized surface for comparison.

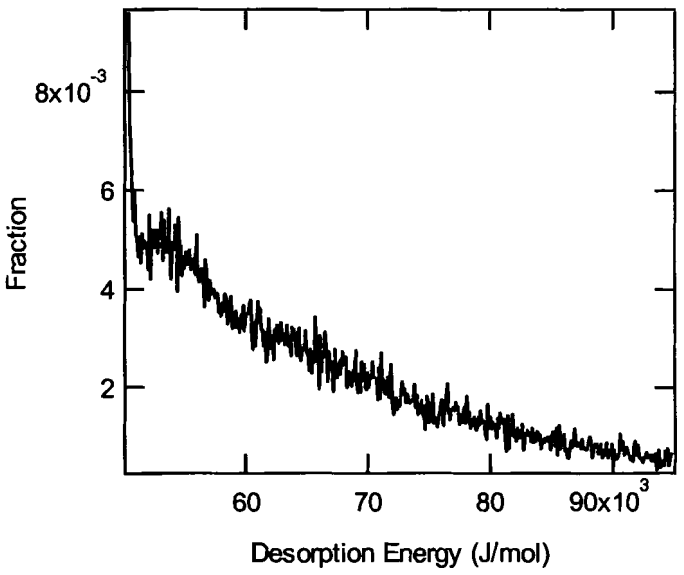


**Figure 3.7**. The distribution of surface site energies that gives rise to theoretical desorption spectra similar to experimental observations under the conditions of negligible intermolecular interactions and rapid diffusion. The distribution was first based on variation of desorption energies, obtained from a leading edge analysis of the series of methanol desorption traces at different coverage. The distribution was then refined by solving the Polanyi-Wigner equation and comparing to the experimental data. Finally, the distribution was used in the Monte Carlo simulation.

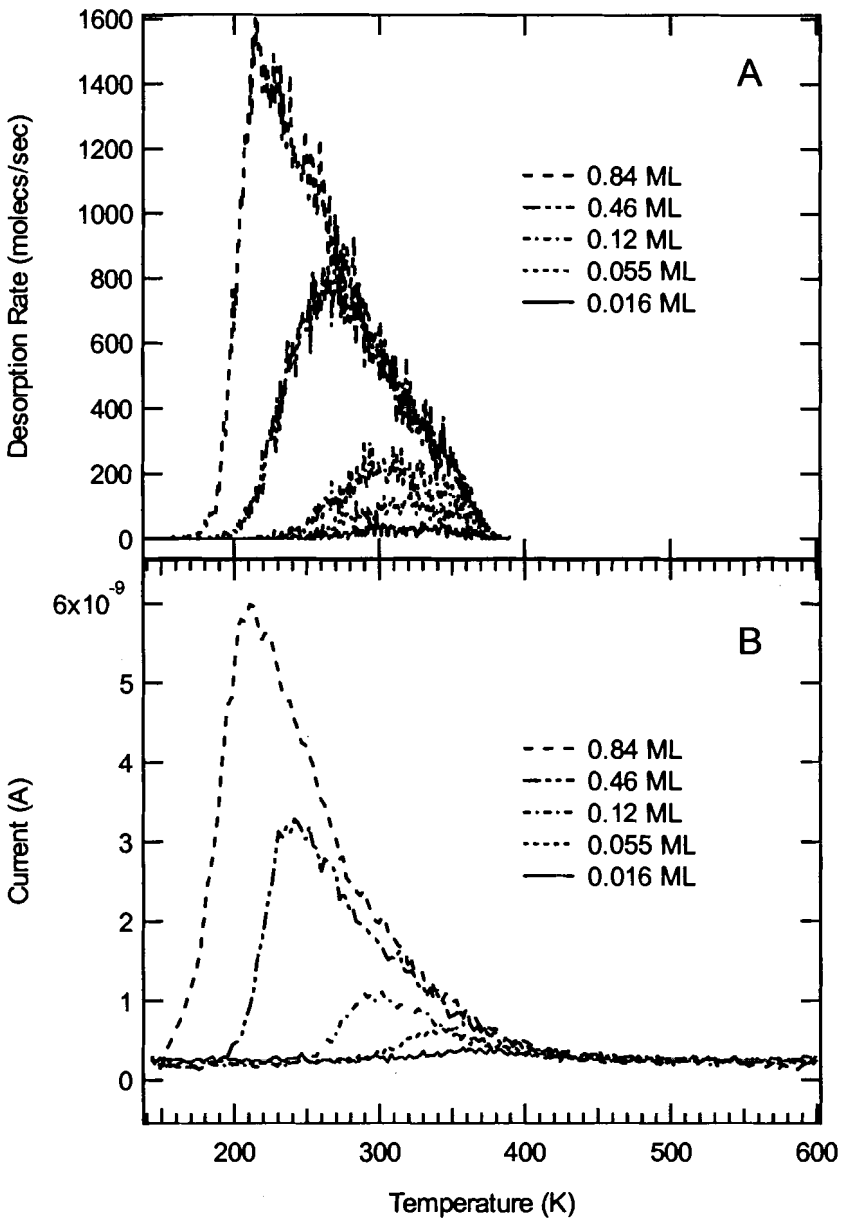


**Figure 3.8**. Comparison of the Monte Carlo simulation spectra with methanol desorption spectra on the oxidized $WO_3(001)$ surface. A) The simulations of desorption spectra with the surface site energy distribution shown in Figure 3.7 at different coverage. B) The methanol CTDS on the oxidized $WO_3(001)$ surface.

## 3.4. Discussion

### 3.4.1. Adsorption site and species

Dixon, *et al.* have studied the electronic states of the single crystal $WO_3(001)$ surface following treatments of sputtering and annealing using photoelectron spectroscopy combined with STM.[50] The close correspondence between the XPS and UPS spectra for the $WO_3(001)$ surfaces in our study with the data given by Dixon, *et al.*, together with the similarity in surface treatments, provides some basis for structural characterization of our surfaces. Based on their STM studies, we are able to associate the reduced surface with the (1×1) structure with most of the terminal oxygen removed and the oxidized surface with the c(2×2) structure with troughs.

Previous studies have revealed that methanol adsorbs on metal oxide surfaces with oxygen bound to coordinatively unsaturated cation sites via lone pair electrons.[128] On the oxidized surface, the change in intensity of the 7a' and 2a" molecular orbitals localized on the oxygen atom (as shown in the UPS spectra of Figure 3.3) is strong evidence for interaction with a Lewis acid site. The five-coordinate, formally $W^{5+}$ sites of the c(2x2) surface, as well as cations in the troughs, whose detailed structure remains unclear, are both possible Lewis acid sites. Our ability to calibrate the desorption spectrum and give absolute coverages allows us to determine that the large majority of exposed cation sites on the oxidized surface act as Lewis acid sites. Noting that the coverage of methanol in Figure 3.3B, curves a and b, is a full monolayer and yet the emission from the 7a' and 2a" molecular orbitals remains suppressed shows not only that trough sites may act as Lewis acid sites but also the majority c(2x2) sites must be relatively strong Lewis acid sites. The presence of strong Lewis acid sites on

dehydroxylated, high surface area $WO_3$ powders has also been found by work in our laboratory by the Tripp group, using pyridine as a probe molecule.[129]

Despite evidence for strong Lewis acid sites, we found that dissociation did not occur on the oxidized surface. Dissociation of this weak Brønsted acid requires a pair of acid/base sites, in which a lattice oxygen atom acts as the Brønsted base site. Both bridging and terminal oxygen atoms are possible Brønsted base sites. The inactivity of the oxidized surface implies that the basicity of the surface oxygen is too low to dissociate the hydroxyl group. Some evidence supporting this argument can be found in the study of adsorption of $H_2O$ on the $Na_xWO_3(001)$ surface using HREELS.[130] It was found that water molecularly adsorbed on the tungsten bronze (001) surface with the oxygen end bonded to the tungsten cation, but no dissociation was detected. Since water has a significantly higher acidity than methanol, we can conclude that the oxidized surface has only weak Brønsted acid sites.

This observation can be understood from the surface structure of the oxidized surface. The five coordinate $W^{5+}$ sites are the majority adsorption sites on the oxidized surface for methanol, and therefore the bridging oxygen is the closest potential Brønsted base site. However, the bridging oxygen is bonded to two tungsten cations, decreasing the electron density on the bridging oxygen and resulting in weak Coulombic interactions with the hydroxyl hydrogen. As far as the terminal oxygen is concerned, its large distance from the Lewis acid adsorption site may present a prohibitively large barrier to dissociation. The tungsten-tungsten spacing is around 3.7 Å, which can be compared qualitatively to the maximum oxygen-oxygen distance for effective hydrogen bonding of 3.5 Å.[131,132]

By contrast, the UPS data clearly shows that on the reduced surface the large majority of methanol adsorbs dissociatively. If the W 4f XPS spectra are interpreted within the final state model to imply that only $W^{5+}$ sites exist on the (1x1) surface, as proposed by Jones, *et al.*,[133] then the higher electron density in the surface (as revealed by a larger intensity in the gap in UPS measurements [50]) suggests an increase in the basicity of the bridging oxygens, relative to the oxidized surface. Theoretical calculations regarding the electronic structure of the reduced surface are needed to fully understand the dissociation mechanism.

While we prefer the final state interpretation of the W 4f XPS region to the initial state model (see below), we are not aware of independent evidence to exclude the presence of lower oxidation state species, and in particular metallic tungsten species. The presence of metallic tungsten could also account for the dissociative adsorption of methanol on the reduced surface. However, the decomposition of methanol on tungsten, and other metal surfaces, results in production of $H_2$ and CO.[134,135] During CTDS experiments, we did not detect any $H_2$, CO or $CO_2$ desorption. Nevertheless, we cannot completely exclude the possibility of small metallic tungsten clusters, since the behavior of cluster may differ significantly from the reactivity of a metal surface.

### 3.4.2. The roles of diffusion and surface heterogeneity

The experimental data of Figure 3.4 cannot be explained by intermolecular interactions on a homogeneous surface, either with or without rapid diffusion. Repulsive interactions lead to peak splitting, and attractive interactions shift the peak to higher temperature with increasing coverage. Qualitatively, the heterogeneous surface model,

shown in Figure 3.6B, is consistent with the coverage dependence of the spectra on the oxidized surface (Figure 3.4B), and the overlap of the high temperature side of the peaks indicates that diffusion is rapid compared to desorption. Further refinement of the lattice site adsorption energy distribution could be performed to more closely fit the experimental data, as done by Nelson *et al.*;[103] however, the results would not provide fundamental information in our case without more extensive characterization of the surface structure and morphology.

The origin of the surface heterogeneity, necessary to explain the coverage dependent spectra, is most likely associated with the surface structure of the epitaxial films. Experimentally, it was found that the $WO_3(001)$ surface is characterized by stepped structures.[67] Sputtering preferentially removes oxygen and generates oxygen vacancy defects, as revealed by the XPS spectra. Nevertheless, similar desorption behavior was observed in the desorption of $H_2O$ from a hydroxylated $\alpha$-$Al_2O_3(0001)$ surface by Nelson *et al*,[103] in which the single crystal surface was known to be nearly defect free prior to desorption. The independence of the peak shape and position with increasing dose suggest that mobility is poor. Thus, the heterogeneity in the surface seems to arise during the dehydroxylation process, not from the initial surface defect structure.

The simulation results imply that neither repulsive nor attractive interactions, and in particular hydrogen bonding, contribute significantly to the coverage and temperature dependence of methanol desorption from the reduced and oxidized surfaces. While this seems surprising, formation of an effective hydrogen bond requires an oxygen-oxygen distance less than 3.5 Å.[131,132] For the adsorption of methanol on $WO_3$ surfaces, with

molecular adsorption at tungsten cation (Lewis acid) sites, the tungsten-tungsten spacing of approximately 3.7 Å [53] is not very favorable for hydrogen bond formation. Furthermore, molecular dynamics studies of hydrogen bonding in crystalline and liquid phase methanol suggest that hydrogen bonding can occur only with two nearest neighbors, forming either 1-dimensional chains or cyclic chains, which further reduces the possible role of hydrogen bonding [136-138] on the desorption energetics.

The UPS spectra showed that the methanol adsorbed molecularly on the oxidized surface and dissociatively on the reduced surface. However, the coverage dependent desorption spectra for methanol on both surfaces are qualitatively very similar, as shown in Figure 3.4. The main difference is that desorption occurs at higher temperatures on the reduced surface. This implies that desorption from the reduced surface is essentially a pseudo-first order process. The reasons for this are not easily justified. Such behavior is found for desorption of $H_2$ from the dissociatively adsorbed hydride state on the Si(100) dimers.[139] The first-order behavior in the silicon hydride case is thought to be due to the poor mobility of the hydride species and that the close proximity of the two hydrides leads to a concerted desorption process. Although the simulation shows clearly that diffusion of *methanol* on the *oxidized* surface is relatively fast compared to desorption, this does not necessarily imply that the *methoxy* species is mobile on the *reduced* surface. As discussed above, the dissociation of methanol probably requires a local acid/base pair site configuration favorable for dissociation of the hydroxyl group. A highly mobile methanol precursor state could then dissociate at a strong Brønsted base site, which retains the proton in close proximity to a more strongly bound methoxy group. The assumption that a stronger Lewis acid/Brønsted base site pair is required for dissociation

of methanol is supported by the higher desorption temperature of methanol on the reduced surface. Thus, the methoxy can desorb in a pseudo-first order process as methanol by combining with the neighboring proton.

### 3.4.3. Reaction mechanism on the reduced surface

During the CTDS experiments, both on the reduced and oxidized $WO_3(001)$ surfaces, methanol is the only desorption product detected. By comparison, methanol was found to react on the sputtered and annealed $TiO_2(001)$ surface to form dimethyl ether.[35] Adsorbate surface mobility and the adsorption structure were thought to be the key factors in facilitating the surface coupling reaction. Kim and Barteau [35] proposed that the doubly coordinatively unsaturated site is the active center responsible for dimethyl ether formation on $TiO_2(001)$ single crystal surfaces, resulting in the close proximity of two adsorbed methoxy groups. This argument was based on the fact that dimethyl ether was detected only on {114}-facetted surface, which was characterized by the stepped structure containing 4-fold oxygen coordination sites, and not on the {011}-facetted surface, which is characterized by a 5-fold oxygen coordination structure. If the reduced surface is characterized by a (1×1) structure with most of the terminal oxygens removed, the large tungsten-tungsten distance would not favor the coupling reaction. However, interpretation of the coverage dependent desorption spectra suggests that adsorbate mobility is not the limiting factor for dimethyl ether production.

A closer tungsten-tungsten distance can, however, be achieved at shear plane structures. During sputtering and annealing, removal of lattice oxygen can also lead to the conversion of corner sharing octahedra into edge sharing structures as found in the

bulk at crystallographic shear (CS) planes.[64] Experimentally, the formation of the CS plane was a facile route for oxidation of the allyl group to acrolein on reduced $WO_3$ surfaces.[140] While we find that decomposition of dimethyl methyl phosphonate (DMMP) on the reduced surface produces dimethyl ether, the fact that dimethyl ether was not observed in this study, from the dissociatively adsorbed methoxy groups, eliminates the possible role of these sites for a surface mediated coupling reaction.

### 3.4.4. Interpretation of XPS data

The W 4f region of the XPS spectra of Figure 3.2 could be interpreted in at least three different ways. The initial state model, involving $W^{6+}$, $W^{5+}$, $W^{4+}$, and $W^0$ species could be justified on the basis of apparent binding energies in reference compounds. The presence of $W^{6+}$ species is easily understood in terms of fully, octahedrally coordinated cations, while the $W^{5+}$ sites could be ascribed either to the cations in the c(2x2) structure with missing terminal oxygens or to cations along idealized shear plane structures. The assignment of $W^{4+}$ species is less clear, but could be attributed either to cations along shear planes that are missing terminal oxygens, or to regions of $WO_2$. The reduction of $WO_3$ to $WO_2$ is thought to be unlikely under vacuum reduction conditions, according to X-ray diffraction experiments.[65] However, we are not aware of any other independent evidence for formation of $W^0$ under the conditions of the experiment, and the reactivity toward methanol, as noted above, is not typical of tungsten metal.

The interpretation of the spectra in terms of final state screening effects, consistent with that of Dixon, *et al.*,[50] is in good agreement with other information we have regarding the properties of our epitaxial films. First, comparing the splitting

between the screened and unscreened final state levels to the empirical data given by Chazalviel, *et al.*,[116] for a range of sodium bronzes, the substoichiometry, $x$, in our $WO_{3-x}$ films would be approximately 0.05. Second, the relative intensity in the gap to that in the valence band region, again according to a theoretical relation given by Chazalviel, *et al.*,[116] predicts a sub-stoichiometry of a few percent. Third, the ratio, $\beta$, of the intensity of the unscreened final state feature to that of the screened final state, was found empirically to behave as $\beta = 0.75x^{-1/3}$, by Chazalviel, *et al.*,[116] which predicts ratios between 2 and 3.5 for x = 0.05 and 0.01, respectively, which is consistent with the fits shown in Figure 3.2. Measurements of the optical absorbance of our epitaxial films in the UV-vis region and estimates of the carrier concentration and mobility give values for the substoichiometry in the range of 0.01 to 0.05, depending upon growth and operating conditions of the films in sensor applications.[32,66] Thus, the presence of a screened final state for the reduced surface seems to be consistent with the carrier density in these materials.

On general grounds, Occam's Razor would suggest that if the data can be fit with fewer doublets, the simpler model should be chosen (*i.e.* fewer doublets are required in the final state model). However, we would like to point out that the interpretation of Dixon, *et al.* [50] implies spatial localization of the narrow bands. In the case of sodium bronze, only one (formally $W^{6+}$) initial state was considered, and the presence of two features originated from the screened or unscreened final states. If the electrons produced from reduction of $WO_3$ form a narrow band that is delocalized, similarly to the sodium bronze, then there should be *four* doublets in the W 4f region, two originating from each initial state (formally $W^{6+}$ and $W^{5+}$). If the $W^{6+}$ initial states results only in one,

unscreened final state, then the implication is that the narrow band must be spatially localized to regions, such as the high tunneling probability "bright rafts", in which there are (formally) $W^{5+}$ sites. Further systematic work, particularly on well characterized surfaces in which the electron density can be estimated, *e.g.* from the plasmon frequency with HREELS, is required to resolve this issue.

Many body effects have also been discussed in terms of the charge transfer model, which involves electron transfer from a ligand atom to the transition metal ion.[141-143] The effect is typically found in the late transition metal dihalides and oxides, such as $NiCl_2$ and CuO.[144-146] However, satellite peaks are typically on the high binding energy side, which is not consistent with our W4f XPS spectra.

# REACTIONS OF ALIPHATIC ALCOHOLS ON $WO_3$(001) SURFACES

## 4.1. Introduction

Understanding the surface reactivity of the $WO_3$ surface is of fundamental importance in exploring its potential applications. Tungsten oxide has been extensively studied as a catalyst in different forms. Oxide supported $WO_3$ in the sub-monolayer uptake regime exhibits high catalytic activities for the metathesis reaction, olefin isomerization, and disproportionation reactions.[147-151] It has been used as the sensing element in detection of nitric oxides[24,27,70] and $H_2S$.[15,26,69] The properties of the crystalline $WO_3$ have been studied in detail, including its semiconductivity and production of oxygen vacancies and crystallographic shear (CS) planes.[64,106,107,109,133,152,153] However, a detailed understanding of how the rate limiting steps in specific surface reactions control the conductivity is not yet fully understood. In our laboratory, high quality $WO_3$ thin films have been fabricated,[66,67] and much effort has been focused on development of selective $WO_3$ thin film-based NO and organophosphorous compound sensors.[33,71]

In Chapter 3, we have reported studies of the adsorption and desorption of methanol on $WO_3$ surfaces. Measurements were made on an oxidized surface and a reduced surface, characterized by XPS and UPS, in order to probe the structure dependence of the surface activity.[154] Comparison of our XPS and UPS data with the single crystal $WO_3$(001) study by Dixon, *et al.* using XPS, UPS and STM suggested that our oxidized surface was associated with the c(2×2) structure with line defects while the reduced surface was similar to the (1×1) structure with most of the surface terminal oxygens removed.[50,154] Our UPS measurements showed that methanol is molecularly

adsorbed on the oxidized surface and dissociatively adsorbed on the reduced surface. The shape of the coverage-dependent desorption curves was modeled with Monte Carlo simulations, which are interpreted in terms of surface heterogeneity and facile surface diffusion. Reaction products, such as formaldehyde and dimethyl ether, which are produced on defective $TiO_2(001)$ surfaces,[35] were not detected.

We also studied the surface activity and reaction selectivity in the decomposition of DMMP on both surfaces.[111] The study showed that DMMP decomposes on both surfaces through production of methoxy intermediates. However, these two surfaces show different reaction selectivity during decomposition of DMMP. Methanol and dimethyl ether were produced on the oxidized surface, but only dimethyl ether was observed on the reduced surface. Thus, in both the DMMP and methanol studies, the reduced and oxidized $WO_3$ surfaces behave differently.

The surface activity is closely related to the surface structure. In $WO_3$, a crystalline network is formed from W-O-W chains in 3-dimensions, which can be described by corner sharing octahedra. In comparison with the edge sharing octahedral structures, for instance in $TiO_2$, or face sharing octahedral crystal structures, the corner sharing octahedral structure results in a large spacing between metal cations. This leads to a large ($\approx$3.7Å) separation between the Lewis base sites (the terminal oxygens) and Lewis acid sites (the coordinatively unsaturated tungsten cations), on the $WO_3(001)$ surface. The large spacing may be responsible for the inactivity toward dissociative adsorption of water and methanol on the oxidized $WO_3(001)$ surface since, although the c(2×2) surface contains acid/base pairs required for dissociative adsorption, the spatial

separation between the acid/base sites also contributes to the activation energy barrier for extraction of the hydroxyl hydrogen.[154]

In this work we studied the reactions of ethanol and isopropanol on these two different $WO_3$ surfaces to further probe the surface activity and structure dependence of surface reactions. A study by Tanner, *et al.*[47] showed that the oxidized single crystal $WO_3(001)$ surface only has activity toward dehydration of alcohols to form alkenes. In their study, 1-propanol, isopropanol and tert-butyl alcohol were exposed to the surface. The corresponding dehydration product alkene desorbs at high temperature after desorption of alcohols are almost complete at low temperatures. It has been pointed out that the coverage of alkoxy species remaining after desorption of alcohols is complete is determined by the competition between associative desorption of alcohols and hydroxyls as water.[83,155] Gamble, *et al.*[155] proposed a defect controlled model to explain the coverage of alkoxy species remaining on the surface at high temperature for ethanol on the $TiO_2(110)$ surface. In comparison, STM [47] identified adsorption of alkoxy species on the majority $WO_3(001)$ terrace sites after the surface was annealed to temperatures where alcohol desorption is complete with no particular evidence for specific defect sites in controlling the selectivity toward the alkene. Thus, the CTDS data that we present here provides complementary information to distinguish the role of defects from that of diffusion and the competition associative desorption of alcohols and recombination of hydroxyls to form water in determining the coverage of alkoxy species that react to form alkene.

This study shows that the desorption of water and alcohols is shifted to higher temperature on the reduced $WO_3(001)$ surface than on the oxidized surface. The shape of the coverage dependent desorption spectra indicates the importance of surface heterogeneity and relatively rapid diffusion of molecularly adsorbed alcohol, consistent with our previous observations for methanol on these two surfaces. During the CTDS experiments, removal of alcohols on the surface occurred through two channels: desorption of alcohol at lower temperatures and dehydration to alkene, which desorbed at higher temperature. The coverage dependence of the selectivity toward the alkene indicates that the alkoxy coverage remaining after dehydroxylation is controlled by the competition between surface reaction kinetics under the low coverage conditions of our experiments. We attribute the rate-limiting step to C-O bond scission in the case of ethanol dehydration reaction. Our data are not able to distinguish whether the β-H elimination or C-O bond scission is the rate-limiting step for isopropanol dehydration; however, the comparison of n-propanol with isopropanol in the study by Tanner, *et al.*[47] indicates that C-O bond scission is again the rate-limiting step.

## 4.2. Results

### 4.2.1. Ethanol interaction with the reduced $WO_3(001)$ surface

A set of coverage dependent desorption spectra are shown in Figure 4.1. As the surface coverage decreased, the desorption temperature increased indicating that, on the basis of our Monte Carlo simulations [154], diffusion is sufficiently rapid to migrate to, and desorb from the most stable adsorption sites. For a coverage of 0.012 ML, ethanol desorption was observed at 432 K on the reduced $WO_3$ surface. Adsorption of the first

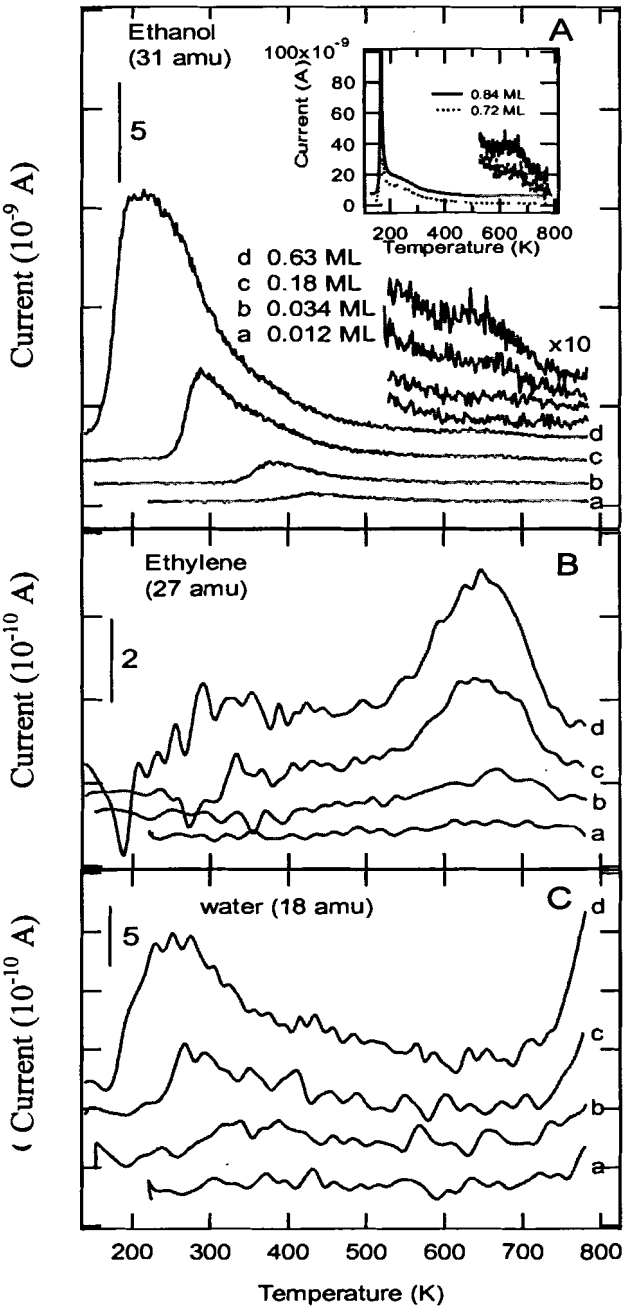


**Figure 4.1.** Ethanol reactions on the reduced $WO_3(001)$ surface. A) Ethanol molecular desorption spectra presented as mass 31 for different coverages. The high temperature portion of the desorption spectra were expanded as indicated. B) The corresponding ethylene desorption spectra, shown as mass 27, which coincided with the high temperature ethanol desorption peak. Spectra were obtained by removing the contribution from ethanol (see text for details). C) The corresponding water desorption spectra. Peaks were offset for clarity.

layer saturated at acoverage slightly greater than 0.63 ML and a multilayer desorption peak appeared at 165 K for a coverage of 0.72 ML. The characteristics of the overlapping leading edge and the increase of the peak temperature with coverage are consistent with zeroth order desorption kinetics for multilayer desorption, with a desorption energy of 47 kJ/mol. At an ethanol surface coverage greater than 0.18 ML, an additional high temperature desorption peak, as shown by the expanded spectra in Figure 4.1A, emerged at 650 K, which coincides with ethylene desorption, as shown in Figure 4.1B (described below).

During the ethanol CTDS experiment, ethylene, produced by ethanol dehydration, was detected around 650 K on the reduced surface. Since masses 26, 27 and 28, which are the major fragments of ethylene, are also fragments of ethanol, the desorption of ethylene is superimposed on the ethanol desorption spectrum and can not be distinguished from ethanol desorption directly. However, the ethylene fragmentation pattern does not contain mass 31, which is the strongest ion in the ethanol fragmentation pattern; hence, the ethanol contribution to masses 26, 27 and 28 was removed from these spectra by scaling the mass 31 desorption trace based on the fragmentation pattern of ethanol. The contribution of ethylene to the 27 amu desorption spectra are shown in Figure 4.1B. Note that ethylene production increases with the surface coverage of ethanol and that the desorption temperatures are constant.

The corresponding water desorption spectra (mass 18) are presented in Figure 4.1C. As the ethanol coverage increased to 0.034 ML, water desorption was observed at 350 K and the desorption temperature decreased with increasing ethanol coverage. The low temperature water peaks are similar to spectra shown in Figure 4.5 (see section 3.5)

for adsorption of water. Very weak water desorption was detected above 700 K, which increased in intensity with the ethanol coverage.

### 4.2.2. Ethanol interaction with the oxidized $WO_3$(001) surface

The ethanol CTDS data for the oxidized $WO_3$ surface are presented in Figure 4.2 in a manner similar to Figure 4.1 with the contributions due to ethanol, ethylene, and water in parts A, B, and C, respectively. As the surface coverage decreases, again the desorption temperature increases. Ethanol desorbs at 418 K for a surface coverage of 0.0024 ML. By comparison with the spectra of Figure 4.1A, the desorption temperature on the oxidized surface is lower than on the reduced surface at the same coverage, and the peak shape is skewed to lower temperature. Based on our Monte Carlo simulations of methanol, these spectra suggest a distribution of adsorption site energies that is substantially reduced at higher adsorption energy. At coverages greater than 0.02 ML, an ethanol desorption peak is observed above 600 K, which overlaps with the ethylene desorption peaks shown in Figure 4.2B, similarly to the case of the reduced surface. The intensity of the desorption peak increases with ethanol surface coverage, as shown by the expanded spectra in Figure 4.2A.

Ethylene desorption was detected near 650 K for a surface coverage greater than 0.0024 ML. Similarly to the reduced $WO_3$ surface, the ethylene desorption peaks do not shift with coverage. The corresponding water desorption spectra are shown in Figure 4.2C. For an ethanol coverage of 0.0024 ML, water desorption was detected at 295 K. The desorption temperature decreases with increasing surface coverage, similarly to the low temperature water desorption profiles on the oxidized surface, discussed in Sect. 3.5.

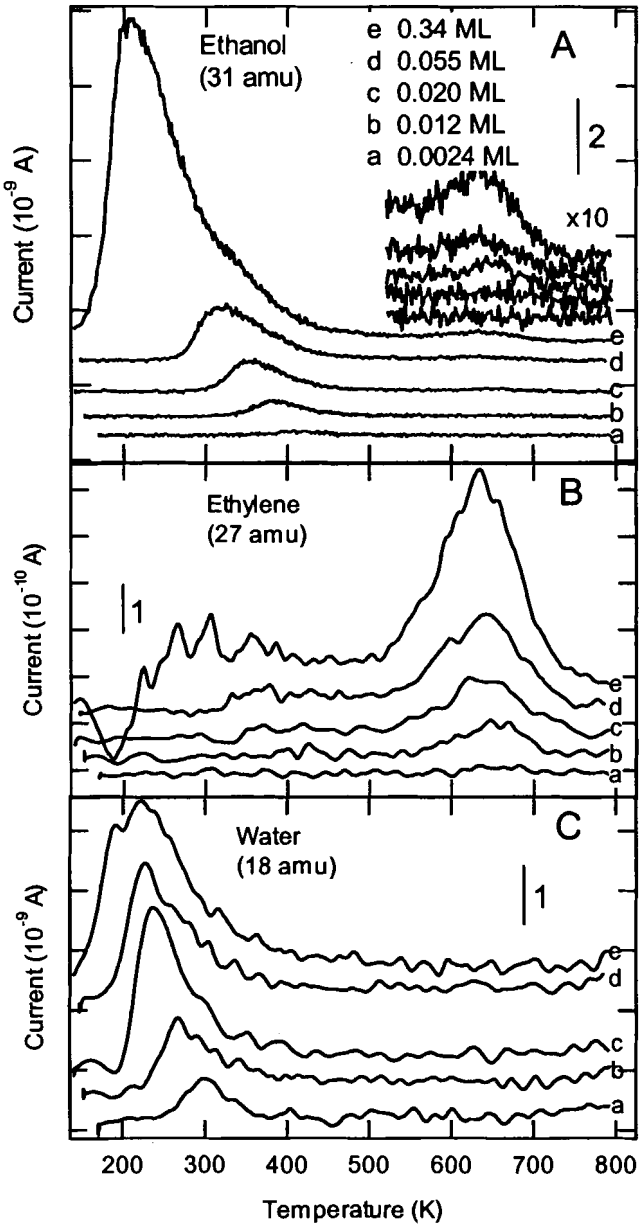


**Figure 4.2.** Ethanol reactions on the oxidized $WO_3(001)$ surface. A) Ethanol molecular desorption spectra presented as mass 31 for different coverages. B) The corresponding ethylene desorption spectra (mass 27), and C) water desorption spectra presented as in Figure 4.1. Peaks were offset for clarity.

However, compared to the ethanol reaction on the reduced surface (Figure 4.1C), desorption of water above 700 K was dramatically reduced.

### 4.2.3. Isopropanol interaction with the reduced $WO_3(001)$ surface

During isopropanol CTDS experiments, desorption of isopropanol, propylene and water were observed, which is shown in Figure 4.3A, B and C respectively. The isopropanol and propylene desorption overlap around 500 K, as shown in Figure 4.3A and 3B. Propylene has major fragments at masses 39, 41 and 42, which are also cracking fragments of isopropanol, but does not have the mass 45 fragment, which is the dominant fragment of isopropanol. Therefore, the propylene desorption spectrum, shown in Figure 4.3B, was obtained by subtraction of the isopropanol contribution to mass 41 by scaling the mass 45 trace according to the isopropanol fragmentation pattern. Isopropanol desorption appeared at 530 K for a surface coverage of 0.00045 ML; the desorption temperature decreased as the surface coverage increased. The coverage dependent behavior again suggests that isopropanol diffusion is sufficiently fast that the isopropanol molecules find the stronger binding sites.[154] Multilayer desorption was detected at 175 K, as shown in the inset of Figure 4.3A, with characteristic zeroth order desorption and a desorption energy of 27 kJ/mol. In comparison with ethanol CTDS, the isopropanol molecular desorption peak occurs approximately 100 K higher, but no high temperature, recombinative desorption peak was detected. The higher desorption temperature for isopropanol with respect to ethanol is consistent with the higher molecular weight. At a total coverage less than 0.00045 ML, isopropanol desorption was not detected, but propylene was still observed at 527 K. The production of propylene increases with the

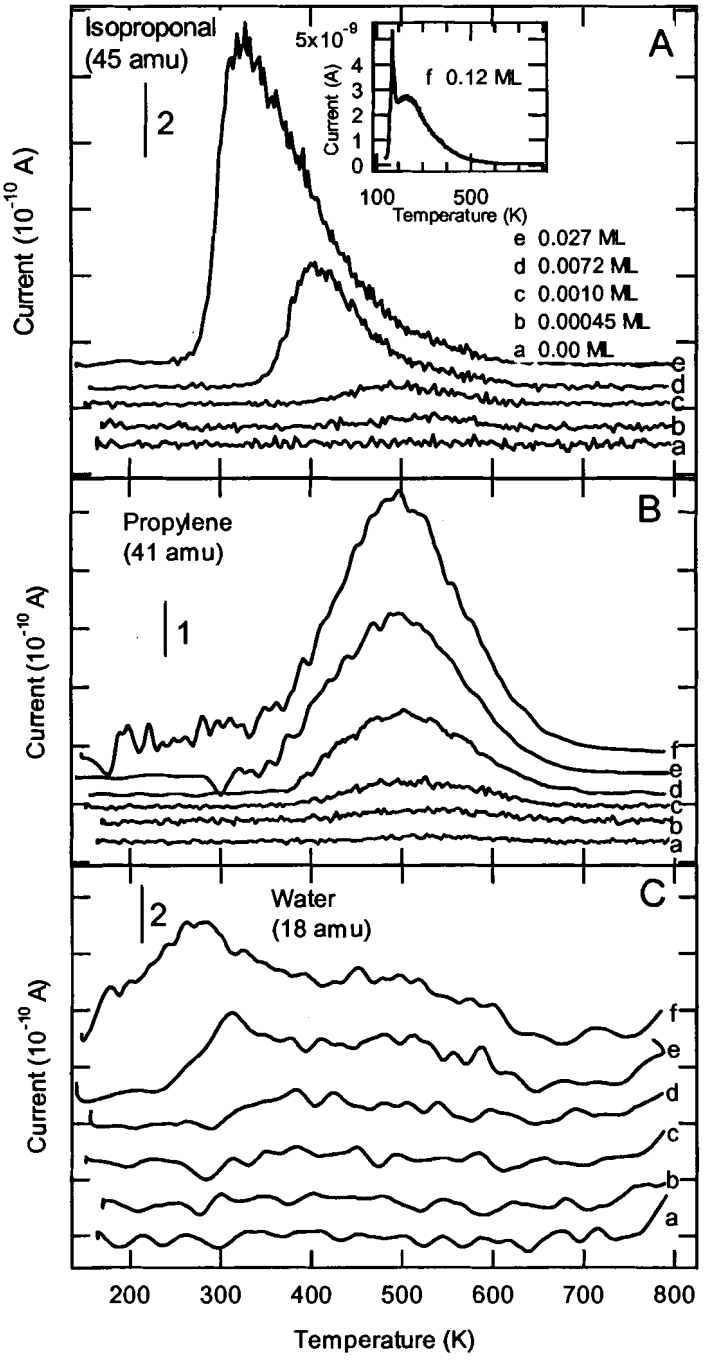


**Figure 4.3.** Isopropanol reactions on the reduced $WO_3(001)$ surface. A) Isopropanol molecular desorption spectra presented as mass 45 for different coverages, with the multilayer desorption of isopropanol presented in the inset. B) The corresponding propylene desorption spectra (mass 41), obtained by removing the contribution from isopropanol (see text for details), and C) water desorption spectra with two desorption peaks resolved at high isopropanol coverages. Peaks were offset for clarity.

isopropanol surface coverage, with a peak position independent of coverage, but at a substantially lower temperature than the ethylene peak at 650 K observed for ethanol dehydration.

A broad water desorption peak was observed around 400 K as the surface isopropanol coverage increased to 0.0072 ML, below which propylene was already detected. This water desorption profile evolved into two desorption peaks centered at 317 K and 508 K, respectively, for an isopropanol coverage of 0.027 ML (Figure 4.3C). The peak temperature for the low temperature desorption decreased with increasing surface coverage, similar to the behavior following water adsorption on the reduced surface (Sect. 3.5). Note that the broad higher temperature desorption, shown in curves e and f in Figure 4.3C, overlaps with the desorption of propylene and that the peak position is relatively coverage independent. The water desorption above 700 K, which was detected for ethanol on the reduced surface, was suppressed.

### 4.2.4. Isopropanol interaction with the oxidized $WO_3$(001) surface

The isopropanol dehydration reaction also occurred on the oxidized $WO_3$ surface. Figure 4.4 shows the desorption spectra for isopropanol, and the corresponding propylene and water desorption spectra. The propylene desorption spectra, shown in Figure 4.4B, were obtained by subtraction of the isopropanol contribution as described for the reduced surface. Again, the isopropanol spectra overlapped with propylene desorption above 400 K.

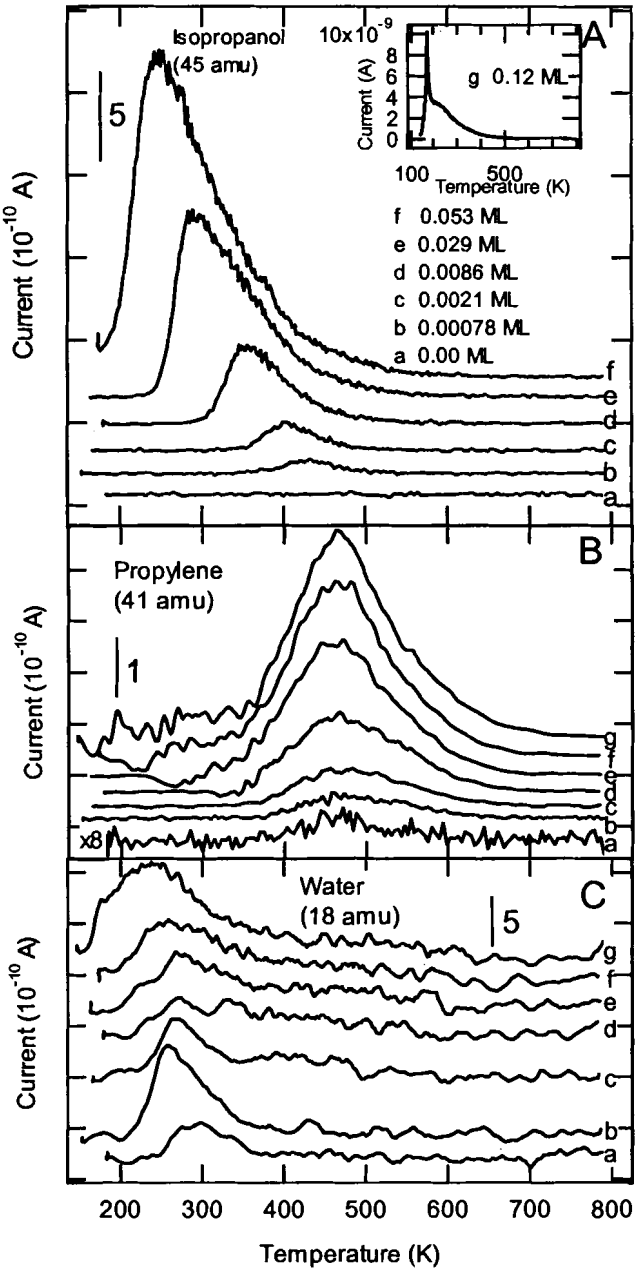


**Figure 4.4.** Isopropanol reactions on the oxidized $WO_3(001)$ surface. A) Isopropanol molecular desorption spectra presented as mass 45 for different coverages. B) The corresponding propylene desorption spectra (mass 41), and C) water desorption spectra as described in Figure 4.3. Peaks were offset for clarity.

At an isopropanol coverage of 0.00078 ML, isopropanol desorption was observed at 433 K, which was about 100 K lower than on the reduced surface. The desorption temperature increased with decreasing surface coverage, which implies that isopropanol diffusion is relatively rapid compared to desorption.[154] Similarly to the reduced $WO_3$ surface, only one isopropanol desorption peak was observed. For a surface coverage less than 0.00078 ML, isopropanol desorption was not observed; however, very weak propylene desorption was detected at 467 K shown in Figure 4.4B curve a. The production of propylene increased with isopropanol surface coverage, but the desorption temperature did not change. By contrast to the ethanol results, the desorption temperature of the dehydration product was significantly lower on the oxidized surface than on the reduced surface. A multilayer desorption peak at 175 K appeared at a coverage of 0.12 ML, as shown in the inset of Figure 4.4A. The desorption energy of 27.4 kJ/mol is essentially identical to the multilayer desorption energy on the reduced surface.

The water desorption spectra exhibited different features on the oxidized surface than on the reduced surface. At a coverage less than 0.00078 ML, water desorption was detected at 298 K, which was observed on the reduced surface only at high isopropanol coverage; the desorption temperature for this desorption state decreased as the surface coverage increased as expected for molecular adsorption (see Sect. 3.5). As the isopropanol surface coverage increased to 0.0021 ML, a very weak desorption peak appeared around 405 K. As the surface coverage increased, this desorption peak broadened (Figure 4.4C curves d to g), and overlapped with the desorption of propylene. On the oxidized $WO_3$ surface, water desorption due to background adsorption was found

below 350 K during our CTDS experiments. Therefore, the water desorption below 350 K includes the contribution from condensation of background water vapor, which was introduced into the chamber during oxidation of the $WO_3$ surface.

During the ethanol and isopropanol CTDS experiments, the dehydrogenation reaction products, such as acetaldehyde and acetone, were not detected, showing that the $WO_3$ thin film surface exhibits only dehydration activity.

### 4.2.5. Water adsorption and desorption on $WO_3$(001) surfaces

Water adsorption and desorption was conducted in this study in order to understand the surface dehydration reaction of ethanol and isopropanol on the $WO_3$ surfaces. Water desorption spectra are displayed in Figure 4.5A for desorption on the reduced $WO_3$ surface and Figure 4.5B for desorption on the oxidized $WO_3$ surface. The peak desorption temperature decreased as the surface coverage increased on both surfaces. On the reduced surface the desorption temperature is higher than on the oxidized surface.

### 4.2.6. Relative yield of dehydration product on $WO_3$(001) surfaces

Figure 4.6 shows the yield of ethylene and propylene evolved from the dehydration reaction of ethanol and isopropanol, respectively, on the reduced and oxidized $WO_3$ surfaces. The plot is simply the ratio of the integrated ion currents for ethylene and propylene without correcting for their respective calibration factors. Actually, the ratio of the relative ionization probabilities for alcohols to those for their corresponding alkenes are approximately 1.5.[156-158] Therefore, correcting the area ratios

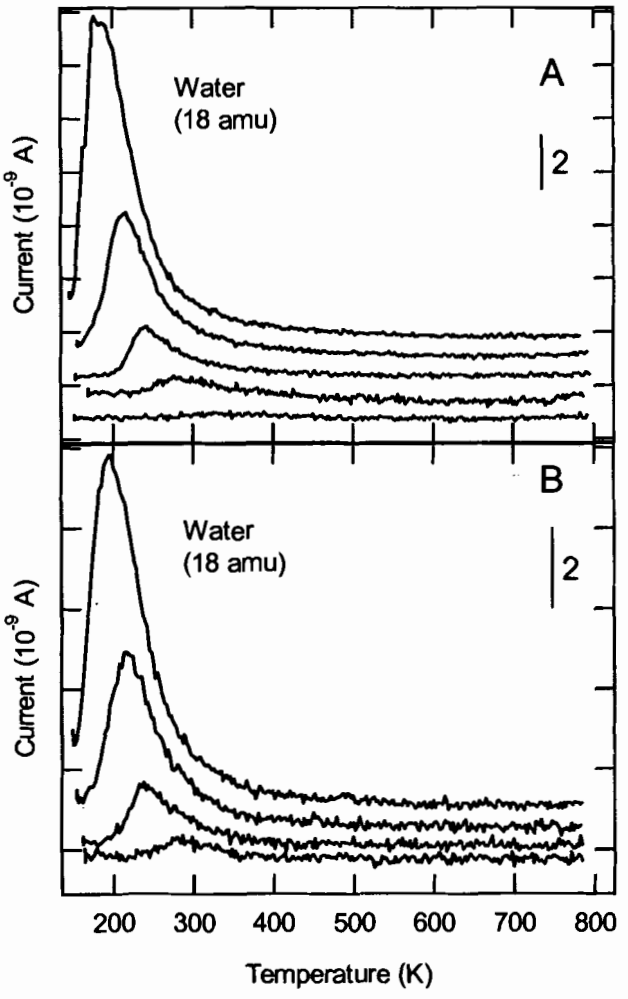


**Figure 4.5**. Water thermal desorption spectra at different coverages on $WO_3(001)$ surfaces. A) On the reduced $WO_3(001)$ surfaces and B) on the oxidized $WO_3(001)$ surface. The conditions for producing these surfaces and measuring the thermal desorption spectra were similar to those used in the alcohol experiments.

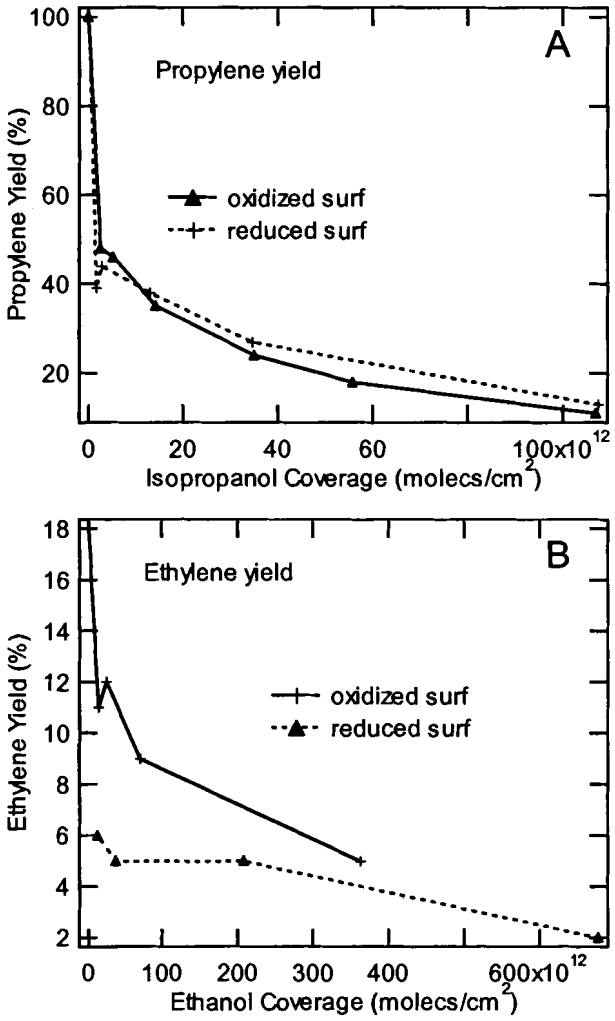


**Figure 4.6**. Comparison of the yield of alkene dehydration products on $WO_3(001)$ surfaces. A) propylene and B) ethylene on the oxidized and the reduced $WO_3$ surfaces, plotted as the ratio of integrated ion current vs. alcohol coverage. (see text for details.)

will not qualitatively change the plot. As shown in Figure 4.6, the yields of ethylene and propylene are not significantly different for the oxidized vs. the reduced $WO_3(001)$ surfaces, showing the insensitivity of dehydration of alcohols to the surface structure.

### 4.3. Discussion

We first examine the mechanism of the dehydration reaction and identify the rate limiting step as CO bond scission. We assume that the dehydration product evolves from alkoxy species remaining on the surface after the low temperature desorption of the alcohol is complete, and therefore the alkoxy coverage determines the selectivity toward the alkene. We then consider two models to understand how the selectivity, i.e. the ratio of the alkene to alcohol, is controlled in the thermal desorption process.

#### 4.3.1. Mechanism of dehydration reactions

On both the oxidized and the reduced $WO_3$ surfaces, the ethylene desorption temperature, detected above 600 K (Figures 4.1B and 4.2B), is higher than the propylene desorption temperature, observed between 450 and 500 K (Figures 4.3B and 4.4B). Our observations are consistent with the observations for alcohol dehydration reactions on the $TiO_2(001)$ surface by Kim and Barteau[84]. In both cases, the larger alkene desorbs at lower temperature, suggesting that desorption of the dehydration products is a reaction limited, rather than desorption limited, process. The coverage independence of the desorption temperatures for ethylene and propylene on the heterogeneous $WO_3$ surfaces also supports this conclusion. The study by Tanner, *et al*,[47] of the dehydration reactions

of 1-propanol and isopropanol on the single crystal $WO_3(001)$ surface showed that propylene is produced at a lower temperature from isopropanol than from 1-propanol.

Dehydration of the alkoxy species requires cleavage of either the α or β-CH bond, and CO bond scission. We now consider whether or not each of these is the rate limiting step. Generally, the α–H bond is more acidic than the β–H, because the former C-H bond is more polarized by the oxygen atom. Several studies have shown that α-H abstraction results in formation of aldehydes or ketones for alcohols on oxide surfaces.[83,84,94,96,159,160] However, acetaldehyde and acetone were not detected during our experiments for ethanol and isopropanol on the $WO_3$ surfaces, respectively. Using isotope labeling techniques, Gamble, *et al* [155] have shown clearly that, for ethoxy species on the $TiO_2(110)$ surface, α-H abstraction and subsequent H migration during the dehydration reaction can be ruled out. Therefore, α-H abstraction of the alcohols on the $WO_3$ surfaces seems unlikely.

If abstraction of the β hydrogen is the rate limiting step, ethylene and propylene would be formed at similar temperatures, since the energy barriers for breaking the β–CH bonds in ethanol and in isopropanol should be similar due to the similarity in their local chemical structures and adsorption configurations on the surfaces. In this case, for a reaction limited surface process, desorption of ethylene and propylene should occur at similar temperatures, which contradicts our observations.

We conclude that cleavage of the C-O bond is most likely the rate limiting step for the dehydration reaction of ethanol, but not necessarily isopropanol, on the $WO_3(001)$ surfaces. This can be justified on the basis that the stability of the carbocation intermediate, produced by breaking the C-O bond, decreases in the order tertiary >

secondary > primary, as suggested by Tanner, *et al.* [47] for their comparison of n-propanol, isopropanol and tert-butyl alcohol dehydration. To the extent that the energy barrier height decreases with increasing stability of the carbocation formed, C-O bond scission in isopropanol should occur at a lower temperature than in ethanol, and produce propylene at a lower temperature than ethylene. This trend is consistent with our data as well as that of Tanner, *et al.* [47] and of Kim and Barteau.[84]

Gamble, *et al.* [155] identify β–hydrogen elimination from one ethoxy species on the $TiO_2$(110) as the rate limiting step which produces the proton for associative desorption of coadsorbed ethoxy species to produce ethanol. However, they suggest that the delay in the ethylene desorption peak, relative to the ethanol peak, is due to a somewhat higher barrier for cleavage of the C-O bond in the $–OCH_2CH_2–$ species. A similar, though small, temperature shift between the ethanol and ethylene peaks can also be observed in our experiments on the $WO_3$ surfaces in Figures 4.1 and 4.2. This implies that *breaking the C-O bond is the rate limiting step for ethylene production.*

Figures 4.3 and 4.4 show that propylene desorption is accompanied with water desorption. This water desorption is higher than that found in water adsorption experiments and is clearly resolved from the low temperature desorption peak, assigned to recombination of surface hydroxyls formed during dissociative adsorption of isopropanol. We attribute it to the recombination of surface hydroxyls resulting from abstraction of the β hydrogen from isopropoxy on the surfaces. However, because of the similarity in the desorption temperatures for water and propylene, the barriers to C-O bond scission and β–hydrogen elimination may be similar.

### 4.3.2. Selectivity toward alkene production

Our experiments show that two channels are available for removal of adsorbed ethanol and isopropanol: desorption as alcohol molecules and desorption as alkenes via dehydration reactions. We present two limiting cases that potentially control the selectivity of alcohol desorption vs. dehydration to the alkene. The first is based upon recent work on other oxide single crystal surfaces in which the yield of alkene is determined by particular surface defect sites; the second is based upon the role of diffusion rates and reaction kinetics, without necessarily requiring "special" defect sites. We then discuss the experimental evidence and conclude that, under the low coverage conditions of our experiments, the second model controls the selectivity to alkenes.

In either case, the adsorption of the alcohol may be (1) associative, (2) dissociative, or a mixture of alcohol and alkoxy species may be present,

$$ROH(g) \rightarrow ROH(a) \tag{1}$$

$$ROH(g) \rightarrow RO(a) + H\cdots O(l) \tag{2}$$

where the alcohol and alkoxy species may be adsorbed on Lewis acid sites or other defect sites and the proton adsorbs on a lattice oxygen. Desorption of alcohol may occur via the reverse reactions:

$$ROH(a) \rightarrow ROH(g) \tag{3}$$

$$RO(a) + H\cdots O(l) \xrightarrow{k_4} ROH(g) \tag{4}$$

Surface hydroxyls may also be lost by recombinative desorption to form water and oxygen surface vacancies:

$$H\cdots O(l) + H\cdots O(l) \xrightarrow{k_5} H_2O(g) + V_O^{\bullet\bullet} + O(l) \tag{5}$$

After desorption of alcohol at the lower temperatures, by reactions 3 and 4, and loss of surface hydroxyls, via reaction 5, there is some fraction of the dissociatively adsorbed alcohol that remains as alkoxy species. These intermediates are not able to desorb as alcohol and are trapped on the surface until either CO bond scission occurs, or a proton becomes available, for example from β–hydrogen elimination from a co-adsorbed alkoxy species. We now consider two models that could control the coverage of alkoxy species remaining after the low temperature desorption is complete, since these are the species that ultimately lead to alkene production.

#### 4.3.2.1. Defect control of selectivity

Gamble, *et al.*[155] proposed that the sites responsible for the ethanol dehydration reaction on the $TiO_2(110)$ surface are the bridging oxygen vacancies produced during water desorption. These vacancies, corresponding to those produced in reaction 5, bind the ethoxy intermediate much more strongly than ethoxy species adsorbed on 5-fold $Ti^{4+}$ sites, as demonstrated by their unreactivity toward further hydroxyl exposure.[155] The surface hydroxyls are necessarily mobile, since they are removed in a recombinative desorption process as water. The coverage of ethoxy species remaining after the low temperature desorption of ethanol (corresponding to reactions 3 and 4) was found to be approximately 25% of the original ethanol coverage.[155] Of the remaining 25% ethoxy species, approximately half desorbed as ethylene and half as ethanol after the β–hydrogen elimination step. This model could apply, *a priori*, to the $WO_3$ surface.

In our previous study of methanol desorption from the $WO_3(001)$ surfaces, we interpreted the thermal desorption curves in terms of surface heterogeneity and relatively rapid diffusion of molecularly adsorbed methanol on the basis of Monte Carlo simulations. [154] The coverage dependent desorption curves can be simulated using a distribution of adsorption site energies, as shown in Figure 3.7. Because no decomposition products of methanol were observed on either the oxidized or reduced surface, the methanol desorption spectra can essentially be used as a probe of the strength of the distribution of all available adsorption sites. By contrast, for the larger alcohols, the more strongly bound sites may lead to alkene production and therefore the alcohol desorption spectra only contain information about the sites that lead to associative desorption (Eqn. 4).

The surface heterogeneity of our films can be attributed to both electronic and morphological factors. The electronic contributions to the heterogeneity of these $WO_3$ surfaces have been characterized experimentally by XPS and UPS.[154] The surface lattice oxygen is preferentially removed during treatment of the surface, resulting in a mixture of $W^{5+}$ and $W^{6+}$ [154] and probably formation of CS type line defects. Furthermore, SEM and STM images have shown that, despite epitaxial growth, our $WO_3$ surfaces are heavily stepped.[161]

In this model, there is a certain fraction of the defect sites that strongly bind the alkoxy intermediate. As the temperature increases, the surface hydroxyls produced in dissociative adsorption are removed via recombination (Eqn. 5), while the rate of desorption of alcohol is substantially reduced (Eqn. 4) for the strongly bound alkoxy species. This implies that the alcohol is sufficiently mobile that, even at low coverage,

the alcohol can find these strong adsorption sites. According to our Monte Carlo simulations [154], the behavior of the coverage-dependent desorption curves, in which the trailing edge overlaps, indicates that the diffusion rate is larger than the desorption rate for water, methanol, ethanol and isopropanol on both the oxidized and reduced $WO_3(001)$ surfaces. Therefore, we believe that this assumption is valid. A second assumption is that the hydroxyl groups are mobile, such that at low coverage, recombinative desorption (via Eqn 5) is possible. The low temperature desorption of water from dissociatively adsorbed alcohols suggests that hydroxyls are relatively mobile, as shown in Figure 4.1C to 4.4C.

The implication of this model is that the selectivity toward dehydration should be substantially higher when the number of defects with binding energy greater than some threshold is increased. Indeed, the desorption temperature is always higher on the reduced surface than on the oxidized surface, which implies that the distribution of binding energies is shifted to higher binding energy on the reduced surface. However, Figure 4.6 shows that the oxidized surface does not exhibit significantly different dehydration activity than the reduced surface for either ethanol or isopropanol. Therefore, we find no evidence to support the defect model, at least under the low coverage conditions of the reactions on $WO_3(001)$ surfaces. Tanner, et al.[47] suggest that the sites for dehydration are the 5-fold coordinated $W^{6+}$ ions, and find no evidence that alkoxy species preferentially adsorb on step or other defect sites. This is consistent with our results.

#### 4.3.2.2. Selectivity controlled by diffusion and surface kinetics

An alternative view is that the selectivity is controlled by the rates of diffusion and reaction kinetics, and that "special" defect sites are not necessarily important. The coverage of alkoxy species that remain is simply the result of a competition between the kinetics of recombinative desorption of hydroxyls (Eqn 5) and associative desorption of hydroxyls and alkoxy species (Eqn 4). Whereas the desorption rate (Eqn 4) for associative desorption of the alcohol may decrease from methanol to ethanol to isopropanol, the recombinative desorption of surface hydroxyls is coverage dependent, but should not depend on the alcohol. In this model, as was necessary in the defect controlled model, surface hydroxyls must be mobile if the rate of Eqn 5 is going to be competitive with the rate of associative alcohol desorption.

In our previous studies of methanol CTDS on $WO_3(001)$ surfaces, UPS shows that methanol molecularly adsorbs on the oxidized $WO_3$ thin film surface and dissociates on the reduced surface.[154] The intensity of the UPS band due to the oxygen lone pair electron on the molecularly adsorbed methanol is significantly reduced, which we attribute to adsorption of methanol through a strong interaction between oxygen and a surface tungsten cation.[154] On the reduced surface, the UPS spectrum contains only three bonds, which easily distinguish methoxy species from the 5-featured spectrum of methanol.[154] However, methanol is the only species detected on both surfaces during the desorption experiments. This implies that the rate of desorption of methanol through reactions (3) or (4) is fast compared to the rate of associative desorption of hydroxyls (Eqn. 5). For ethanol and isopropanol, we do not have direct evidence regarding the fraction of alcohol that is associatively vs. dissociatively adsorbed. However, it is clear

that some fraction dissociates from the alkene production. For ethoxy/ethanol and isopropoxy/isopropanol, neither UPS nor vibrational spectroscopy is able to distinguish these species from each other particularly in a mixture.[125,162]

On metal surfaces, the shape of desorption spectra are frequently used to distinguish first order desorption (Eqn. 3) from second order desorption (Eqn. 4).[163-166] Figures 4.2A and 4.4A show that the desorption temperatures for ethanol and isopropanol on the oxidized $WO_3(001)$ surface decreased with increasing surface coverage, which is similar to the desorption of methanol on the oxidized $WO_3(001)$ surface.[154] In particular, the desorption curves for different coverages for water and all of the alcohols have a common tail on the high temperature side. This behavior can be described, on both the oxidized and reduced surfaces, by first order desorption kinetics with surface heterogeneity and rapid diffusion. We note that rapid diffusion of alcohols was also detected on the single crystal $WO_3(001)$ surface by Tanner, *et al.*[47] A slow surface diffusion process would result in a broad desorption profile but coverage-independent desorption peak temperatures, as reported by Nelson, *et al.*, for water desorption from the $\alpha$-$Al_2O_3(0001)$ surface.[103] The broad temperature range of the desorption peaks implies a wide distribution of surface adsorption energies. Our Monte Carlo model for methanol desorption indicated that, although diffusion of methanol was significantly faster than desorption on both surfaces, the shape of the coverage dependent curves was consistent with a first order- or pseudo-first order-process on both the oxidized and reduced surfaces, respectively, even though methanol was molecularly adsorbed on the oxidized surface and dissociatively adsorbed on the reduced surface. Therefore, the shape of the desorption spectra are not able to determine the adsorption state.

Spitz, *et al.*[167] showed that the relative acidity of Brønsted acids on oxide surfaces is consistent with that in aqueous solutions. The acidity of methanol, $pK_a = 15.5$, is slightly stronger than for ethanol, $pK_a = 15.9$, and significantly larger than isopropanol, $pK_a = 17.1$. By comparison to the adsorption state of methanol on the $WO_3(001)$ surfaces and the weaker acidities of ethanol and isopropanol compared to methanol, we might expect that ethanol and isopropanol would only adsorb molecularly on the oxidized $WO_3(001)$ surface and would be less likely to adsorb dissociatively on the reduced surface than methanol. However, our experiments show that significant amounts of alkene were produced by dehydration of ethanol and isopropanol on both the oxidized and reduced $WO_3(001)$ surfaces, as shown in Figure 4.1B to 4.4B. A detailed understanding of the acid dissociation equilibria would require information about the temperature dependence of the alcohol dissociation. We suggest that the coverage of the alkoxy that remains after dehydroxylation is a result of the stronger dispersion interactions of the larger alcohols with the surface, and therefore, higher desorption temperature of the larger alcohols, leading to greater dissociation at higher temperature. Before the alcohol desorbs, dehydroxylation occurs.

Once the surface alkoxy coverage at high temperatures is established, the selectivity between alkene production and reaction of the hydroxyls produced by β–hydrogen elimination to form water or alcohol should again be dependent on the coverage and diffusion rates. When the coverage is low and hydroxyl diffusion is facile, then a larger fraction of the hydroxyls may be lost as water, rather than through associative desorption of alcohol.

Previous studies show that the ratio of alkene to alcohol desorption at relatively high coverage in the high temperature peak is close to 1:1 for alcohols on the $TiO_2(001)$ surface[84] and ethanol on the $TiO_2(110)$ surface[155]. Kim and Barteau[84] proposed that the formation of alkene and alcohol at high temperature is a kinetically related process; the β-hydrogen abstracted from one alkoxy during formation of alkene is used to hydrogenate another alkoxy to form an alcohol molecule.

Compared with the dehydration reaction of alcohols on $TiO_2$ surfaces,[84,155] the yield of alcohol molecules with respect to alkene production on the $WO_3$ surfaces at high temperature is much lower. This observation is more prominent for isopropanol on the $WO_3$ surfaces than for ethanol. Figures 4.3 and 4.4 clearly show that with the increasing production of propylene around 500 K, the desorption of isopropanol in the corresponding temperature region does not grow significantly as observed on the $TiO_2(001)$ surface[84]. This again suggests that the rate of recombinative hydroxyl desorption is faster than associative desorption of the alcohol.

# SURFACE REACTIONS OF ETHERS ON $WO_3$(001) SURFACES

## 5.1. Introduction

Semiconducting $WO_3$ thin films, grown epitaxially on single crystal $Al_2O_3(1\bar{1}02)$ substrates, have been studied extensively in our laboratory as a potential chemiresistive sensor material.[33,69-71] The sensor response involves a change in the oxygen vacancy concentration, which is related to the film's conductivity. The vacancy concentration is determined by the relative rates of oxidation (by $O_2$) and reduction (e.g. by hydrocarbon) reactions. Therefore, a fundamental understanding of the extent to which different molecules can be distinguished requires knowledge of both the rate limiting steps and the charge transfer in the redox reaction step(s). In Chapters 3, 4 and 6, we have reported calibrated thermal desorption spectroscopy data for methanol, ethanol and isopropanol, and dimethyl methylphosphonate (DMMP). In order to elucidate the relationship between the surface catalytic activity and surface structure, two different surfaces, "reduced" and "oxidized" surfaces, were created in the same way for all of these studies.

Our experiments show that the reduced and oxidized surfaces exhibit different activities to DMMP and methanol adsorption. With DMMP adsorption, methanol and dimethyl ether are produced on the oxidized surface; however, only dimethyl ether is formed on the reduced surface. Methanol molecularly adsorbs on the oxidized surface, but dissociates to a large extent on the reduced surface. In contrast to behavior on $V_2O_5$ and $TiO_2$(001), methanol does not couple to dimethyl ether and is not oxidatively dehydrogenated to formaldehyde on either surface.

In contrast, we find no significant difference between the surfaces toward oxidative dehydration of ethanol and isopropanol. The selectivity is coverage dependent, which we attribute to competitive desorption of alcohol and recombinative dehydroxylation, which leaves alkoxy intermediates. These species decompose via β-H elimination and C-O bond scission at a similar temperature on the two surfaces.

In this chapter, we studied the surface reactions of dimethoxymethane on the reduced and oxidized $WO_3(001)$ surfaces with the calibrated thermal desorption spectroscopy (CTDS). Dimethoxymethane (DMM), also known as methylal, is used in cosmetics and pharmaceuticals and has been studied intensively as an alternative to diesel fuel.[168-171] DMM, $CH_3$-$OCH_2O$-$CH_3$, can be viewed as a di-ether whose acidity should be higher than methanol, because of the greater polarization of the C-H bond. The pair of oxygens offer two Lewis base interactions compared to the single one in dimethyl ether. We find that dimethyl ether adsorbs and desorbs molecularly with a desorption temperature consistent with adsorption through the oxygen lone pair at a Lewis acid site. By contrast, DMM desorbs through two channels, molecular desorption and decomposition to yield methanol. On the oxidized surface, a single Lewis acid-base interaction is suggested, while on the reduced surface, a higher temperature desorption peak may be due to two Lewis acid-base interactions.

## 5.2. Results

### 5.2.1. DMM interaction with the reduced $WO_3(001)$ surface

Figure 5.1 shows a representative thermal desorption spectrum of DMM on the reduced $WO_3(001)$ surface. The peaks at 400 K are assigned to the desorption of

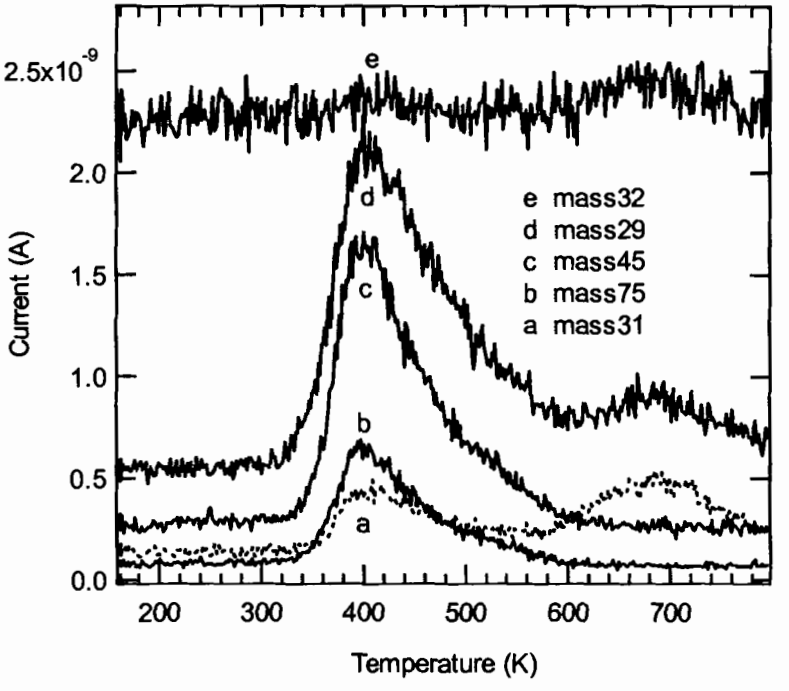


**Figure 5.1.** A representative desorption spectrum of dimethoxymethane (DMM) on the reduced $WO_3(001)$ surface. The desorption peak at 400 K is attributed to molecular desorption of DMM, while the peak at 690 K is assigned to desorption of methanol, produced from decomposition of DMM, based on their fragmentation patterns.

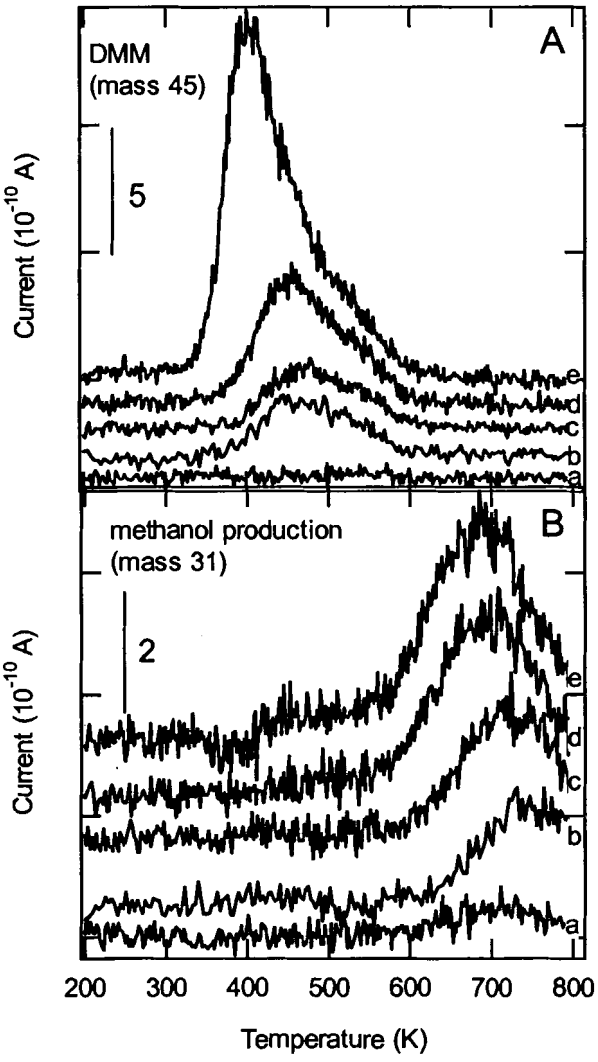


**Figure 5.2.** Coverage dependence of dimethoxymethane desorption and corresponding production of methanol on the reduced $WO_3(001)$ surface. A) A series of DMM molecular desorption spectra (mass 45) with increasing coverage. Note the two overlapping desorption peaks in curves b and c (compare to Figure 5.4A). B) Methanol production from the decomposition of DMM. Spectra were offset for clarity.

molecular DMM, based on its consistency with the gas phase fragmentation pattern of DMM. Masses 29, 31 and 32 showed a second peak at 690 K. Since the fragmentation pattern of this peak is consistent with the fragmentation pattern of methanol[172], the 690 K peak is attributed to desorption of methanol produced during decomposition of DMM on the reduced $WO_3$ surface.

The desorption spectra of DMM and methanol, evolved from decomposition of DMM, on the reduced surface are presented in Figure 5.2 for different initial DMM surface coverages. As the surface coverage increased, the desorption temperature decreased as shown in Figure 5.2A, consistent with previous observations of water and alcohol desorption,[154,173] which is due to the rapid surface diffusion and heterogeneity. For the lower coverage spectra, curves b and c, there are two peaks centered around 450 and 540 K. With increasing surface DMM coverages, the corresponding production of methanol (Figure 5.2B) increased while the desorption temperature decreased slightly. The methanol desorption temperature is high compared to molecular desorption when methanol is adsorbed, implying a reaction limited process for production of methanol.

### 5.2.2. DMM interaction with the oxidized $WO_3$(001) surface

The thermal desorption spectrum is displayed in Figure 5.3 for DMM on the oxidized $WO_3$ surface. As with DMM on the reduced $WO_3$ surface, the desorption around 350 K is assigned to desorption of DMM molecules and the peak in the 29, 31, and 32 amu spectra above 700 K are assigned to desorption of methanol. A family of desorption spectra for desorption of DMM and the methanol produced at different coverages is presented in Figure 5.4. Note that the peak width is considerably narrower

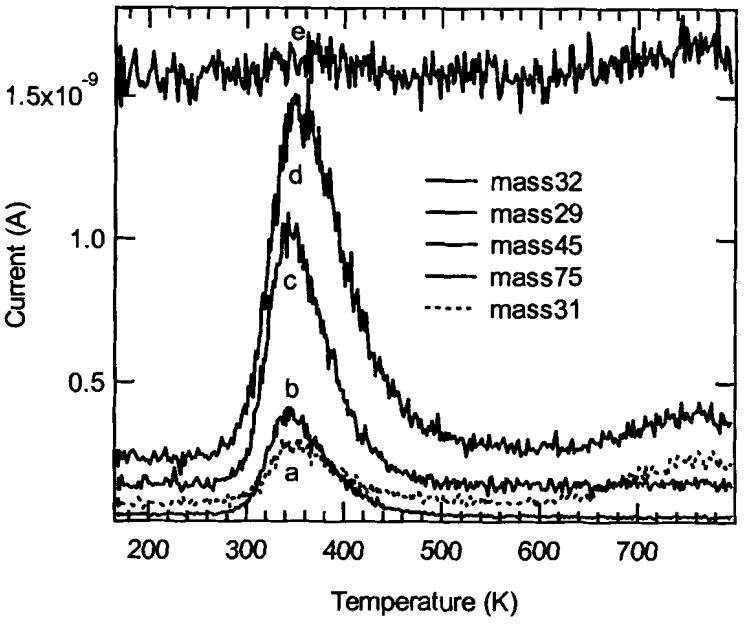


**Figure 5.3.** A representative desorption spectrum of DMM on the oxidized $WO_3(001)$ surface. The desorption peak at 350 K is attributed to molecular desorption of DMM; the absolute coverage of the methanol desorption peak above 700 K, produced from decomposition of DMM, is significantly reduced compared to the reduced surface (Figure 5.2B).

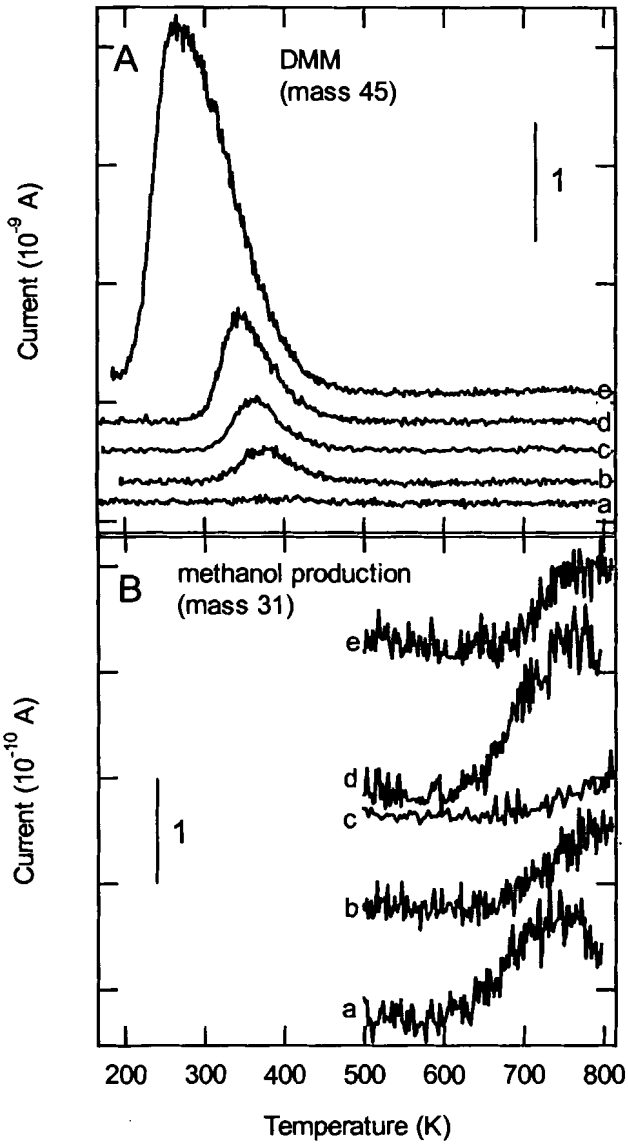


**Figure 5.4.** Coverage dependence of dimethoxymethane desorption and corresponding production of methanol on the oxidized $WO_3(001)$ surface. A) A series of DMM molecular desorption spectra with increasing coverage, and B) the corresponding methanol production from the decomposition of DMM. Spectra were offset for clarity.

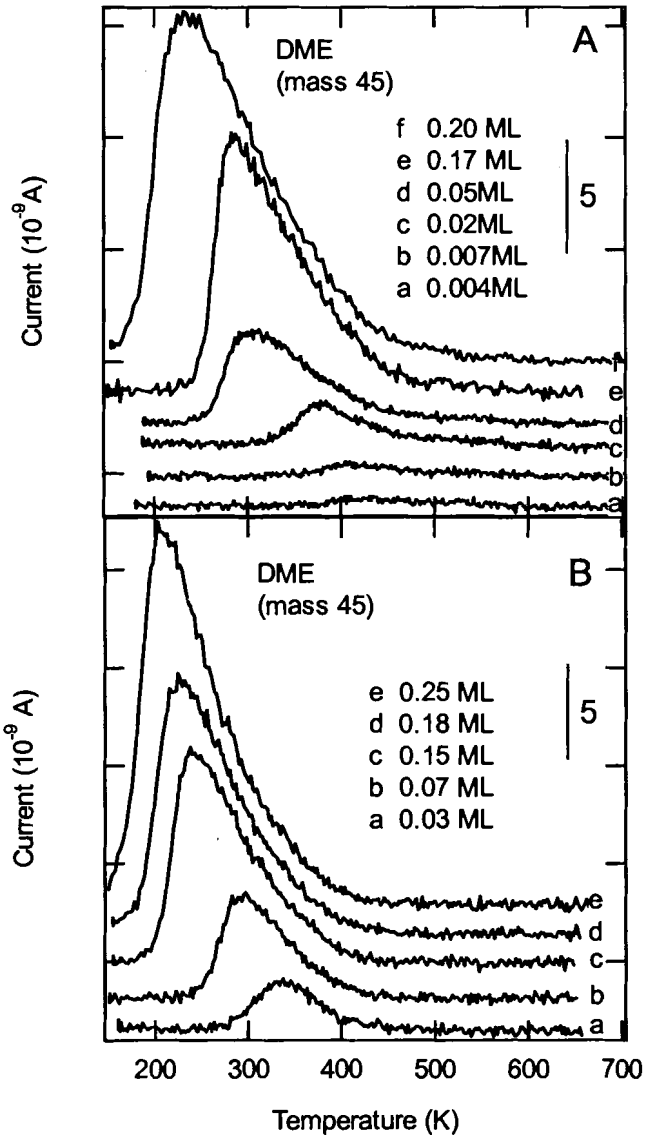


**Figure 5.5.** Dimethyl ether desorption spectra at the initial coverages indicated A) on the reduced $WO_3(001)$ surface and B) on the oxidized surface. Spectra were offset for clarity.

than on the reduced surface and consists of a single peak. The desorption temperature of DMM on the oxidized surface decreases with increasing surface coverage and is 80-100 K lower than the lower temperature peak on the reduced surface. We typically find that the molecular desorption peaks are stronger for the alcohols on the reduced surface, resulting in a temperature shift of this magnitude. Compared to the molecular DMM peak, the production of methanol on the oxidized surface shown in Figure 5.4B, is reduced by a factor of three or four and is shifted to higher temperature.

During the DMM thermal desorption experiments, mass fragments associated with CO, $CO_2$, $CH_4$, and dimethyl ether were monitored, both on the oxidized and reduced $WO_3$ surfaces, but no significant desorption peaks were detected. On the oxidized surface, only a weak water desorption peak was detected below 400 K, attributed to background adsorption. Formaldehyde was not observed on the reduce surface but was detected around 300 K on the oxidized surface after a high dose, which was assigned to the coadsorption of contaminant formaldehyde with DMM.

### 5.2.3. Dimethyl ether interaction with $WO_3$(001) surfaces

The thermal desorption spectra of DME on the reduced and oxidized $WO_3$ surfaces are presented in Figure 5.5A and 5B, respectively. The desorption temperature of DME decreased with increasing surface coverage on both surfaces, which we ascribe to the effects of surface heterogeneity and relatively rapid diffusion.[154] On the reduced surface, the desorption temperature in the low coverage limit approaches 420 K, while on the oxidized surface, it is below 400 K. We did not observe production of methanol on either surface.

## 5.3. Discussion

### 5.3.1. Adsorption states of ethers on $WO_3$(001) surfaces

Our previous study showed, using UPS, that methanol adsorbs molecularly on the $WO_3$ surface by interaction of the oxygen lone pair electron with a surface tungsten cation.[154] Similarly, we expect that DMM and DME adsorb, in the molecular state, on the surface through the interaction of oxygen lone pair electrons with surface tungsten cations. The peak desorption temperatures in the zero coverage limit from the methanol[154], ethanol[173], isopropanol[173], and ether desorption measurements are compared in Table 5.1. The trend appears to correlate with the molecular weight on both surfaces, with an approximately 100 K difference between the oxidized and reduced surfaces. Therefore, the desorption temperatures for DME and the lower DMM peak seem to be consistent with a Lewis base interaction at single exposed tungsten cation sites. We have compared our XPS and UPS data[154] for the reduced surface with that of Dixon, *et al.*,[50] in which their STM images show (1x1) structures in which all of the terminal oxygens are lost. This provides an opportunity for adsorption of DMM through the oxygen lone pairs on both oxygens, as suggested in Figure 5.6A. The oxygen-oxygen separation is approximately 2.35 Å, compared to the W-W distance of 3.5-3.7 Å in the bulk terminated (001) surface. However, the W-W distance should be about 2.6 Å in crystallographic shear planes, as shown in Figure 5.6B. Therefore, we suggest that the higher, 550 K peak in Figure 5.2A may be attributed to DMM bonded to two W cation sites.

**Table 5.1.** Comparison of desorption peak temperatures for alcohols and ethers on the $WO_3(001)$ surfaces at the zero coverage limit.

| Molecules and desorption peak temperatures | | | | | |
|---|---|---|---|---|---|
| MW | 32 | 46 | 46 | 60 | 76 |
| adsorbate | Methanol | DME | Ethanol | Isopropanol | DMM |
| oxidized surface | 360 K | 350 K | 410 K | 430 K | 380 K |
| reduced surface | 390 K | 410 K | 430 K | ~530 K | 460 K<br>550 K |

Further support for molecular adsorption of DME comes from comparison with the reactivity of methanol on our $WO_3$ surfaces. Previous studies have shown that DME dissociates on the $ZrO_2$ and $CeO_2$ surfaces to form methoxy adsorbed on the surface.[85,174] However, our previous study showed that $WO_3$ is not active in catalyzing the coupling reaction between adsorbed methanol molecules to form DME, even on the reduced surface where methanol dissociates to form methoxy species. The methoxy species desorb by combining with a surface hydroxyl to form methanol. This suggests that if methoxy were produced during dissociative adsorption of DME, then desorption of methanol would be observed. The methanol was not detected on either surface, which also implies that DME molecularly adsorbs on the $WO_3$ surfaces.

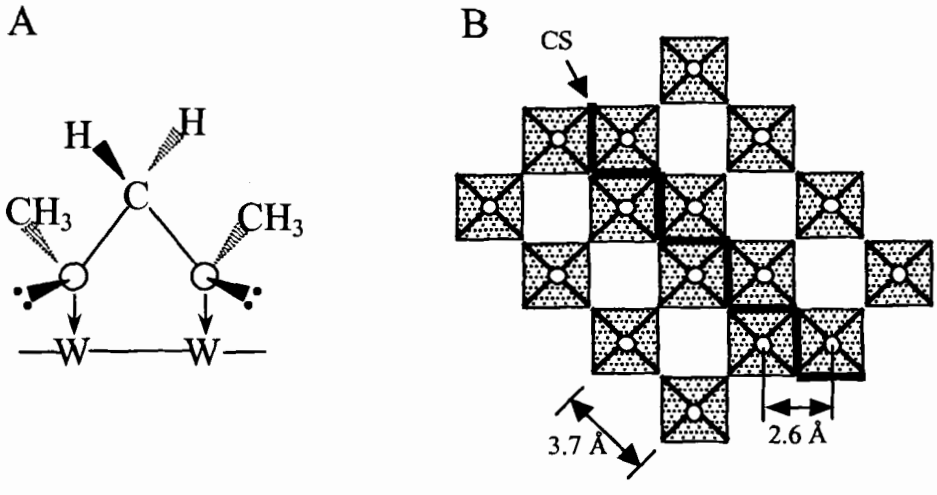


**Figure 5.6.** An adsorption state of dimethoxymethane (DMM) on the crystallographic shear (CS) plane domain. A) The adsorption of DMM molecule on tungsten cations through 2 oxygen lone pair Lewis acid-base interactions. Normal 5-fold $W^{6+}$ sites with a spacing of 3.7 Å would not be favorable for this adsorption configuration; however, the CS structure, shown in B), provides appropriate geometric sites with tungsten cation spacing of 2.6 Å that are more amenable for this adsorption state.

### 5.3.2. Mechanism for surface reactions

We now consider the decomposition of DMM and the production of methanol above 600 K. Our previous study of methanol on the $WO_3$ surfaces showed that the majority of methanol desorbs below 450 K on the reduced surface and below 400 K on the oxidized surface. However, a very weak methanol desorption peak occurs above 600 K on both the reduced and oxidized surfaces.[154] The methanol that evolved from DMM decomposition and desorbed above 600 K on both surfaces would appear to be a reaction limited process. Although there must be associative desorption of methoxy species, formed in the decomposition of DMM, the desorption temperature is lower on the reduced surface than on the oxidized surface, which is rather unusual. In our analysis of the selectivity of the alcohol dehydration reactions, we concluded that diffusion and competition between dehydroxylation of surface hydroxyls and associative desorption of the alcohol was more important than the surface defect structure. An analogous process may be important here, since the lower temperature desorption occurs at higher coverage. The reduced surface dissociates DMM to a greater extent, and second order kinetics would then predict a lower temperature with increasing coverage.

# EFFECT OF SURFACE REDUCTION ON DECOMPOSITION OF DIMETHYL METHYLPHOSPHONATE ON TUNGSTEN TRIOXIDE SURFACES

## 6.1. Introduction

Considerable interest has been shown in finding effective ways to decompose and detect organophosphorous compounds, such as pesticides and warfare agents, for environmental and human safety reasons. Understanding the surface chemistry of these compounds in the environment is of fundamental importance for modeling their spread and degradation.[175] Dimethyl methylphosphonate (DMMP) is commonly accepted as a model compound for warfare agents in laboratory studies due to its similar structure and lower toxicity. The decomposition of DMMP on different metals and metal oxides has been widely studied.[74,76-81,176]

Early research work was done by Templeton and Weinberg [80] on the adsorption of DMMP on the hydroxylated aluminum oxide surface, with inelastic electron tunneling spectroscopy (IETS). They found that DMMP molecularly adsorbs on the surface at 200 K, either through hydrogen bond formation between the phosphoryl oxygen and a surface hydroxyl group or through bonding of the phosphoryl oxygen to a surface Lewis acid site, $Al^{3+}$. As the temperature is increased above 295 K, one of the phosphorus-methoxy bonds (P-$OCH_3$) breaks. Above 573 K, another methoxy group is lost. The resulting methylphosphate species is thought to adsorb on the surface in a tridentate form.

White and coworkers studied the adsorption of DMMP on Pt(111), silica and $\alpha$-$Fe_2O_3$ surfaces [79,176] using High Resolution Electron Energy Loss Spectroscopy (HREELS), Static Secondary Ion Mass Spectrometry (SSIMS) and Temperature

Programmed Desorption (TPD). Below 300 K DMMP molecularly adsorbs on the Pt(111) surface through the phosphoryl oxygen [176], while above 300 K, both PO-C and P-OC bonds are broken, and between 400-500 K, the P-$CH_3$ bond breaks. $PO_x$ species remain on the surface to very high temperatures. On the dehydroxylated silica surface, DMMP does not decompose during adsorption [79]. For the hydroxylated silica surface, less than 10% of a monolayer of DMMP decomposes. On the clean $\alpha$-$Fe_2O_3$ surface, the desorption of DMMP multilayers is observed around 200 K [79] and the monolayer desorption of DMMP is observed at 410 K. As the temperature is increased to above 247 K, all of the P-$OCH_3$ and P-$CH_3$ bonds of DMMP break. The desorption products are $H_2O$, CO, $CO_2$, $H_2$, $CH_3OH$ and HCOOH, which are observed above 500 K. Accumulation of phophorus on the $\alpha$-$Fe_2O_3$ surface eventually causes the surface to be poisoned.[74]

Mitchell and coworkers have studied the adsorption of DMMP on the aluminum oxide, magnesium oxide, lanthanum oxide and iron oxide surfaces using infrared spectroscopy [74]. They found that the adsorption and decomposition mechanism is similar for the first three oxides. DMMP is anchored to the surface through interaction of the phosphoryl oxygen with a Lewis acid site, which results in a down shifted P=O vibrational frequency. The two methoxy groups are lost sequentially, as the temperature is increased. However, the P-$CH_3$ group is still on the surface to quite high temperatures. As for the iron oxide surface, as the temperature increases, infrared shows that both the P-$OCH_3$ and the P-$CH_3$ bonds are broken at the same time with methoxy intermediates detected.

Yates and coworkers used infrared to study the adsorption of DMMP on $TiO_2$ powders [76]. They found that at low temperature, on the hydroxylated $TiO_2$ surface DMMP adsorbs through hydrogen bonding between the phosphoryl oxygen and surface hydroxyl groups, which is similar to the case of DMMP adsorption on the $Al_2O_3$ surface. As the temperature increases above 214 K, the surface methoxy intermediate is observed. Around 486 K, methyl methylphosphonate (MMP) is left on the surface in a bidentate adsorption state.

The decomposition of DMMP on high surface area $WO_3$ powders has been studied by Kim, *et al.* using infrared spectroscopy [81], showing that decomposition occurs through breaking the P-$OCH_3$ bonds with the P-$CH_3$ group remaining on the surface to very high temperatures.

While most of the studies of DMMP on metal oxide surfaces have focused on the decomposition intermediates, less work was conducted on surface reaction products and decomposition mechanisms. For sensor applications, the significance of studying the surface reactions lies in the fact that the conductivity change is ultimately determined by the amount of oxygen removed from the oxide surface and the kinetics of the rate limiting step.

In catalysis, $WO_3$ is known as one of a class of compounds, including $V_2O_5$ and bismuth molybdate mixed metal oxide compounds, that are selective- or partial-oxidation catalysts. For example, propylene is oxidized to acrolein, rather than $CO_2$,[2] and methanol reacts via an oxidative dehydrogenation process to form formaldehyde and $H_2O$. Isotope labeling studies, in particular, have demonstrated clearly that the oxygen incorporated into the product comes from the lattice, rather than directly from oxygen in

the feedstream.[177,178] Thus, the relative ease with which oxygen can be provided to a reacting species leads to incorporation of oxygen; however, the lattice oxygen is much less reactive than surface adsorbed ionic species such as $O^-$ and $O_2^-$ which generally lead to complete combustion. The oxide is then reoxidized by the feedstream to complete the catalytic cycle.

The ability of $WO_3$ to exchange oxygen is similar to other partial oxidation catalysts; however, there are some distinct structural differences. The $WO_3$ structure is constructed through formation of W-O-W chains in three dimensions, forming a nearly cubic, $ReO_3$-type structure. It can also be described in terms of corner sharing octahedra. Slight tilt and distortion of the octahedra give rise to different lower symmetry structures and several bulk phases are described.[53] Pure $WO_3$ is a good insulator with a band gap of 2.7 eV.[153] The semiconducting properties of $WO_3$ are associated with oxygen vacancies or crystallographic shear (CS) planes [107,109,114]. Haber, *et al.* [140] have suggested that only the phases of $WO_{3-x}$ which readily form CS structures are the ones responsible for facile insertion of oxygen into hydrocarbons. Furthermore, while the structure of $MoO_3$ is similar, isolated oxygen vacancies are present in $MoO_3$, but not $WO_3$.

Our research effort has been focused on developing tungsten oxide semiconducting thin film based sensors for the detection of toxic organophosphorous compounds [71,110]. However, the major challenge is the lack of selectivity, since this sensor not only responds to organophosphorous compounds, such as DMMP, but also responds to other organic compound interferents, such as methanol. Whereas selectivity in catalysis refers to the ability of a catalyst to convert one reactant in the feedstream to one product, a selective sensor should respond ideally to only one, or perhaps a limited

class, of compounds in a mixture of gases. Since the primary information contained in the sensor response is a measure of reaction rates, the ability to distinguish different compounds depends upon differences in activation energy barriers for the rate limiting steps. This motivated us to investigate the decomposition and surface reaction mechanism of DMMP and methanol on $WO_3$ thin film surfaces.

In this chapter, we studied the decomposition and reaction mechanisms of DMMP on epitaxially grown $WO_3(001)$ thin films on $\alpha$-$Al_2O_3$ substrates by calibrated thermal desorption spectroscopy (CTDS) [88] and x-ray photoelectron spectroscopy (XPS). The experiments were conducted on two different surfaces, an $Ar^+$ sputtered and annealed surface and an oxidized surface, in order to study the effects of surface reduction on the decomposition of DMMP. XPS was used to characterize the surface by monitoring the W4f and valence band regions of the surfaces. The XPS W4f band and the UPS valence band region in this study showed similar features to that found in the studies by Dixon, *et al.* [50] for $WO_3(001)$ single crystal surfaces prepared under similar conditions and characterized using XPS, UPS and STM. Therefore, the surface structures can be characterized based on the STM studies by Dixon, *et al.* and Jones, *et al.* [133].

The study showed that DMMP evolves from the surface via two separate routes. Molecular desorption occurs from majority sites at temperatures around 600-700 K. DMMP on more active sites decomposes to produce dimethyl ether and methanol on the oxidized surface, but only dimethylether was observed on the reduced surface. By comparison with previous studies of the adsorption and desorption of methanol and dimethyl ether on $WO_3(001)$ surfaces, we propose that DMMP generates dimethyl ether in an intramolecular rearrangement in a single step, rather than through a stepwise

mechanism [74,81] and surface mediated coupling reaction previously suggested from infrared studies. Our XPS measurements are consistent with IR data [81] that show that a methyl phosphate-like species remain on the $WO_3$ surface.

## 6.2. Results

### 6.2.1. XPS characterization of the oxidized and reduced $WO_3$ surfaces

Figure 3.1 shows the structure of monoclinic $WO_3$, and the non-polar c(2×2) $WO_3$(001) surface, with the lattice vectors relative to the idealized, cubic $ReO_3$ structure. Two types of oxygen exist on the bulk terminated (001) surface, terminal oxygen and bridging oxygen. In the c(2×2) surface, half of the terminal oxygens are removed, to produce a stable surface.[109,114] Sputtering may preferentially remove oxygen, either in the terminal or bridging positions, to result in a reduced, disordered surface. Formally, the five-coordinate tungsten cations, with missing terminal oxygens, are in the 5+ oxidation state. However, annealing the surface would also be expected to produce shear plane structures, which also result in reduced formal cation oxidation states. At shear plane boundaries (see Figure 3.1C), in which an octahedron has two corner sharing and two edge sharing octahedra neighbors, the cations would also be in a 5+ formal oxidation state. Removal of the terminal oxygen from the cation at the shear plane would formally produce a 4+ oxidation state.

Figure 6.1 shows the W4f XPS spectra for the epitaxially grown $WO_3$(001) film treated in different conditions, showing that the ion sputtered or thermally treated surfaces (Figure 6.1 curves a-d) are complicated by the emergence of new bands in the

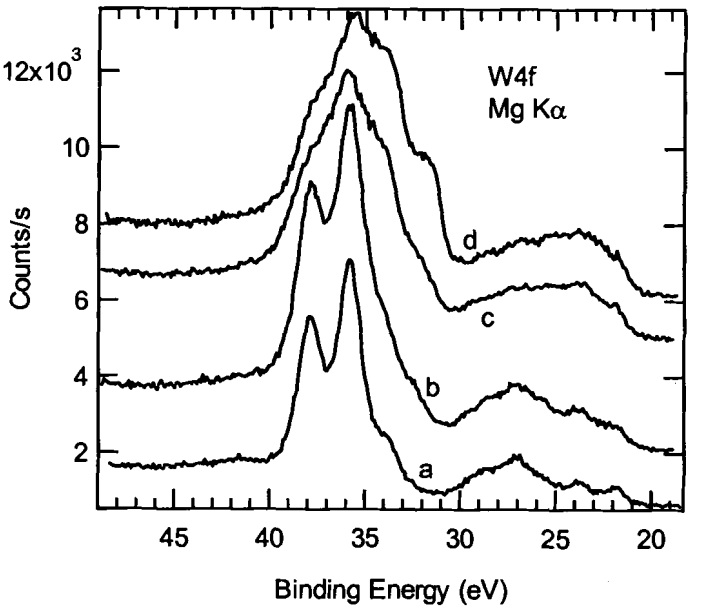


**Figure 6.1.** The W4f XPS spectra for $WO_3(001)$ surfaces treated under different conditions. **Curve a.** surface oxidized in 0.18 mbar $O_2$ at 300 °C for 3 hrs after sputtering; **curve b.** surface oxidized in 0.18 mbar $O_2$ at 200 °C for 2 hrs; **curve c.** surface sputtered by $Ar^+$ at beam energy of 500 eV and 100 μA for 110 secs; **curve d.** surface sputtered at the same $Ar^+$ beam conditions as for curve c for 240 secs.

lower binding energy region, whose intensity depends upon the extent of surface treatments.

Although the spectra can be fit[107,117-120] with components assigned to a range of initial states, $W^{6+}$, $W^{5+}$, $W^{4+}$ and $W^{0}$, for several reasons discussed in Chapter 3, we prefer the interpretation put forward by Dixon, *et al.*[50] This mechanism, which originates from many body effects, supposes that, when the electrostatic interaction between the photoionized core hole and an electron in the conduction band is strong enough to exceed the width of the conduction band, the conduction band state can be pulled down into the gap to form a localized state, [115] trapping the conduction electron. Two final states can be evolved, depending on the occupancy of the localized state; if the trap is occupied, final state screening results in a lower apparent binding energy (*i.e.* the "screened" final state) compared to the "unscreened" final state in the case when the trap is empty. For this mechanism, two final states are possible from the same initial oxidation state, and the relative intensity and shift are dependent upon the electron density near the Fermi level.[116]

Figure 6.1 curves b, c and d show W4f XPS spectra for the oxidized, reduced, and heavily sputtered surfaces, respectively. In Chapter 3, we have fit the spectrum of the oxidized surface, shown in Figure 6.1b, with two spin-orbit doublets, assigned to the $d^0$ final state of $W^{6+}$ ($W4f_{7/2}$ BE=35.8 eV) and the unscreened $d^1$ final state of $W^{5+}$ ($W4f_{7/2}$ BE = 33.9 eV). The spectra c and d in Figure 6.1 were fit with three spin-orbit doublets, assigned to the $d^0$ final state of $W^{6+}$ ($W4f_{7/2}$ BE=35.7 eV), the unscreened $d^1$ final state of $W^{5+}$ ($W4f_{7/2}$ BE = 33.7 eV) and the screened $d^2$ final state of $W^{5+}$ ($W4f_{7/2}$ BE = 31.8 eV).

The results of the final state model are given in Table 3.1. Small contributions from the W 5p level were neglected.[116]

Dixon, *et al.* [50] found that significant differences above the valence band (*i.e.* in the gap of stoichiometric $WO_3$), as measured with UPS, could be correlated with formation of "troughs" running across the c(2×2) terraces and "bright rafts" on more reduced surfaces, which was shown in a separate STM study to be the (1×1) structure of a $WO_2$ layer with all of the terminal oxygen removed.[50,133] Our spectra for the UPS valence band region and XPS W4f band [154] were very similar to the results obtained by Dixon, *et al.* [50] The similarity of our XPS and UPS data to that of Dixon, *et al.*, allows us to associate the oxidized surface with the c(2×2) structure, probably containing "troughs" and the sputtered (and annealed) surface with regions of "bright rafts" in which all terminal oxygen are removed. In any case, the XPS spectra shown in Figure 6.1b and 2c and UPS data similar to the corresponding data in the work of Dixon [50] characterize the oxidized and reduced surfaces, respectively, used for all of the experiments in this study.

### 6.2.2. DMMP decomposition on the reduced $WO_3$(001) surface

Figure 6.2 shows the CTDS spectrum after DMMP was adsorbed on the reduced surface at 140 K. Mass 94 fragments emerged at 580 and 200 K, while masses 45, 46 and 31 evolve at 350 K. Note the shoulder on the high temperature side of the mass 31 peak. In a separate experiment, in which masses 124, 79 and 94 were monitored simultaneously, we found that masses 79, 94 and 124 appeared in the high temperature peak around 580 K, but only masses 94 and 79 appeared around 200 K and the mass 79 peak at 200 K was very weak compared to mass 94. Comparison with the fragmentation

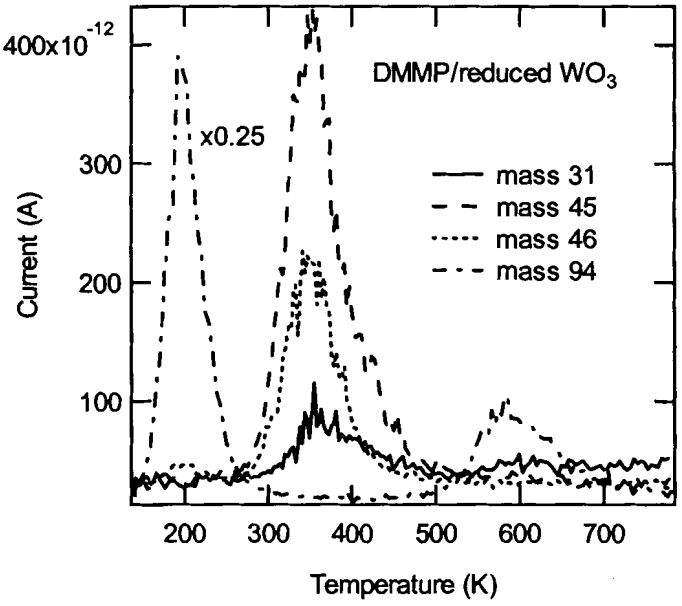


**Figure 6.2.** A representative set of desorption spectra following adsorption of DMMP on the reduced $WO_3(001)$ surface. DMMP molecular desorption was observed at 580 K and desorption of DME, produced from decomposition of DMMP, was observed at 350 K; the large desorption at mass 94 at 200 K is probably due to contaminant methyl bromide. (See text for details).

pattern of DMMP [172] shows that the desorption at 580 K was consistent with DMMP desorption, whereas the desorption at 200 K was not.

In experiments with DMMP that was not purified in the ice-salt bath after freeze-pump-thaw cycles, the desorption peak at 200 K was much larger in intensity, relative to the peak around 600 K, both on the oxidized and reduced $WO_3$ surfaces. With the contaminated DMMP, desorption at 200 K was also accompanied with a strong desorption feature identified by mass 45 around 400 K on the reduced $WO_3$ surface which, if present, is dramatically reduced in the CTDS experiments with the purified sample shown in Figure 6.2. The desorption of phosphorous-containing species, evolved from DMMP decomposition at 200 K, is unlikely because previous studies of the adsorption of DMMP on metal and metal oxides have consistently shown that phosphorous-containing species are stable on the surface to very high temperatures.[76,78,80,81] This suggests that the desorption at 200 K is most likely due to a contaminant in the DMMP. However, the desorption of surface reaction products at 350 K on the reduced surfaces, and at 340 K and 350 K on the oxidized surfaces, to be described below, were similar in the experiments with the contaminated and further purified DMMP samples. The species responsible for desorption at 200 K has not been conclusively identified in our experiments, but most closely resembles the fragmentation pattern of $CH_3Br$.

The desorption peak at 350 K was identified as dimethyl ether. The major cracking fragments for dimethyl ether are masses 45, 29, 46 and 15 [172] with mass 45 being the strongest component and mass 46 approximately 50% of the mass 45 intensity. All of the major fragments were detected at 350 K during our CTDS experiments for

DMMP on the reduced surface (for simplicity, only the major peaks at mass 45 and 46 are shown). The shoulder at mass 31 was found to appear accompanied with mass 75 (not shown) around 400 K. In CTDS experiments with the DMMP that was not purified in the ice-salt bath the mass 75 peak was remarkably enhanced. Therefore, we could not rule out the possibility that the desorption around 400 K was associated with DMMP, but we expect that it is most likely related to trace amounts of the contaminant that could not be entirely removed. During CTDS experiments, we did not detect the desorption of $H_2$, CO, $CO_2$, $CH_2O$ or $CH_3OH$ molecules during DMMP decomposition.

Figures 6.3B, 6.4B and 6.5B show the P2p, C1s and W4f XPS spectra for the reduced surface before and after being exposed to DMMP. The Fermi level was taken as the reference for correction of the peak shifts caused by surface charging. After the DMMP CTDS experiments, a strong P2p peak was developed at 133 eV, as shown in Figure 6.3B. A very weak shoulder was observed around 285 eV in the C1s region, as shown in Figure 6.4B and slight change was found in W4f XPS spectrum as shown in Figure 6.6B after DMMP exposures. The structure in the background of the C1s region is associated with loss structures in the tail of the W4d peak.

### 6.2.3. DMMP decomposition on the oxidized $WO_3$(001) surface

Figure 6.6A shows the CTDS spectrum of DMMP on the oxidized $WO_3$ surface after dosing at 140 K. Masses 94, 79 and 124 appeared at 600 K. A small mass 94 peak appeared at 200 K, while mass 79 was negligible, suggesting that the contaminant does not stick as well to the oxidized surface as the reduced surface. Masses 45, 46 and 29 emerged at 340 K. As for DMMP on the reduced surface, the desorption at 600 K was

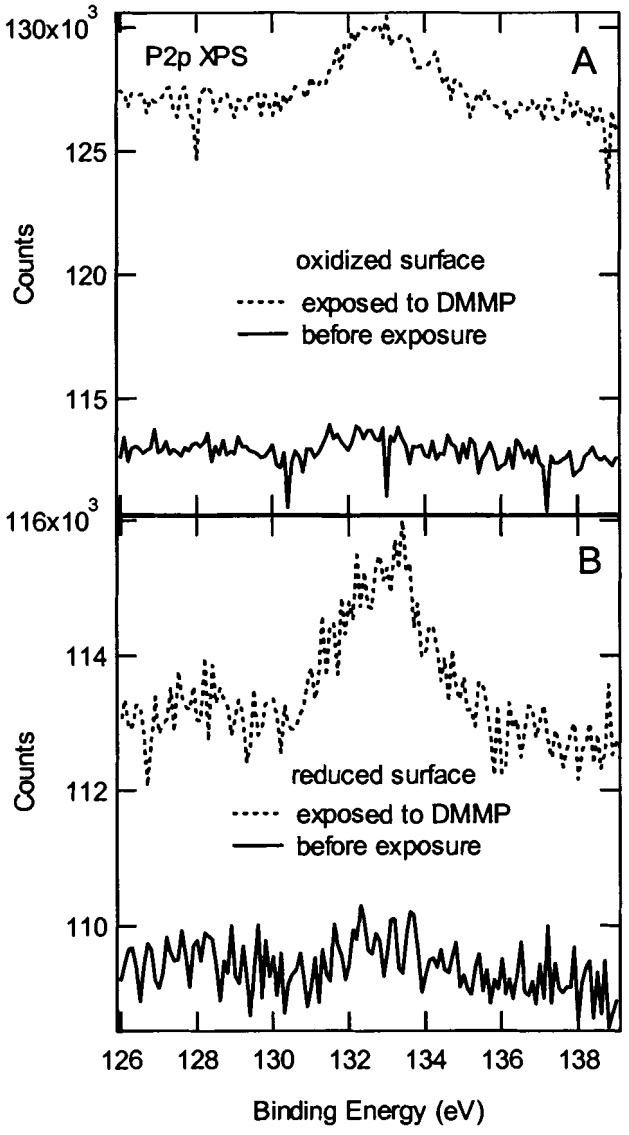


**Figure 6.3.** P2p XPS spectra before and after DMMP exposure on A) the oxidized $WO_3(001)$ surface and B) the reduced surface. Phosphorous was identified on both surfaces after DMMP exposure.

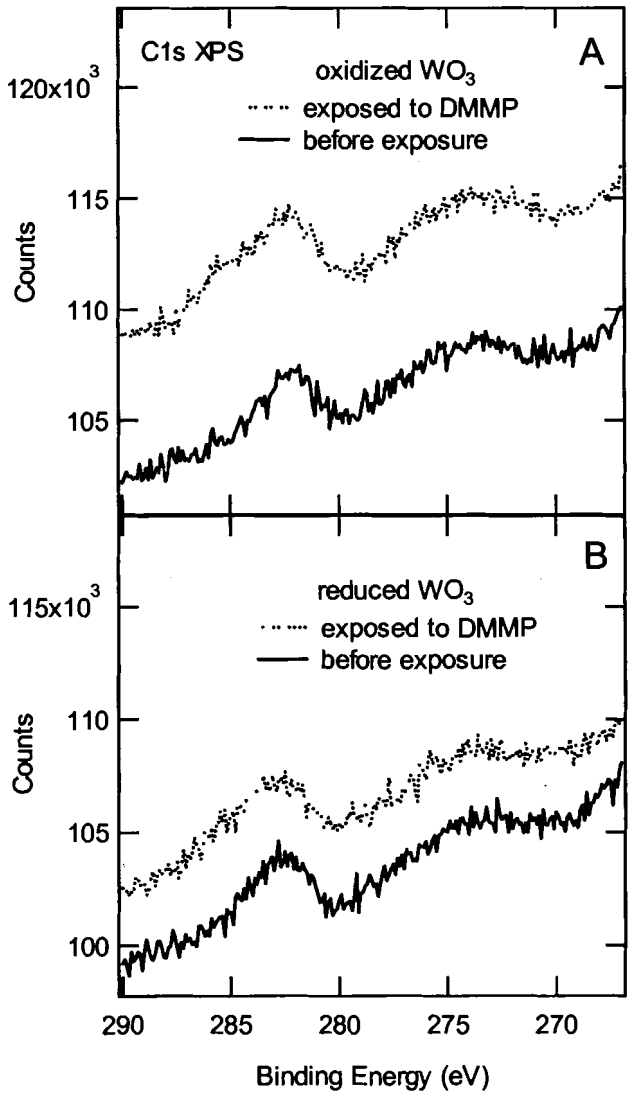


**Figure 6.4.** C1s XPS spectra before and after DMMP exposure on A) the oxidized $WO_3(001)$ surface and B) the reduced surface. A C1s peak was identified around 286 eV on both surfaces.

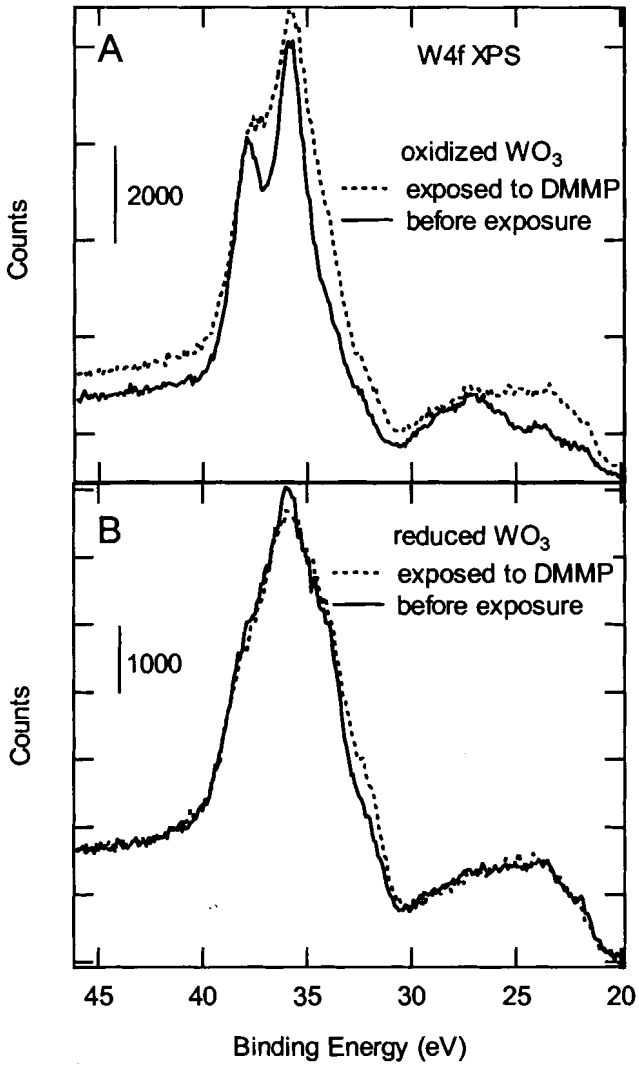


**Figure 6.5.** Comparison of W4f XPS before and after DMMP exposure on A) the oxidized $WO_3(001)$ surface and B) the reduced surface. Significant reduction of the oxidized surface was detected, but only small change in the reduced surface.

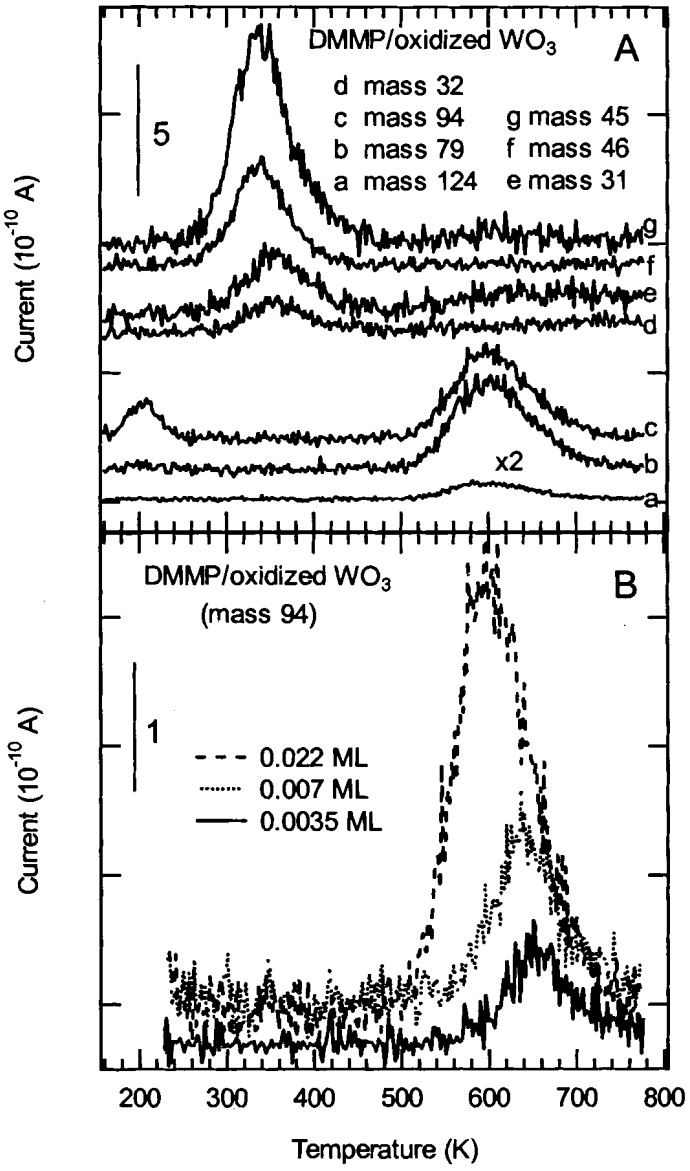


**Figure 6.6.** A representative set of desorption spectra following adsorption of DMMP on the oxidized $WO_3(001)$ surface (A) and coverage dependence of DMMP desorption on the oxidized surface (B). DMMP molecular desorption was found at 600 K and desorption of DME and methanol, produced from decomposition of DMMP, was observed at 330 K and 350 K, respectively; similar to the reduced surface, desorption at mass 94 at 200 K is not due to DMMP. Spectra in (A) were offset for clarity.

assigned to molecular DMMP desorption, the desorption at 200 K was not due to DMMP, and dimethyl ether desorbed at 340 K. In addition, masses 31 and 32 appeared at 350 K, very close to the desorption temperature of dimethyl ether. This desorption peak was ascribed to methanol desorption. Mass 31 is the strongest component in the methanol fragmentation pattern, and the molecular ion, mass 32, is about 70% of mass 31 in intensity [172]. $H_2$, CO, $CO_2$, $CH_4$ and $CH_2O$, were not detected during the desorption experiment.

The corresponding P2p, C1s, and W4f XPS spectra for the oxidized surface before and after DMMP CTDS experiments are shown in Figures 6.3A, 6.4A, and 6.5A, respectively. A very strong P2p peak was observed at 133 eV, as shown in Figure 6.3A; a shoulder appeared at 285.6 eV in the C1s XPS spectrum as shown in Figure 6.4A; and dramatic changes were also observed in the W4f XPS spectrum with the doublet unresolved, as shown in Figure 6.6A.

The binding energy of the C1s peak in the methoxy group has been reported at 286.8 eV [35,91] and for $CH_n$ around 285 eV [179]. In view of the presence of phosphorous and low C1s binding energy of 285.6 eV, we ascribed the C1s peak to a P-$CH_3$ species, which has also been observed on $WO_3$ powders[81]. Infrared studies of DMMP decomposition on $WO_3$ powders showed that methyl phosphonate was left behind up to very high temperatures [81]. The intact P-$CH_3$ species also remained on the surface up to high temperature for decomposition of DMMP on aluminum oxide [80]. On the oxidized $WO_3$ surface, with successive exposure to DMMP and accumulation of phosphorous on the surface, the surface was finally poisoned so that the surface decomposition reaction was suppressed.

It is necessary to point out that previous studies showed that DMMP itself exhibits very high thermal stability.[180-182] A pyrolysis experiment with $N_2$ as the carrier gas indicated that destruction of DMMP happened on the stainless-steel wall to form CO, $CH_2O$ and $CH_4$ at 1023 K in a flow reactor, and that DMMP did not decompose in a quartz coated reactor.[182] During CTDS experiments, the $WO_3$ surface temperature was far below the temperature in the pyrolysis experiment, and furthermore, CO, $CH_2O$ and $CH_4$ were not detected. Therefore, all of the products observed are due to decomposition reactions of DMMP on the $WO_3$ surfaces. Further evidence is the surface structure dependence of the reaction products on the $WO_3$ surfaces.

### 6.2.4. Reaction selectivity and activity with DMMP on the $WO_3$(001) surfaces

The selectivity, or fractional distribution of products formed during the DMMP decomposition on $WO_3$ surfaces is displayed in Figure 6.7. We calculated the fraction of DMMP molecules that form each product by attributing one dimethyl ether to 2/3 of a DMMP molecule and production of a methanol to 1/3 of a DMMP molecule. The accumulated DMMP uptake on the surface, calculated from the absolute sensitivity factors for methanol, dimethyl ether, and DMMP and the stoichiometric factors, is plotted as the horizontal axis and the fractional distribution as the vertical axis. Figure 6.7A shows that on the oxidized $WO_3$ surface dimethyl ether is the dominant reaction product at the beginning of exposure to DMMP, however, with increasing exposure, the production of methanol occurs and increases as the dominant product. At approximately 0.4 ML uptake, the surface was poisoned and the surface decomposition reaction was quenched, as shown in Figure 6.7A.

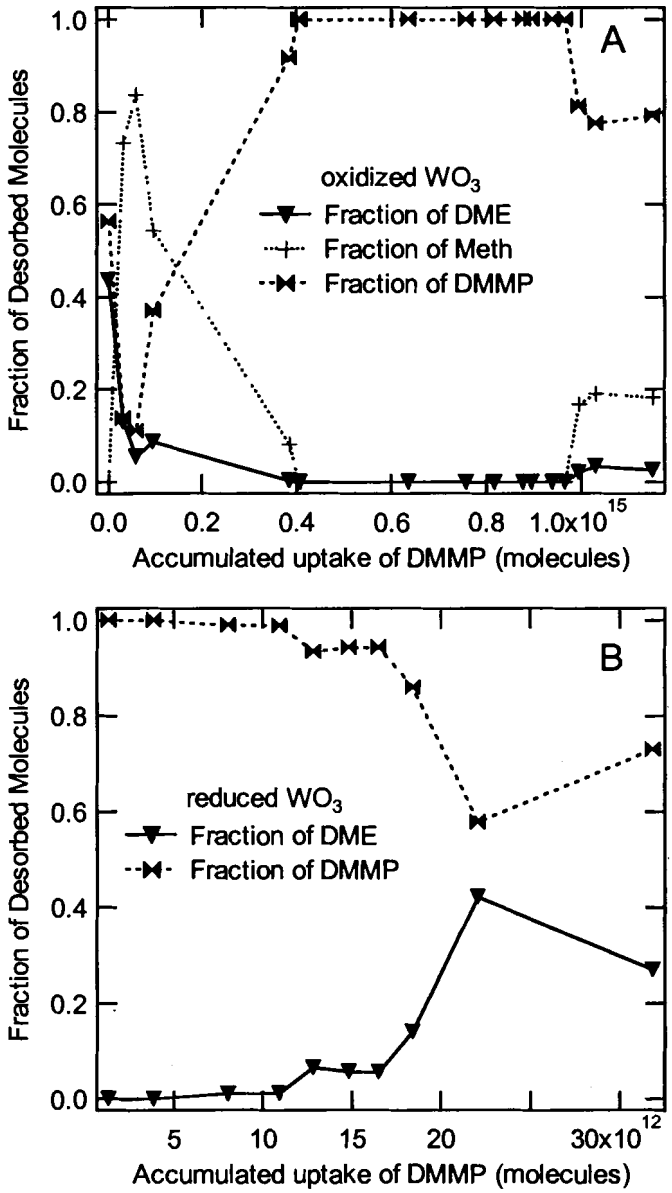


**Figure 6.7.** The product distribution as a function of cumulative DMMP exposure. A) On the oxidized $WO_3$(001) surface and B) on the reduced surface. A poisoning effect was observed on the oxidized surface; however, accumulation of phosphorous on the reduced surface promotes the production of DME.

The production of dimethyl ether increases with the uptake of DMMP on the reduced $WO_3$ surface. Although the decomposition reaction continued through our experiments shown in Figure 6.7B, the experiment was only carried out up to total DMMP uptake of 0.04 ML, which is much lower than shown in Figure 6.7A for the oxidized surface.

### 6.2.5. Methanol adsorption and desorption on the oxidized $WO_3$(001) surface

In order to understand the mechanism of production of methanol and dimethyl ether from decomposition of DMMP on the oxidized surface, methanol[154] and dimethyl ether[183] adsorption experiments were conducted on both the reduced and oxidized surfaces, and UPS was used to monitor the methanol adsorption state. UPS showed that methanol molecularly adsorbed on the oxidized surface; however, it adsorbed dissociatively on the reduced surface [154]. During the CTDS experiments, methanol was the only species detected on both surfaces. We compare the methanol spectra produced from DMMP decomposition with that following adsorption of methanol in Figure 6.8. On the oxidized surface, methanol desorbed (after methanol adsorption) around 360 K at a coverage of 0.03 ML (1ML=$10^{15}$ molecules/$cm^2$) and the desorption temperature decreased with increasing coverage, as shown in Figure 6.8A. On the reduced surface, methanol desorbed at higher temperatures compared to desorption on the oxidized surface [154].

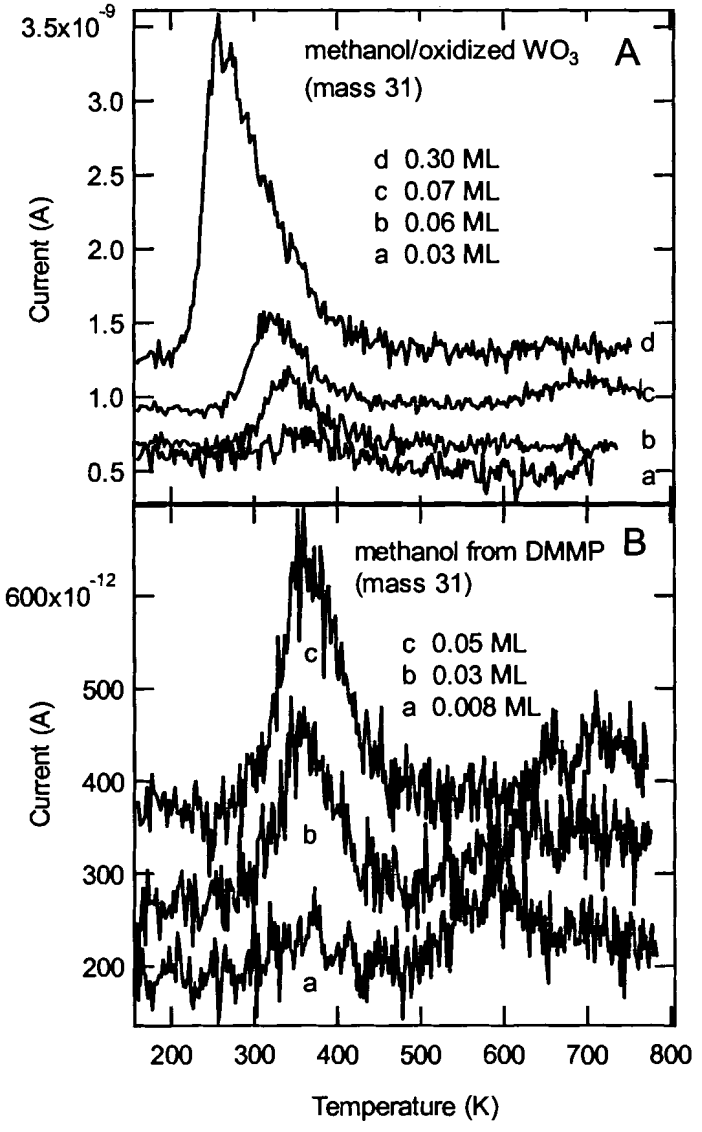


**Figure 6.8.** Comparison of methanol desorption on the oxidized $WO_3(001)$ surface following A) methanol adsorption and B) decomposition of DMMP.

A family of desorption spectra for methanol produced from DMMP decomposition on the oxidized surface is shown in Figure 6.8B. The methanol produced from DMMP desorbed at 360 K for a coverage of 0.03 ML. The desorption temperature during DMMP decomposition did not change with increasing production of methanol.

By comparison, we find that the desorption temperature for methanol evolved from DMMP decomposition is very close to the methanol desorption temperature in methanol CTDS experiment at lower coverage on the oxidized $WO_3$ surface. However, the change of desorption temperature from a coverage 0.03 ML to 0.06 ML is significant by over 15 K in methanol adsorption and desorption experiments. This implies that the production of methanol from DMMP is not desorption limited, but probably is a reaction controlled process.

### 6.2.6. Dimethyl ether adsorption and desorption on $WO_3$(001) surfaces

Dimethyl ether was the only species detected both on the oxidized and reduced surfaces during dimethyl ether CTDS experiments, shown in Figure 6.9A and Figure 6.10A, respectively. Dimethyl ether desorbed from 390 to 590 K in a very broad temperature range at a surface coverage of 0.004 ML on the reduced $WO_3$ surface. As the coverage increased, the desorption from 500 to 600 K did not change, suggesting that the stronger adsorption states were saturated at 0.004 ML. The desorption temperature decreases with increasing surface coverage as shown in Figure 6.9A. During the DMMP CTDS experiments on the reduced surface, the dimethyl ether generated desorbed at 350 K for a coverage of 0.001 ML and shifted only slightly to higher temperature at lower coverage, as shown in Figure 6.9B.

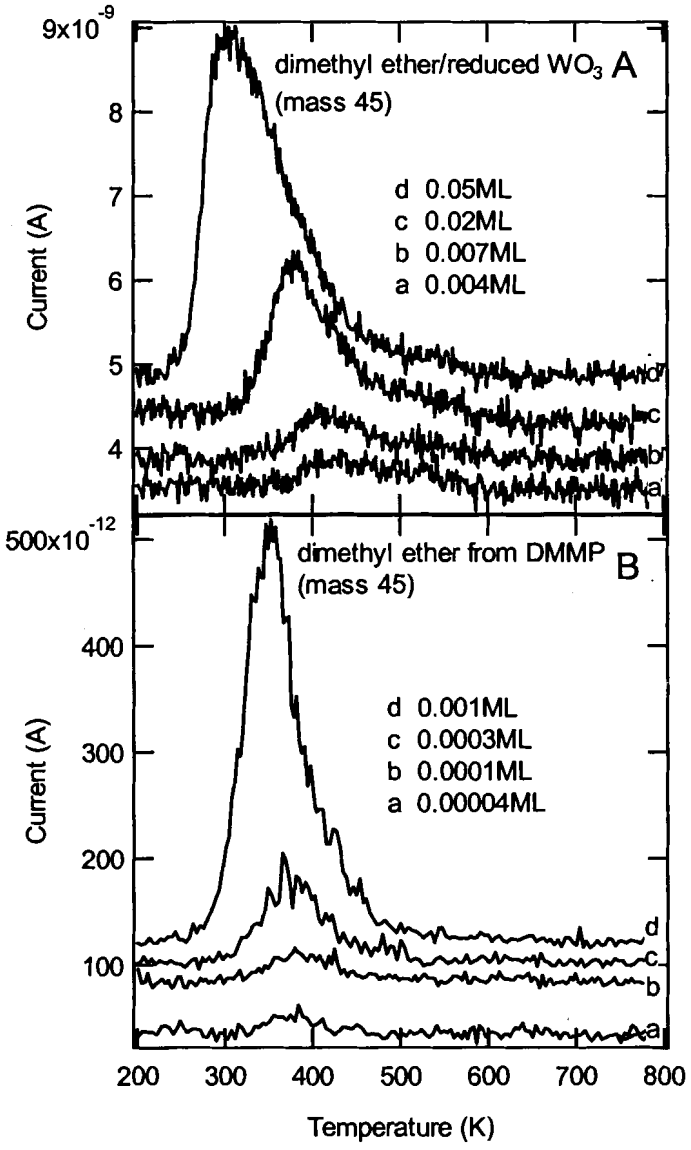


**Figure 6.9.** Comparison of dimethyl ether desorption on the reduced $WO_3(001)$ surface following A) dimethyl ether adsorption and B) decomposition of DMMP.

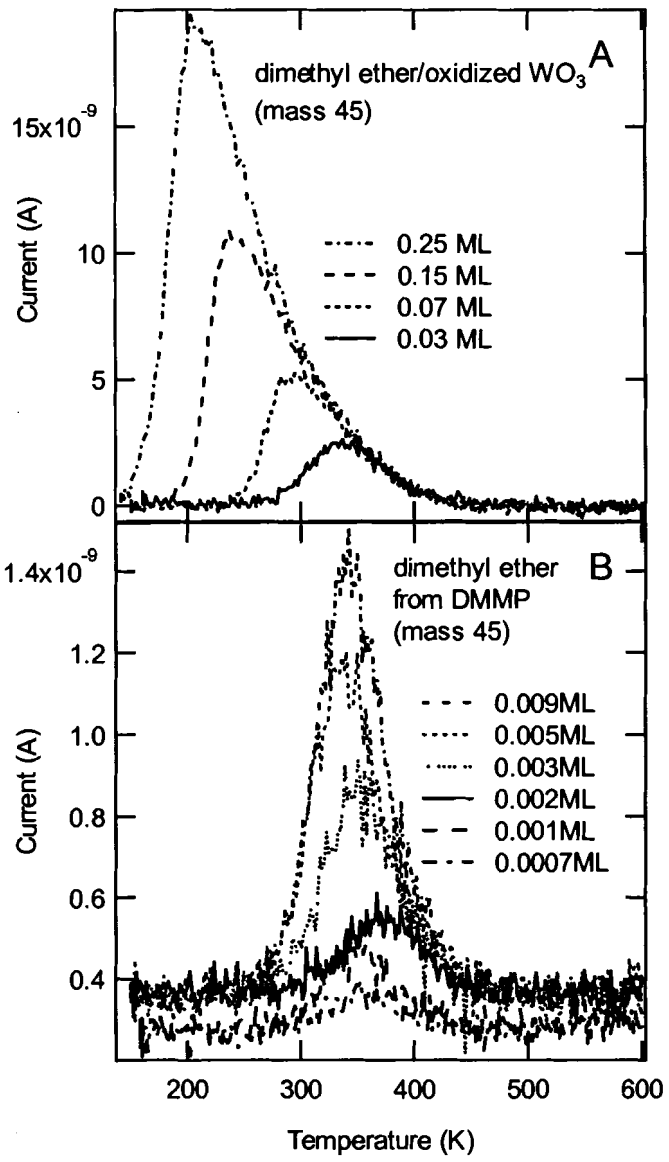


**Figure 6.10.** Comparison of dimethyl ether desorption on the oxidized $WO_3(001)$ surface following A) dimethyl ether adsorption and B) decomposition of DMMP.

On the oxidized $WO_3$ surface, dimethyl ether desorbed at 337 K for a coverage of 0.03 ML with the desorption temperature decreasing with increasing surface coverage as shown in Figure 6.10A. The dimethyl ether evolved during DMMP decomposition desorbed around 340 K for a coverage of 0.009 ML as shown in Figure 6.10B.
The surprising results are that desorption of dimethyl ether from DMMP decomposition occurred at lower temperature than in the dimethyl ether CTDS experiment, both on the reduced and oxidized $WO_3$(001) surfaces, but particularly dramatic on the reduced surface.

## 6.3. Discussion

### 6.3.1. Adsorption of DMMP on $WO_3$ surface

Previous studies have shown that DMMP adsorbs on metal oxide surfaces in several possible ways, depending upon the acid-base characteristics of the oxide surface. On $Al_2O_3$ surfaces, Templeton and Weinberg[80] first suggested that DMMP bonds to a coordinatively unsaturated surface Lewis acid cation site through the phosphoryl oxygen, as illustrated in Figure 6.11A. Similar conclusions have been reached by Mitchell *et al.*[74] for adsorption on aluminum, magnesium, and lanthanum oxides, by Rusu and Yates for the $TiO_2$ surface [76], by Segal *et al.* on manganese oxides [75] and by Kim and Tripp [81] for $WO_3$ surfaces. Evidence for interaction of the phosphoryl oxygen of DMMP with a surface hydroxyl group, as illustrated in Figure 6.11B, has also been given by Kim and Tripp [81] for $WO_3$ surfaces and by Rusu and Yates for the $TiO_2$ surface [76]. On the $WO_3$,

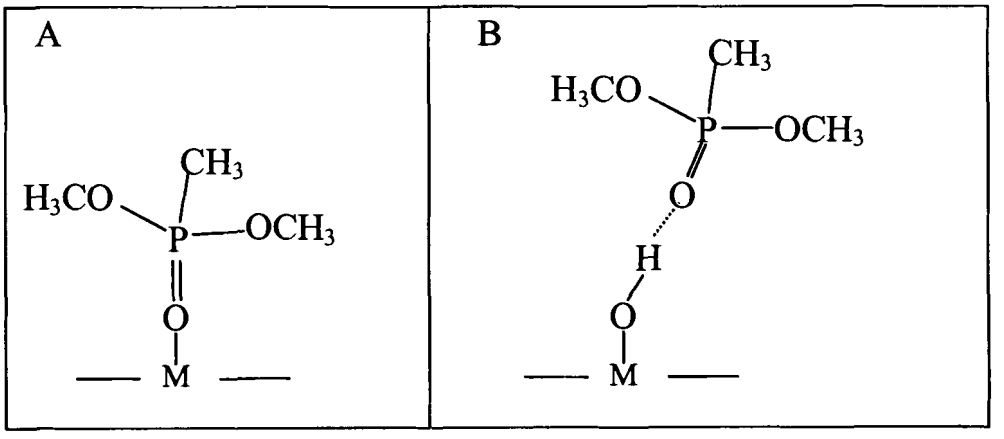


**Figure 6.11.** Adsorption states for different molecules and the dependence of the desorption temperatures on the oxidized ($T_{ox}$) and reduced ($T_{red}$) surfaces on molecular weight (MW), due to dispersion interactions. DMMP adsorbed on A) a Lewis acid (metal cation) site, B) a Brønsted acid site; C) adsorption of methanol, ethanol and isopropanol on Lewis acid sites; D) dimethyl ether adsorbed on a Lewis acid site; E) adsorption of dimethoxymethane through a single and two Lewis acid-base interactions; F) DMMP adsorption through two Lewis acid-base pairs and G) Intramolecular reaction for DMMP in adsorption state F to form DME.

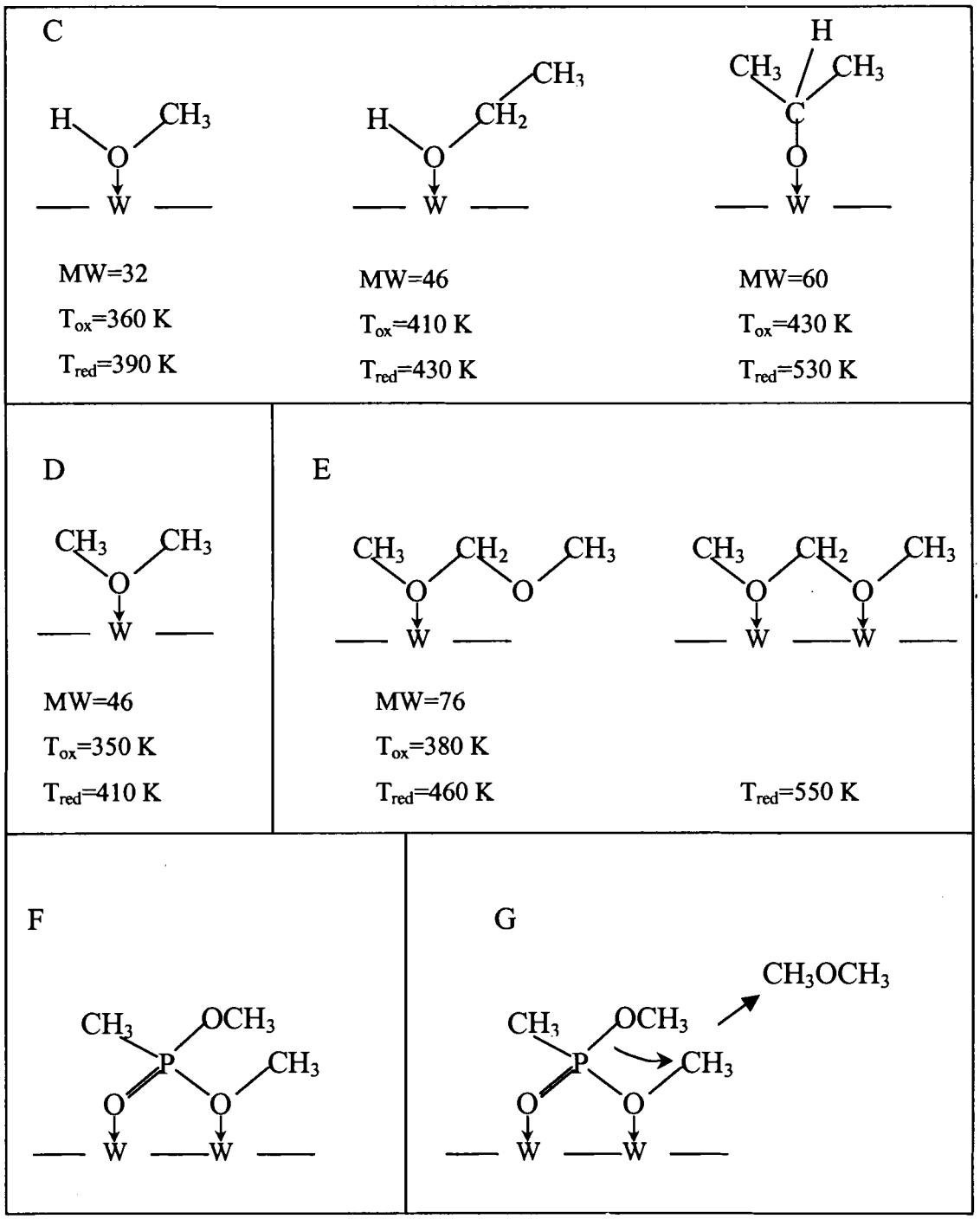


**Figure 6.11.** (Cont'd)

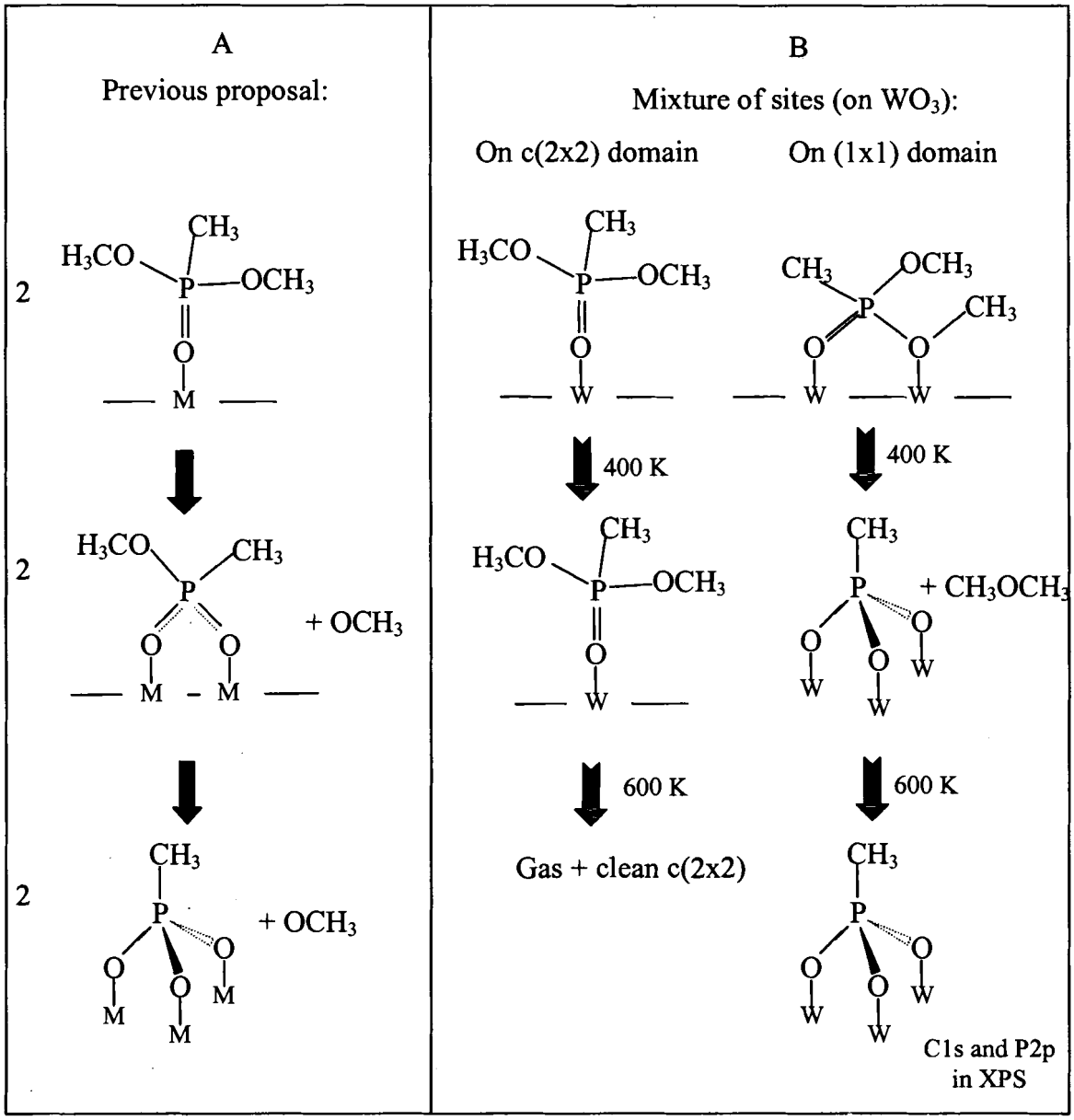


**Figure 6.12.** Comparison of A) the previously proposed DMMP decomposition pathways with B) two DMMP pathways on $WO_3$(001) surfaces having a mixture of sites. Note that from infrared data alone, A) and B) are difficult to distinguish.

the strong Lewis acidity of unsaturated tungsten cation sites has been identified by pyridine titration using infrared spectroscopy.[129]

Molecular desorption was found in thermal desorption experiments on $SiO_2$ from both a multilayer state at 204K and a chemisorbed state with a broad desorption peak near 275 K.[79] By contrast, on the $\alpha$-$Fe_2O_3$ surface, molecular desorption was only observed for multilayer desorption at low temperatures (near 200 K). [79] During our CTDS experiments with DMMP, no multilayer adsorption state was detected but monolayer desorption was observed at relatively high temperatures of 600-700 K on both the oxidized and reduced surfaces (Figures 6.2 and 6.6). The coverage dependence of the desorption temperature, which shifts to lower temperature with increasing surface coverage (shown in the Figure 6.6B) and has a common high temperature tail, was similar to the behavior of methanol. [154] Monte Carlo simulations show that this behavior occurs when diffusion is sufficiently rapid that adsorbates can find and desorb from the most strongly bound sites on a heterogeneous surface.

For comparison with the desorption temperature of DMMP on $WO_3$, we summarize the bonding of a series of alcohols[154,173] and ethers[183] and their corresponding zero-coverage limit desorption temperature in Figure 6.11C and D. We find that the desorption temperature is approximately 100 K higher on the reduced surface than the oxidized surface and increases with molecular weight as would be expected from dispersion forces. The evidence from UPS [154] supports the binding of methanol to a tungsten cation via an oxygen lone pair. The lone pairs on the ether molecules, dimethyl ether and dimethoxy methane are available for a similar adsorption process. The variation of the desorption temperature with molecular weight for the entire series of

alcohols and ethers seems consistent with the geometry shown. Given the larger molecular weight of DMMP compared to the alcohols and ethers, adsorption at a Lewis acid site through a single lone pair interaction appears consistent. We tentatively correlate the high temperature desorption peak to DMMP adsorbed on the c(2×2) terrace sites with adsorption through a single phosphoryl oxygen.

We also note that dimethoxymethane has a second, more strongly bound molecular adsorption state on the reduced surface, which we have suggested may be associated with bonding through the oxygen lone pairs on both ether oxygens, as shown in Figure 6.11 E. Such an adsorption geometry requires a closer W-W distance than is possible in the $WO_3$ c(2x2) surface, but if crystallographic shear planes emerge at the surface, shorter 2.6Å distances would be possible. A similar adsorption geometry may be possible for DMMP on the reduced surface, involving lone pairs on the phosphoryl oxygen and one of the methoxy oxygens, as suggested in Figure 6.11F.

### 6.3.2. Decomposition mechanism of DMMP on $WO_3$ surfaces

The intermediates in the decomposition of DMMP have been studied with vibrational spectroscopy on a number of metal oxides, however there is very little overlap between the thermal desorption and vibrational spectroscopy data. In the study on $Al_2O_3$ by Templeton and Weinberg, [80] and later in the studies on $Al_2O_3$, MgO and $La_2O_3$[74] and on $TiO_2$,[76] the vibrational spectra have been interpreted by the mechanism shown in Figure 6.12A. The tacit assumption is that all molecules behave similarly and DMMP first loses one methoxy group, resulting in methyl methylphosphonate as the surface was heated to temperatures of 400-500K. At higher temperatures, loss of the second methoxy

occurs. The –P-$CH_3$ moiety was left on the surface to much higher temperatures. The suggestion is that methoxy intermediates combine with surface hydroxyls to produce methanol. [74] Indeed, Rusu, et al. [76] identify methoxy intermediates on the $TiO_2$ surface, and Mitchell, et al. [74] observe loss of surface hydroxyls. However, we are not aware of any direct evidence regarding the species evolved from gas phase monitoring of the product distribution on the $Al_2O_3$, MgO, $La_2O_3$, or $TiO_2$ surfaces. On the $\alpha$-$Fe_2O_3$ surface, Henderson et al. [79] found desorption of CO, $CO_2$, $H_2$, methanol and formic acid around 600 K.

The decomposition products, dimethyl ether and methanol on the oxidized $WO_3$ surface and dimethyl ether on the reduced $WO_3$ surface, in our CTDS experiments implies loss of methoxy groups from DMMP in the 300-400 K range. However, the desorption of molecular DMMP at higher temperatures is not consistent with the mechanism of Figure 6.12A. The associative desorption of methoxy species to form DMMP seems unlikely, and instead we suggest that on the $WO_3$ surface there at least two different decomposition processes. The molecules that desorb at 600 K, which we suggest may be bound to a Lewis acid site via a single oxygen lone pair interaction, would be observed in FTIR studies, such as the one by Kim and Tripp,[81] until the desorption temperature is reached. Other DMMP molecules, which may be adsorbed on more reduced $WO_3$ surfaces, decompose to form dimethyl ether and, on the oxidized surface, a mixture of dimethyl ether and methanol. We propose that the decomposition of DMMP to produce dimethyl ether occurs essentially as an intramolecular decomposition reaction, rather than formation of surface methoxy intermediates that couple to produce dimethyl ether for several reasons.

We first point out that the apparent "stepwise elimination" of the methoxy groups (Figure 6.12A) proposed for the $Al_2O_3$, MgO, $La_2O_3$, $TiO_2$ and $WO_3$ surfaces cannot easily be distinguished from the alternate scheme suggested in Figure 6.12B. If roughly half of the molecules are adsorbed in each state, then the mixture of intact DMMP and methyl phosphate species remaining after the low temperature desorption is complete will have a similar absorption spectrum as methyl methylphosphonate. On $WO_3$ powders, the methoxy group absorption bands decrease in intensity by approximately half at temperatures above 473 K, which is consistent with both mechanisms and the temperature at which decomposition is complete in our CTDS data. The remaining intensity in the methoxy group absorption bands on the powder $WO_3$ disappeared above 673 K, which correlates well with our DMMP desorption peak, considering the differences in conditions of the UHV and HV systems and potential differences between thin film and powder materials. After the high temperature DMMP molecular desorption is complete, the C1s binding energy of the product in our work is consistent with the methyl phosphate species identified by Kim and Tripp.[81]

Comparison of the CTDS data of dimethyl ether desorption from the $WO_3$ surfaces following dimethyl ether adsorption with that during DMMP decomposition shows that these processes are significantly different. Desorption of dimethyl ether during DMMP decomposition at temperatures *below* the temperature observed from dimethyl ether is surprising. Our Monte Carlo simulations suggest that diffusion is relatively rapid compared to desorption and so we would not expect dimethyl ether to desorb at lower temperatures if methoxy intermediates couple on the surface before desorbing. In a second order, surface mediated coupling reaction, the desorption rate

would be limited by the statistical probability of the methoxy intermediates colliding with each other, whereas in an intramolecular coupling reaction, the process likely would be a pseudo-first order process. Notice that in the decomposition reaction, the desorption temperature is relatively constant, which also suggests that the relevant activation energy barrier is an intramolecular bond breaking process. Furthermore, our methanol study showed that, although methoxy intermediates were the majority species on the reduced surface, no coupling to dimethyl ether was observed. On the $TiO_2$(001) surface, Kim and Barteau[35] has suggested that coupling of methoxy to dimethyl ether requires closely spaced metal cations, which may be a factor on the relatively open $WO_3$ surface. However, as we have discussed,[173] the presence of hydroxyl groups may be a more important reason that no dimethyl ether is produced following dissociative methanol adsorption on the reduced $WO_3$ surface: the rate of associative desorption of molecular methanol is fast compared to the rate of recombinative desorption of surface hydroxyls to form water.

We now turn to the role of the surface for production of dimethyl ether. In gas phase pyrolysis experiment in a pure $N_2$ carrier gas, DMMP is very robust, decomposing only above 1100 K when a quart tube was used in the reactor, while surface reactions led to decomposition at much lower temperatures when a stainless steel tube was used. [182] Several suggestions regarding surface reactions have been put forward. Templeton and Weinberg [80] suggested that a nucleophilic lattice oxygen attacks the phosphorous atom, resulting in breaking the P-$OCH_3$ bond to form a methoxy intermediate. Li and Klabunde [78] proposed a mechanism involving the interaction between a surface methoxy group and an adsorbed DMMP molecule in explaining the formation of formic acid in their study of

the decomposition of DMMP on nanoscale MgO particles. Henderson et al. [79] found that coadsorption of water with DMMP on the oxidized iron surface significantly enhanced the production of methanol during DMMP decomposition.

We suggest that the more strongly bound DMMP molecules are adsorbed through more than one oxygen, as illustrated in Figure 6.11F. These molecules may undergo an intramolecular rearrangement to produce dimethyl ether, leaving one methoxy oxygen on the surface to form a phosphate-like species, as illustrated in Figure 6.12 G. The reduced surface only produces dimethyl ether, which is consistent with the ability of crystallographic shear plane structures in $WO_3$ to easily absorb or release oxygen during selective oxidation reactions.

On the oxidized surface, we observe both methanol and dimethyl ether during DMMP decomposition. As we have noted, there is some background water adsorption due to the high pressure (0.2 mbar) oxidation treatment of the oxidized surface. This suggests that hydroxyl groups are present, which leads to methanol, in addition to dimethyl ether. Again, the desorption temperature is below that expected for methanol desorption, which suggests an interaction of surface hydroxyls with the strongly bound DMMP molecules.

The role of surface hydroxyl groups in formation of methanol has been identified in previous studies. In the interaction of DMMP with $SiO_2$, DMMP decomposition was only observed on the hydrated surface, resulting in methanol production.[79] On the iron oxide surface, coadsorption of water with DMMP significantly enhanced the production of methanol during decomposition of DMMP. Finally, in an infrared study of the

decomposition of DMMP on $Al_2O_3$, in which methanol was observed, surface hydroxyl groups disappeared after $Al_2O_3$ was exposed to DMMP at high temperature.[75]

### 6.3.3. Reaction selectivity and influence of accumulated phosphorus

The reaction selectivity to methanol and dimethyl ether on the oxidized surface is shown the Figure 6.7A. Initially, dimethyl ether was the dominant product. As the surface was exposed to DMMP, methanol production became large compared to the production of dimethyl ether. With accumulation of phosphorous, the surface reactivity decreased until the surface was finally poisoned. The production of methanol and dimethyl ether on $WO_3$ surfaces is similar to the results reported for DMMP decomposition on $Al_2O_3$ surfaces. Methanol and dimethyl ether were found to be the only surface reaction products during decomposition of DMMP on $Al_2O_3$ surfaces below 673 K.[72,75] Furthermore, Sheinker and Mitchell [72] found that dimethyl ether was always produced prior to production of methanol and that as the temperature increased, the initial production of dimethyl ether increased. However, with the surface exposed to DMMP, methanol production dominates over production of dimethyl ether. On the reduced surface, dimethyl ether production increased with DMMP exposure. A similar effect was observed by Ai [82] in his study of the oxidation of methanol on $P_2O_5$ doped $WO_3$, in which production of dimethyl ether was enhanced.

The phosphorous accumulation on the $WO_3$ surface has been exploited in our lab as a selective poison effect for development of an organophosphorus selective $WO_3$ based sensor element.[33] The conditions under which poison occurs appears to be sensitive to the surface oxidation state, which may be related to the two different processes suggested

in Figure 6.12. Henderson, *et al.*[79] found that the DMMP decomposition reaction on $\alpha$-$Fe_2O_3$ surface could not be sustained due to the accumulation of phosphorous on the surface.

# SUMMARY AND FUTURE WORK

## 7.1. Summary of the current research work

Our motivation was to understand the decomposition mechanism of dimethyl methylphosphonate (DMMP), a simulant for chemical warfare agents and pesticides, on the $WO_3$ thin film surface, which is being developed for potential use as a sensor element. We investigated the adsorption, desorption, and surface reactions of both DMMP and several related compounds, including alcohols, ethers and water on $WO_3(001)$ surfaces using calibrated thermal desorption spectroscopy (CTDS). The $WO_3$ films were grown epitaxially on an $\alpha$-$Al_2O_3$ substrate. Two surfaces were created for the studies: a "reduced" surface that was generated by $Ar^+$ sputtering and an "oxidized" surface that was produced by oxidizing the reduced surface in oxygen at high temperatures and relatively high pressure. X-ray photoelectron spectroscopy (XPS) and ultra-violet photoelectron spectroscopy (UPS) were used to characterize both surfaces by monitoring the W4f and valence band regions. Based on the final state model, which is very successful in explaining the W4f XPS spectra for $Na_xWO_3$ surfaces, we concluded that the reduced surface contains a mixture of $W^{6+}$ and $W^{5+}$ species. The research work for each adsorbate is summarized as follows:

### 7.1.1. Methanol interaction with the $WO_3(001)$ surfaces

In this study, UPS was used to monitor the adsorption state of methanol on the reduced and oxidized $WO_3(001)$ surfaces and CTDS was used to detect desorbing species. Monte Carlo simulations of the first order desorption with a controlled diffusion vs. desorption rate were conducted to understand the nature of the experimental

desorption spectra. On the oxidized surface, UPS shows that methanol bonds molecularly to Lewis acid sites, while on the reduced surface, stronger Brønsted base sites lead to dissociative adsorption. The coverage dependent desorption of methanol shows strong shifts to lower temperature, similar to behavior of water and other alcohols on oxide surfaces. Monte Carlo simulations allow the relative importance of diffusion and desorption to be assessed from coverage dependent spectra. Qualitatively different behavior is also found for the effects of a heterogeneous surface and intermolecular interactions, for both the cases of slow and rapid diffusion. On $WO_3(001)$, diffusion of molecular methanol is relatively rapid. The structural constraints of the large tungsten-oxygen-tungsten cation distances appear to prevent significant hydrogen bonding between adsorbed methanol molecules. Thus, the coverage dependence of the desorption spectra is attributed to the heterogeneity of the adsorbate-surface interaction. Methanol was the only species detected during experiments. Formaldehyde and dimethyl ether, which are produced following methanol adsorption on the $TiO_2(001)$ surface, were not observed on either the oxidized surface or the reduced surface, on which methanol dissociates.

### 7.1.2. Aliphatic alcohol reactions on the $WO_3(001)$ surfaces

Reactions of alcohols on the reduced and oxidized $WO_3(001)$ surfaces were conducted at much lower coverages than in previous studies. Alcohols were removed from the surfaces through two channels: i) low temperature desorption of alcohol with desorption spectra that indicate a broad distribution of adsorption site energies and diffusion rates that are sufficiently rapid for the alcohol to find and desorb from the most

strongly bound sites; and ii) dehydration to form an alkene, which desorbs at higher temperature together with desorption of water. Desorption of the alkene is a reaction controlled process and the rate-limiting step for dehydration of ethanol, and probably for isopropanol, is C-O bond scission. The reduced and oxidized $WO_3(001)$ surfaces do not have significant differences in their selectivity toward dehydration of the alcohols to alkenes. The coverage dependence of the selectivity was attributed to the role of diffusion and reaction kinetics under the low coverage conditions, which contrasts with the defect controlled dehydration of alcohols on the $TiO_2(110)$[155] and $TiO_2(001)$[84] surfaces.

### 7.1.3. Ether interaction with the $WO_3(001)$ surfaces

Adsorption and desorption of dimethyl ether (DME) and dimethoxymethane (DMM) were performed on the reduced and oxidized $WO_3(001)$ surfaces with calibrated thermal desorption spectroscopy. DME molecularly adsorbs and desorbs on both the reduced and oxidized surfaces without decomposition products being detected. For DMM adsorption, two molecular desorption peaks were observed and a reaction controlled desorption of methanol, formed from decomposition of DMM, was identified. Based on the comparison of desorption peak temperatures of ethers and alcohols, the low temperature peak was attributed to DMM interacting with a single tungsten cation through oxygen lone pair electrons. The higher temperature peak that appears only on the reduced surface was assigned to DMM interacting with two tungsten cations through both ether oxygens, perhaps in regions associated with crystallographic shear structure

domains. The possible role of DMM as a probe molecule in studying closely spaced metal cation sites, on the $WO_3$ surface and other oxides, is noted.

### 7.1.4. Decomposition of DMMP on $WO_3$(001) surfaces

Adsorption and decomposition of dimethyl methylphosphonate (DMMP) on the reduced and oxidized $WO_3$(001) surfaces were conducted using calibrated thermal desorption spectroscopy (CTDS). Multilayer desorption of DMMP was not detected on either surface, while the monolayer desorption, attributed to molecularly adsorbed DMMP species, was observed around 600 K. The desorption temperature of chemisorbed DMMP appears to be consistent with the dependence on molecular weight of the desorption temperatures of alcohols and ethers studied on these surfaces. On the oxidized $WO_3$(001) surface, dimethyl ether and methanol were produced during decomposition of DMMP; however, on the reduced surface, only dimethyl ether was observed. The desorption of DMMP decomposition products shows that DMMP decomposed below 450 K on the $WO_3$(001) surfaces.

We associate the lower temperature decomposition of DMMP to dimethyl ether to adsorption on more strongly bound sites, which have been identified in the study of dimethoxymethane adsorption on the reduced surface. These surface sites may be related to emergence of crystallographic shear (CS) planes at the surface, in which the spacing between Lewis acid sites is expected to be reduced compared to the majority 5-fold $W^{6+}$ sites. We suggest that adsorption occurs through two Lewis acid-base interactions between adsorbate and adsorbent.

Dimethyl ether and methanol, produced from decomposition of DMMP, desorbed at lower temperatures compared to the desorption temperature following adsorption of dimethyl ether or methanol, respectively. Given the behavior of methanol on both the reduced and oxidized surfaces, on which dimethyl ether was not detected, even on the reduced surface where methanol adsorbs dissociatively, production of dimethyl ether was suggested to be most likely to occur through an intramolecular coupling reaction. The production of methanol was determined by the availability of surface hydroxyls during the decomposition process. P-$CH_3$ species are identified in XPS on both the reduced surface and oxidized surface after decomposition of DMMP. Accumulation of phosphorus resulted in poisoning of the surface reaction. The surface processes of DMMP on the $WO_3(001)$ surfaces suggested in this study may be consistent with previous infrared observations in the study of DMMP adsorption on $WO_3$ powders [81]; however, our mechanism differs from the widely accepted decomposition mechanism on the $Al_2O_3$ surface and some other oxide surfaces. Thermal desorption studies on the powder materials and vibrational studies on our thin film surfaces are needed to resolve the difference in interpretation.

### 7.2. Future work

After the research work performed in this thesis, some work still needs to be conducted in order to further understand the differences of the oxidized and reduced surfaces in their surface reactivity. Identifying the surface states on the reduced $WO_3(001)$ surface vs. oxidized surface with vibrational spectroscopy is necessary; further

experiments are required to confirm the proposed DMMP decomposition reaction pathway.

### 7.2.1. Identify surface tungsten states and structure on the reduced surface vs. the oxidized surface

XPS shows that treatment of the $WO_3$ surface by sputtering or annealing results in growth of new bands on the low binding energy side in W4f spectra, depending on the extent of the surface treatment. Two models are proposed to interpret the complicated W4f spectra, as mentioned in this thesis, the initial state and final state models. The fact that both models behave equally well in fitting W4f spectra makes very hard identifying one from the other.

It is well known that the surface physicochemical processes are closely associated with the surface structure, for instance the important role of oxygen vacancies in oxide surfaces have been recognized for surface reaction specificity and the properties of oxides. In order to understand the difference in the activity of the reduced surface vs. the oxidized surface toward dissociative adsorption of methanol and selectivity in the DMMP decomposition reaction, identifying the surface species on the reduced surface vs. oxidized surface would be necessary and required. Auger may be a useful technique in identifying different oxidation states of tungsten species by monitoring the Auger parameter.

Our surface structures for the reduced and oxidized $WO_3$ surface were tentatively identified based on the comparison with the observations by Dixon, *et al.* in their XPS, UPS and STM study of a single crystal $WO_3(001)$ surface. A STM study, at atomic

resolution, of the reduced surface and oxidized surface of $WO_3$ epitaxial films would be very useful in identifying the difference in the their structures.

### 7.2.2. Further experiments to identify DMMP decomposition mechanism

Previous study of adsorption of DMMP on oxide surfaces shows that decomposition of DMMP requires the presence of surface hydroxyl groups, such as on the $SiO_2$ surface. In our study, selectivity toward decomposition of DMMP to methanol clearly shows surface structure dependence. Compared to the oxidized surface, a majority of surface oxygen on the reduced surface are removed during sputtering $WO_3$, implying the reduction of the surface hydroxyl coverage on the reduced surface. In this case, the structure dependence of selectivity toward methanol for DMMP decomposition can be understood in terms of the availability of surface hydroxyls during the decomposition reaction. Coadsorption of water with DMMP on the reduced surface will help to verify this reaction pathway by monitoring the product distribution versus the adsorbed water and DMMP. HREELS experiments would be the best means of monitoring the surface hydroxyl coverage on the thin film.

The coverage dependence of DMMP desorption spectra on $WO_3$ surfaces and the overlapping tail, as shown in Figure 6.6B, similar to desorption of methanol on these surfaces, implies that the desorption of DMMP can be characterized by surface heterogeneity and relatively rapid diffusion. Based on the relationship between desorption temperatures and molecular weight suggested in our studies, the adsorption state responsible for the DMMP molecular desorption around 600 K are not necessarily the highest binding energy sites. In contrast, DMMP adsorbed on the stronger binding

energy sites may be most likely to experience decomposition to form methanol and dimethyl ether. An experiment with pre-adsorption of methanol might be conducted to block the strong binding sites before DMMP exposure due to the mobility of methanol as suggested in the study of methanol adsorption. Therefore, such a study may be helpful to elucidate how decomposition of DMMP is related to surface structure. By comparing the product distribution under the conditions with and without pre- or co-adsorption of methanol on the reduced surface, on which methanol dissociates, the reaction mechanism of decomposition of DMMP to form dimethyl ether may be clarified, since if formation of dimethyl ether is not an intramolecular reaction as suggested in our study, the coverage dependence of dimethyl ether production on a surface with adsorbed methoxy groups may be more like adsorption of dimethyl ether.

Two adsorption states are proposed corresponding to desorption of molecular DMMP around 600 K and decomposition of DMMP at below 450 K on the $WO_3(001)$ thin film surface. A STM study of adsorption of DMMP will be helpful in identifying the correlation between the sites and DMMP decomposition.

## BIBLIOGRAPHY


(1) Wilk, G. D.; Wallace, R. M.; Anthony, J. M. *J. Applied Phys.* **2001**, *89*, 5243.

(2) Bielanski, A.; Haber, J. *Oxygen in Catalysis*; Marcel Dekker, Inc.: New York, 1991.

(3) Zhou, B.; Chuang, K. T.; Guo, X. *J. Chem. Soc. Faraday Trans.* **1991**, *87*, 3695-3702.

(4) Taylor, S. H.; Hargreaves, J. S. J.; Hutchings, G. J.; Joyner, R. W. *Applied Catalysis A* **1995**, *General 126*, 287-296.

(5) Burrington, J. D.; Kartisek, C. T.; Grasselli, R. K. *J. Cat.* **1980**, *63*, 235-254.

(6) Chiba, A. *Development of the Taguchi gas sensor*; Kodansha: Tokyo, 1992; Vol. 4.

(7) Taguchi, N.; U.S. Patent, 1971.

(8) *Fundamental and applications of chemical sensors*; Seivama, T.; Yamazoe, N., Eds.; American chemical society: Washington, D.C., 1986; Vol. 309, pp 39.

(9) Shimizu, Y.; Egashira, M. *MRS Bulletin* **1999**, *24*, 18.

(10) Heiland, G. *Sens. Actuators* **1982**, *2*, 343-361.

(11) Kohl, D. *Sens. Actuators* **1989**, *18*, 71-113.

(12) Barbi, G. B.; Blanco, J. S. *Sens. Actuators B* **1993**, *15-16*, 372.

(13) Santos, J.; Serrini, P.; O'Beirn, B.; Manes, L. *Sens. Actuators B* **1997**, *43*, 154-160.

(14) Gopel, W.; Schierbaum, K. D. *Sens. Actuators B* **1995**, *26-27*, 1-12.

(15) Meixner, H.; Lampe, U. *Sens. Actuators B* **1996**, *33*, 198-202.

(16) http://www.microsens.ch/products.

(17) Morrison, S. R. *Sens. Actuators* **1982**, *2*, 329-341.

(18) Nelli, P.; Depero, L. E.; Ferroni, M.; Groppelli, S.; Guidi, V.; Runomi, F.; Sangaletti, L.; Sberveglieri, G. *Sens. Actuators B* **1996**, *31*, 89.

(19) Williams, G.; Coles, G. S. V. *MRS Bulletin* **1999**, *24*, 25.

(20) Martinelli, G.; Carotta, M. C.; Traversa, E.; Ghiotti, G. *MRS Bulletin* **1999**, *24*, 30.

(21) Choi, Y.; Sakai, G.; Shimanoe, K.; Teraoka, Y.; Miura, N.; Yamazoe, N. *Sens. Actuators B* **2003**, *in press*.

(22) Martin, A.; Frederick, B. G. *sensor research work.*

(23) Sberveglieri, G.; Depero, L.; Gropelli, S.; Nelli, P. *Sens. Actuators B* **1995**, *26-27*, 89.

(24) Cantalini, C.; Sun, H. T.; Faccio, M.; Pelino, M.; Santucci, S.; Lozzi, L.; Passacantando, M. *Sens. Actuators B* **1996**, *31*, 81-87, and references therein.

(25) Chu, C. W.; Deen, M. J.; Hill, R. H. *J. Electrochem. Soc.* **1998**, *145*, 4219.

(26) Solis, J. L.; Saukko, S.; Kish, L.; Granqvist, C. G.; Lantto, V. *Thin Solid Films* **2001**, *391*, 255-260.

(27) Lozzi, L.; Ottaviano, L.; Passacantando, M.; Santucci, S.; Cantalini, C. *Thin Solid Films* **2001**, *391*, 224-228.

(28) Lunsford, J. H. ESR of adsorbed oxygen species. In *Catalysis Reviews*; Heinemann, H., Ed.; New York, Marcel Dekker, Inc.: New York, 1973; Vol. 8; pp 135-157.

(29) Che, M.; Tench, A. J. Characterization and reactivity of molecular oxygen species on oxide surfaces. In *Advances in Catalysis*; Academic Press: New York, 1983; Vol. 32; pp 1-147.

(30) Winter, E. R. S. *J. Chem. Soc. (A), Inorg. Phys. Theor.* **1968**, 2889-2902.

(31) LeGore, L. J. Microstructure, kinetics and diffusion in tungsten trioxide thin film sensors. Ph.D., University of Maine, 2000.

(32) Ren, H. Current voltage characteristics of a semiconductor metal oxide sensor. M.S., University of Maine, 2001.

(33) Madi, A. E.; Meulendyk, B.; Pilling, R. S.; Bernhardt, G.; Lad, R. J.; Frederick, B. G. *Mat. Res. Sci.* **2003**, *in press*.

(34) Campbell, C. T. *Surf. Sci. Reports* **1997**, *27*, 1-111.

(35) Kim, K. S.; Barteau, M. A. *Surf. Sci.* **1989**, *223*, 13-32.

(36) Dixon, R. A.; Egdell, R. G. *Surf. Sci.* **2000**, *452*, 207-219.

(37) Ernst, K. H.; Ludviksson, A.; Zhang, R.; Yoshihara, J.; Campbell, C. T. *Phys. Rev. B* **1993**, *47*, 13782.

(38) Reddic, J. E.; Zhou, J.; Chen, D. A. *Surf. Sci.* **2001**, *494*, L767-772.

(39) Frederick, B. G.; Apai, G.; Rhodin, T. N. *J. Am. Chem. Soc.* **1987**, *109*, 4797-4804.

(40) Cox, P. A. *The electronic structure and chemistry of solids*; Oxford University Press: Oxford, 1987.

(41) Henrich, V. E.; Cox, P. A. *The surface science of metal oxides*; Cambridge University Press:, 1994.

(42) O'Grady, W. E.; Atanasoska, L.; Pollak, F. H.; Park, H. L. *J. Electroanal. Chem.* **1984**, *178*, 61-68.

(43) Atanasoska, L.; O'Grady, W. E.; Atanasoski, R. T.; Pollak, F. H. *Surf. Sci.* **1988**, *202*, 142-166.

(44) Tasker, P. W. *J. Phys. C, Solid State Phys.* **1979**, *12*, 4977.

(45) Imaduddin, S.; Lad, R. J. *Surf. Sci.* **1993**, *290*, 35-44.

(46) Lad, R. J.; Antonik, M. D. *Ceramic Transactions* **1991**, *24*, 359.

(47) Tanner, R. E.; Meethunkij, P.; Altman, E. I. *J. Phys. Chem. B* **2000**, *104*, 12315-12323.

(48) Tanner, R. E.; Altman, E. J. *J. Vac. Sci. Technol. Part A: Vacuum, Surfaces and Films* **2001**, *19*, 1502-1509.

(49) Salje, E. K. H. Polarons and bipolarons in WO3-x and YBa2Cu3O7. In *Polarons and Bipolarons in High-Tc Superconductors and Related Materials*; Salje, E. K. H., Alexandrov, A. S., Liang, W. V., Eds.; Cambridge University Press: Cambridge, 1995.

(50) Dixon, R. A.; Williams, J. J.; Morris, D.; Rebane, J.; Jones, F. H.; Egdell, R. G.; Downes, S. W. *Surf. Sci.* **1998**, *399*, 199-211.

(51) Campagna, M.; Wertheim, G. K.; Shanks, H. R.; Zumsteg, F.; Banks, E. *Phys. Rev. Lett.* **1975**, *34*, 738.

(52) Wertheim, G. K. *Chem. Phys. Lett.* **1979**, *65*, 377.

(53) LeGore, L. J.; Lad, R. J.; Moulzolf, S. C.; Vetelino, J. F.; Frederick, B. G.; Kenik, E. A. *Thin Solid Films* **2002**, *406*, 79-86.

(54) Cora, F.; Stachiotti, M. G.; Catlow, C. R. A.; Rodriguez, C. O. *J. Phys. Chem. B* **1997**, *101*, 3945-3952.

(55) Owen, J. F.; Teegarden, K. J.; Shanks, H. R. *Phys. Rev. B* **1978**, *18*, 3827.

(56) Jones, F. H.; Rawlings, K.; Dixon, R. A.; Fishlock, T. W.; Egdell, R. G. *Surf. Sci.* **2000**, *460*, 277-291.

(57) Brown, B. W.; Banks, E. *Phys. Rev.* **1951**, *84*, 609.

(58) Muhlestein, L. D.; Danielson, G. C. *Phys. Rev.* **1967**, *158*, 825.

(59) Deb, S. K. *Philos. Mag.* **1973**, *27*, 801-822.

(60) Colton, R. J.; Guzman, A. M.; Rabalais, J. W. *J. Applied Phys.* **1978**, *49*, 409.

(61) Granqvist, C. G. *Appl. Phys. A* **1993**, *57*, 19-24.

(62) Firment, L. E.; Ferretti, A. *Surf. Sci.* **1983**, *129*, 155-176.

(63) Tilley, R. J. D. *Defect crystal chemistry and its applications*; Blackie: Glasgow, 1987.

(64) Bursill, L. A.; Hyde, B. G. *J. Solid State Chem.* **1972**, *4*, 430-446.

(65) Booth, J.; Ekstrom, T.; Iguchi, E.; Tilley, R. J. D. *J. Solid State Chem.* **1982**, *41*, 293-307.

(66) Moulzolf, S. C.; Ding, S. A.; Lad, R. J. *Sens. Actuators B* **2001**, *77*, 375-382.

(67) Moulzolf, S. C.; LeGore, L. J.; Lad, R. J. *Thin Solid Films* **2001**, *400*, 56-63.

(68) LeGore, L. J.; Greenwood, O. D.; Paulus, J. W.; Frankel, D. J.; Lad, R. J. *J. Vac. Sci. Technol.* **1997**, *A15*, 1223-1227.

(69) Fruhberger, B.; Grunze, M.; Dwyer, D. J. *Sens. Actuators B* **1996**, *31*, 167-174.

(70) Fruhberger, B.; Stirling, N.; Grillo, F. G.; Ma, S.; Ruthven, D.; Lad, R. J.; Frederick, B. G. *Sens. Actuators* **2001**, *76*, 226-234.

(71) Pilling, R. S.; Bernhardt, G.; Kim, C. S.; Duncan, J.; Crothers, C. B. H.; Kleinschmidt, D.; Frankel, D. J.; Lad, R. J.; Frederick, B. G. *Sens. Actuators B, Submitted.*

(72) Sheinker, V. N.; Mitchell, M. B. *Chem. Mater.* **2002**, *14*, 1257-1268.

(73) Aurian-Blajeni, B.; Boucher, M. M. *Langmuir* **1989**, *5*, 170-174.

(74) Mitchell, M. B.; Sheinker, V. N.; Mintz, E. A. *J. Phys. Chem.* **1997**, *B 101*, 11192-11203.

(75) Segal, S. R.; Cao, L.; Suib, S. L.; Tang, X.; Satyapal, S. *J. Cat.* **2001**, *198*, 66-76.

(76) Rusu, C. N.; J. T. Yates, J. *J. Phys. Chem. B* **2000**, *104*, 12292-12298.

(77) Tesfai, T. M.; Sheinker, V. N.; Mitchell, M. B. *Phys. Rev. B* **1998**, *102*.

(78) Li, Y.; Klabunde, K. J. *Langmuir* **1991**, *7*, 1388-1393.

(79) Henderson, M. A.; Jin, T.; White, J. M. *J. Phys. Chem.* **1986**, *90*, 4607-4611.

(80) Templeton, M. K.; Weinberg, W. H. *J. Am. Chem. Soc.* **1985**, *107*, 97-108.

(81) Kim, C. S.; Lad, R. J.; Tripp, C. P. *Sens. Actuators B* **2001**, *76*, 442-448.

(82) Ai, M. *J. Cat.* **1978**, *54*, 426-435.

(83) Kim, K. S.; Barteau, M. A.; Farneth, W. E. *Langmuir* **1988**, *4*, 533-543.

(84) Kim, K. S.; Barteau, M. A. *J. Molecular Catalysis* **1990**, *63*, 103-117.

(85) Hara, M.; Kawamura, M.; Kondo, J. N.; Domen, K.; Maruya, K. *J. Phys. Chem.* **1996**, *100*, 14462-14467.

(86) Yuan, Y.; Iwasawa, Y. *J. Phys. Chem. B* **2002**, *106*, 4441-4449.

(87) Busca, G.; Elmi, A. S.; Forzatti, P. *J. Phys. Chem.* **1987**, *91*, 5263-5269.

(88) Jackson, R. H. Spatial distributions and transient fluxes in Calibrated Thermal Desorption Spectroscopy. Ph. D., University of Maine, 2000.

(89) Scofield, J. H. *J. Electron Spectrosc. Relat. Phenom.* **1976**, *8*, 129-137.

(90) Christmann, K. *Introduction to Surface Physical Chemistry*; Springer-Verlag: New York, 1991.

(91) Vohs, J. M.; Barteau, M. A. *Surf. Sci.* **1986**, *176*, 91-114.

(92) Cox, D. F.; Schulz, K. H. *J. Vac. Sci. Technol.* **1990**, *A 8*, 2599.

(93) Frederick, B. G.; Apai, G.; Rhodin, T. N. *Surf. Sci.* **1992**, *277*, 337-350.

(94) Gercher, V. A.; Cox, D. F.; Themlin, J. M. *Surf. Sci.* **1994**, *306*, 279-293.

(95) Nishimura, S. Y.; Gibbons, R. F.; Tro, N. J. *J. Phys. Chem. B* **1998**, *102*, 6831-6834.

(96) Wong, G. S.; Kragten, D. D.; Vohs, J. M. *Surf. Sci.* **2000**, *452*, L293-L297.

(97) Schildbach, M. A.; Hamza, A. V. *Surf. Sci.* **1993**, *282*, 306-322.

(98) Hugenschmidt, M. B.; Gamble, L.; Campbell, C. T. *Surf. Sci.* **1994**, *302*, 329-340.

(99) Gercher, V. A.; Cox, D. F. *Surf. Sci.* **1995**, *322*, 177-184.

(100) Akbulut, M.; Sack, N. J.; Madey, T. E. *Surf. Sci.* **1996**, *351*, 209-227.

(101) Henderson, M. A. *Surf. Sci.* **1996**, *355*, 151-166.

(102) Stirniman, M. J.; Huang, C.; Smith, R. S.; Joyce, S. A.; Kay, B. D. *J. Chem. Phys.* **1996**, *105*, 1295.

(103) Nelson, C. E.; Elam, J. W.; Cameron, M. A.; Tolbert, M. A.; George, S. M. *Surf. Sci.* **1998**, *416*, 341-353.

(104) Meng, B.; Weinberg, W. H. *J. Chem. Phys.* **1994**, *100*, 5280.

(105) Weinketz, S. *J. Chem. Phys.* **1994**, *101*, 1632.

(106) Sundberg, M.; Tilley, R. J. D. *J. Solid State Chem.* **1974**, *11*, 150.

(107) Salje, E.; Carley, A. F.; Roberts, M. W. *J. Solid State Chem.* **1979**, *29*, 237.

(108) Bringans, R. D.; Hochst, H.; Shanks, H. R. *Phys. Rev. B* **1981**, *24*, 3481.

(109) Jones, F. H.; Rawlings, K.; Foord, J. S.; Cox, P. A.; Egdell, R. G.; Pethica, J. B.; Wanklyn, B. M. R. *Phys. Rev. B* **1995**, *52*, R14392.

(110) Pilling, R. S.; Bernhardt, G.; Frederick, B. G. *in preparation.*

(111) Ma, S.; Jackson, R. L.; Frederick, B. G. *to be submitted* **2003**.

(112) Woodward, P. M.; Sleight, A. W.; Vogt, T. *J. Phys. Chem. Solids* **1995**, *56*, 1305.

(113) *JCPDS Diffraction Tables*; JCPDS, Ed.; International Centre for Diffraction Data:, 1997.

(114) Jones, F. H.; Rawlings, K.; Foord, J. S.; Egdell, R. G.; Pethica, J. B.; Wanklyn, B. M. R.; Parker, S. C.; Oliver, P. M. *Surf. Sci.* **1996**, *359*, 107-121.

(115) Friedel, J. *Comments Solid State Phys.* **1969**, *2*, 21.

(116) Chazalviel, J. N.; Campagna, M.; Wertheim, G. K.; Shanks, H. R. *Phys. Rev. B* **1977**, *16*, 697.

(117) Kim, K. S.; Baitinger, W. E.; Amy, J. W.; Winograd, N. *J. Electron Spectrosc. Relat. Phenom.* **1974**, *5*, 351.

(118) Angelis, B. A. D.; Schiavello, M. *J. Solid State Chem.* **1977**, *21*, 67-72.

(119) Sabbatini, L.; Sherwood, P. M. A.; Zambonin, P. G. *J. Electrochem. Soc.: Electrochemical Science and Technology* **1983**, *130*, 2199.

(120) Wong, H. Y.; Ong, C. W.; Kwok, R. W. M.; Wong, K. W.; Wong, S. P.; Cheung, W. Y. *Thin Solid Films* **2000**, *376*, 131.

(121) Jorgensen, W. L.; Salem, L. *The organic chemist's book of orbitals*; Academic Press: New York San Francisco London, 1973.

(122) Erskine, J. L.; Bradshaw, A. M. *Chem. Phys. Lett.* **1980**, *72*, 260.

(123) Rodriguez, J. A. *Surf. Sci.* **1992**, *273*, 385.

(124) Bowker, M.; Madix, R. J. *Surf. Sci.* **1982**, *116*, 549-572.

(125) Bowker, M.; Madix, R. J. *Surf. Sci.* **1980**, *95*, 190-206.

(126) Rogers, J. W.; Hance, R. L.; White, J. M. *Surf. Sci.* **1980**, *100*, 388-406.

(127) Hirschwald, W.; Hofmann, D. *Surf. Sci.* **1984**, *140*, 415-424.

(128) Onishi, H.; Aruga, T.; Egawa, C.; Iwasawa, Y. *Surf. Sci.* **1988**, *193*, 33-46.

(129) Kanan, S. M.; Lu, Z.; Cox, J. K.; Bernhardt, G.; Tripp, C. P. *Langmuir* **2002**, *18*, 1707.

(130) Aitken, D. G.; Cox, P. A.; Egdell, R. G.; Hill, M. D.; Sach, I. *Vacuum* **1983**, *33*, 753-756.

(131) Sarkar, S.; Joarder, R. N. *J. Chem. Phys.* **1993**, *99*, 2032.

(132) Lindan, P. J. D.; Harrison, N. M. *Phys. Rev. Lett.* **1998**, *80*, 762.

(133) Jones, F. H.; Dixon, R. A.; Brown, A. *Surf. Sci.* **1996**, *369*, 343-350.

(134) Egelhoff, W. F.; Perry, D. L.; Linnett, J. W. *J. Electron Spectrosc. Relat. Phenom.* **1974**, *5*, 339-350.

(135) Egelhoff, W. F.; Linnett, J. W.; Perry, D. L. *Faraday Discuss. Chem. Soc.* **1975**, *60*, 127.

(136) Allan, D. R.; Clark, S. J.; Brugmans, M. J. P.; Ackland, G. J.; Vos, W. L. *Phys. Rev. B* **1998**, *58*, R11 809.

(137) Asahi, N.; Nakamura, Y. *Chem. Phys. Lett.* **1998**, *290*, 63.

(138) Bako, I.; Jedlovszky, P.; Palinkas, G. *J. Molecular Liquids* **2000**, *87*, 243.

(139) Wise, M. L.; Koehler, B. G.; Gupta, P.; Coon, P. A.; George, S. M. *Surf. Sci.* **1991**, *258*, 166.

(140) Haber, J.; Janas, J.; Schiavello, M.; Tilley, R. J. D. *J. Cat.* **1983**, *82*, 395-403.

(141) Laan, G. v. d.; Westra, C.; Haas, C.; Sawatzky, G. A. *Phys. Rev. B* **1981**, *23*, 4369.

(142) Hufner, S. *Solid State Communications* **1984**, *49*, 1177-1179.

(143) Boer, D. K. G. d.; Haas, C.; Sawatzky, G. A. *Phys. Rev. B* **1984**, *29*, 4401.

(144) Zaanen, J.; Sawatzky, G. A. *Phys. Rev. Lett.* **1985**, *55*, 418.

(145) Ghijsen, J.; Tjeng, L. H.; Elp, J. v.; Eskes, H.; Westerink, J.; Sawatzky, G. A. *Phys. Rev. B* **1988**, *38*, 11322.

(146) Laan, G. v. d.; Zaanen, J.; Sawatzky, G. A.; Karnatak, R.; Esteva, J.-M. *Phys. Rev. B* **1986**, *33*, 4253.

(147) Yamaguchi, T.; Tanaka, Y.; Tanabe, K. *J. Cat.* **1980**, *65*, 442-447.

(148) Ogata, E.; Kamiya, Y.; Ohta, N. *J. Cat.* **1973**, *29*, 296-307.

(149) Grunert, W.; Shpiro, E. S.; Feldhaus, R.; Anders, K.; Antoshin, G. V.; Minachev, K. M. *J. Cat.* **1987**, *107*, 522-534.

(150) Grunert, W.; Morke, W.; Feldhaus, R.; Anders, K. *J. Cat.* **1989**, *117*, 485-494.

(151) Grunert, W.; Feldhaus, R.; Anders, K.; Shpiro, E. S.; Minachev, K. M. *J. Cat.* **1989**, *120*, 444-456.

(152) Pickering, R.; Tilley, R. J. D. *J. Solid State Chem.* **1976**, *16*, 247.

(153) Berak, J. M.; Sienko, M. J. *J. Solid State Chem.* **1970**, *2*, 109-133.

(154) Ma, S.; Amar, F. G.; Frederick, B. G. *J. Phys. Chem. A* **2003**, *107*, 1413-1423.

(155) Gamble, L.; Jung, L. S.; Campbell, C. T. *Surf. Sci.* **1996**, *348*, 1-16.

(156) Spectra Instruments, I. *RGA Application Bulletin # 208, Spectra Reference.*

(157) Nakao, F. *Vacuum* **1975**, *25*, 431.

(158) Nakao, F. *Vacuum* **1975**, *25*, 201-209.

(159) Machiels, C. J.; Cheng, W. H.; Chowdhry, U.; Farneth, W. E.; Hong, F.; Carron, E. M. M.; Sleight, A. W. *Applied Catalysis* **1986**, *25*, 249-256.

(160) Gasior, M.; Grzybowska, B. *React. Kinet. Catal. Lett.* **1986**, *32*, 281-285.

(161) LeGore, L. J.; Lad, R. J. *STM images of WO3.*

(162) Kagel, R. O. *J. Phys. Chem.* **1967**, *71*, 844-850.

(163) Goddard, P.; West, J.; Lambert, R. M. *Surf. Sci.* **1978**, *71*, 447-461.

(164) Taylor, J. L.; Weinberg, W. H. *Surf. Sci.* **1978**, *78*, 259-273.

(165) Falconer, J. L.; Madix, R. J. *J. Cat.* **1977**, *48*, 262-268.

(166) Chan, C. M.; Aris, R.; Weinberg, W. H. *Appl. of Surf. Sci.* **1978**, *1*, 360-376.

(167) Spitz, R. N.; Barton, J. E.; Barteau, M. A.; Staley, R. H.; Sleight, A. W. *J. Phys. Chem.* **1986**, *90*, 4067-4075.

(168) Wallington, T. J.; Hurley, M. D.; Ball, J. C.; Straccia, A. M.; Platz, J.; Christensen, L. K.; Sehested, J.; Nielsen, O. J. *J. Phys. Chem. A* **1997**, *101*, 5302-5308.

(169) Geiger, H.; Becker, K. H. *Atmospheric Environment* **1999**, *33*, 2883-2891.

(170) Vertin, K. D.; Ohi, J. M.; Naegeli, D. W.; Childress, K. H.; Hagen, G. P.; McCarthy, C. I.; Cheng, A. S.; Dibble, R. W. *SAE Sp1458* **1999**, *29*, 41.

(171) Daly, C. A.; Simmie, J. M.; Dagaut, P.; Cathonnet, M. *Combustion and Flame* **2001**, *125*, 1106-1117.

(172) http://webbook.nist.gov/chemistry/.

(173) Ma, S.; Frederick, B. G. *to be submitted* **2003**.

(174) Ouyang, F.; Yao, S. *J. Phys. Chem. B* **2000**, *104*, 11253-11257.

(175) http://0-www.er.doe.gov.library.csuhayward.edu "(BES) Workshop on Basic Research Needs for Countering Terrorism," Office of Basic Energy Sciences (BES), 2002.

(176) Henderson, M. A.; White, J. M. *J. Am. Chem. Soc.* **1988**, *110*, 6939-6947.

(177) Hucknall, D. J. *Selective Oxidation of Hydrocarbons*; Academic Press: New York, 1974.

(178) Cheng, W. H.; Chowdhry, U.; Ferretti, A.; Firment, L. E.; Groff, R. P.; Machiels, C. J.; McCarron, E. M.; Ohuchi, F.; Staley, R. H.; Sleight, A. W. Methanol Oxidation over Molybdate Catalysts. In *Heterogeneous Catalysis*; Shapiro, B. L., Ed.; Texas A&M Press: College Station, TX, 1984.

(179) Badrinarayanan, S.; Mandale, A. B.; Sainkar, S. R. *J. Mater. Res.* **1996**, *11*, 1605.

(180) Lijser, H. J. P. d.; Mulder, P.; Louw, R. *Chemosphere* **1993**, *27*, 773.

(181) Durig, J. R.; Smith, D. F.; Barron, D. A. *J. Analytical and Applied Pyrolysis* **1989**, *16*, 37.

(182) Zegers, E. J. P.; Colantoni, G. M.; Fisher, E. M. *Chem. Phys. Processes Combust.* **1994**, 309-312.

(183) Ma, S.; Frederick, B. G. *to be submitted* **2003**.

## APPENDIX. FLOW CHART FOR MONTE CARLO SIMULATIONS OF DESORPTION

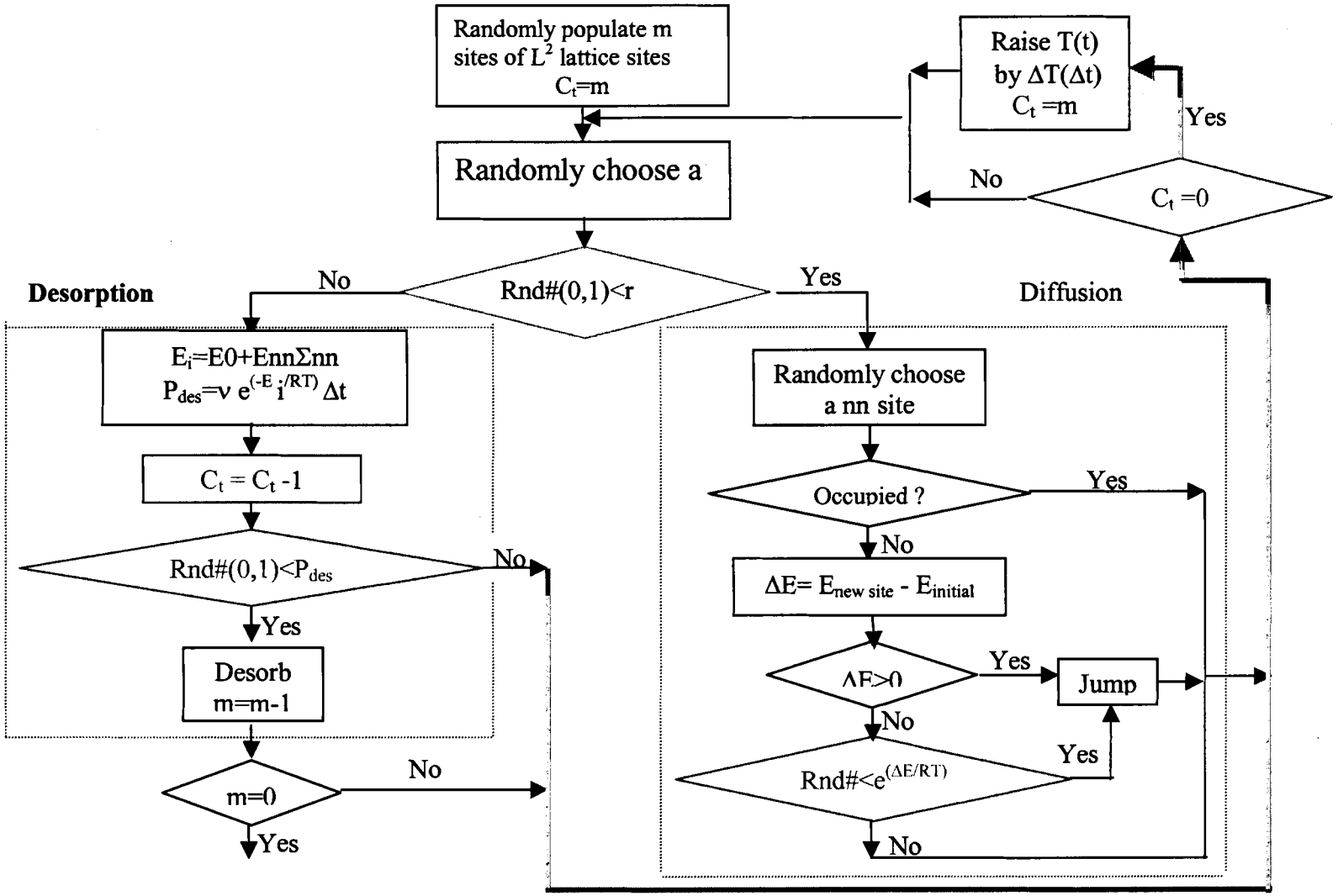

## BIOGRAPHY OF THE AUTHOR

Shuguo Ma was born in Ganhe, Inner Mongolia of China on 1 March, 1968. He graduated from the second high school of Yitulihe in Inner Mongolia in 1987. He graduated with his B.S. degree in Chemistry from Inner Mongolia Normal University in Huhehot of China in 1991. As a chemistry teacher, he worked at the high school of Yakeshi for a year. He attended the Institute of Chemistry of Chinese Academy of Sciences in September 1992 and graduated with M.S. degree in physical chemistry in 1995. During M.S. study, he focused on the studies of dynamics of cation and anion doped crystals, property of electron transfer complexes and formation of bilayer lipid membrane on a small hole using molecular vibration spectroscopy (Raman/surface enhanced Raman spectroscopy and FT-IR). After his M.S. degree, Shuguo Ma joined the Tsinghua University with his formal advisor to continue the research work in those fields.

In the fall of 1998, Shuguo Ma obtained the stipend from the University of Maine which supports him to study in surface science for a Ph.D. Shuguo Ma is a candidate for the Doctor of Philosophy degree in Chemistry from The University of Maine in May, 2003.